8-10-2015 12:00 AM

Computational Studies of Compressed Diborane and Engineered Narrow-Gap Semiconductors

Amin Torabi, *The University of Western Ontario*

Supervisor: Prof. Viktor N. Staroverov, *The University of Western Ontario*

A thesis submitted in partial fulfillment of the requirements for the Doctor of Philosophy degree in Chemistry

COMPUTATIONAL STUDIES OF COMPRESSED DIBORANE AND ENGINEERED NARROW-GAP SEMICONDUCTORS

(Thesis format: Integrated Article)

by

Amin Torabi

Graduate Program in Chemistry

A thesis submitted in partial fulfillment
of the requirements for the degree of
Doctor of Philosophy

The School of Graduate and Postdoctoral Studies
The University of Western Ontario
London, Ontario, Canada

Abstract

The research contained in this thesis is two-fold: understanding the behavior of diborane under pressure, and engineering wide-gap semiconductors in order to promote their optical efficiency. Each of these themes are further explained below.

Diborane (B_2H_6), is a prototypical electron-deficient molecule and has received a great deal of attention in recent years due to its unique and peculiar structure, as well as its potential applications as a hydrogen-storage material. At high pressures, vibrational spectroscopy analysis have revealed several changes in the spectral profile that suggest occurrence of polymorphic transformations; however, the new crystal structures at high pressures have not been identified due to experimental challenges. In this study, we employ electronic structure calculations to investigate and assign the pressure-induced polymorphic transformations of crystalline diborane observed by vibrational spectroscopy up to 88 GPa. In particular, our density-functional calculations predict that diborane will remain in molecular form up to near-megabar pressures, above which it should transform into a structure with covalently bonded chains of boron atoms and eventually become metallic around 138 GPa.

Zinc oxide (ZnO) and zinc sulfide (ZnS) are abundant and nontoxic compound semiconductors, but their band gaps are too wide for potential use in light-harvesting applications. Integration of these thermally and chemically stable compounds into a bulk heterostructure presents an opportunity for the generation of novel materials with notably different properties from their bulk counterparts. Using screened hybrid density-functional methods, we show that the band gaps of ZnO and ZnS can be dramatically reduced by creating layered ZnO/ZnS bulk heterostructures in which m contiguous monolayers of ZnO alternate with n contiguous monolayers of ZnS. In particular, the band gap decreases by roughly 40% upon substitution of every tenth monolayer of ZnS with a monolayer of ZnO (and vice versa) and becomes as low as 1.5 eV for heterostructures with $m = 3$ to $m = 9$ contiguous monolayers of ZnO alternating with $n = 10 - m$ monolayers of ZnS. The predicted band gaps of layered ZnO/ZnS heterostructures span much of the visible spectrum, which makes these materials suitable for photovoltaic device engineering.

Keywords: quantum-chemistry simulations, density-functional theory, diborane, pressure-induced polymorphic transformation, bulk heterostructures, band gap engineering.

Co-Authorship Statement

The research reported here in this thesis is a result of contributions from the author Amin Torabi, supervisor Prof. Viktor N. Staroverov, and coworkers Dr. Chitra Murli and Prof. Yang Song from the Department of Chemistry at the University of Western Ontario, whose contributions are described below.

Chapter 1 describes the computational methodology employed in this study, and was drafted by Amin Torabi and revised by Viktor N. Staroverov.

Chapter 2 is based on the paper "Pressure-induced polymorphic transitions in crystalline diborane deduced by comparison of simulated and experimental vibrational spectra" by Amin Torabi, Yang Song, and Viktor N. Staroverov [*J. Phys. Chem. C* **2013**, *117*, 2210]. Amin Torabi carried out all the calculations, and Yang Song obtained all the experimental spectra. The manuscript was drafted by Amin Torabi and revised by Yang Song and Viktor N. Staroverov.

Chapter 3 is based on the paper "Polymorphic transitions of diborane at sub- and near-megabar pressures" by Amin Torabi, Chitra Murli, Yang Song and Viktor, N. Staroverov [*Sci. Rep.* **2015**, *5*, 13929]. Amin Torabi carried out all the calculations, and Chitra Murli and Yang Song obtained all the experimental spectra. The manuscript was drafted by Amin Torabi and revised by Yang Song and Viktor N. Staroverov.

Chapter 4 is based on the paper "Band gap reduction in ZnO and ZnS by creating layered ZnO/ZnS heterostructures" by Amin Torabi, and Viktor N. Staroverov [*J. Phys. Chem. Lett.* **2015**, *6*, 2075]. Amin Torabi carried out all the calculations. The manuscript was drafted by Amin Torabi and revised by Viktor N. Staroverov.

Acknowledgments

This dissertation marks the endpoint of a long and eventful journey in which I have discovered some great people; and I would like to take this opportunity and thank them for the great work that they do.

Above all, I am immensely grateful to my supervisor, Prof. Viktor N. Staroverov, for his unfailing support and patient guidance throughout the entire course of my program. Viktor's meticulous outlook towards quality research, coupled by his wise counsels, makes him an exceptional supervisor. Viktor has given me the freedom and trust to pursue my ideas, while still challenging me to improve my critical thinking, academic writing and presentation skills. It has been a privilege working with Viktor, and I am very much indebted to him. I must also thank him for his most generous financial assistance and numerous travel opportunities.

I wish to express my sincere thanks to Prof. Yang Song and Prof. T. K. Sham and their group members, for providing us with invaluable resources and knowledge. This work would have not be possible without them, and I cannot thank them enough.

I would like to acknowledge and thank Quantum Espresso and Uspex developers for their fine free codes, and Sharcnet and Compute Canada for their top-notch services.

I owe my deepest gratitude to my beautiful parents and sweet siblings who least understand what I have been doing, but never hesitated to support me in all my endeavors. I thank my dear friends and colleagues at Western, my Friday evening volleyball and Sunday morning soccer peers, who all have been an endless source of enjoyment and vitality in my life. Finally, I am heartily thankful to my beloved wife, Bahar, for our unique amazing chemistry together.

تقدیم به مادر و پدر دلسوزم که با از خودگذشتگی سال‌ها

برای پیشرفت این تاجر بی‌کالا زحمت کشیدند

Contents

List of Figures

List of Tables

List of Abbreviation

DFA	—	density-functional approximaiton
DFT	—	density-functional theory
DOS	—	density of states
ELF	—	electron localization function
GGA	—	generalized-gradient approximation
HSE	—	Heyd–Scuseria–Ernzerhof
IR	—	infrared
LDA	—	local-density approximation
LR	—	long range
PBE	—	Perdew–Burke–Ernzerhof
PBEsol	—	Perdew–Burke–Ernzerhof for solids
PDOS	—	projected density of states
PO	—	pseudo-orbital
PP	—	pseudopotential
SR	—	short range
XC	—	exchange-correlation

Chapter 1

Computational methodology

1.1 Introduction

Computer simulation is a fairly young branch of scientific research, and yet, it is already recognized for its pivotal role in a wide variety of disciplines. Experiments that are either difficult or impossible to set up in laboratories, now have a chance to be simulated computationally. This has been made possible thanks to the tremendous advancement in hardware technology and high-performance programming over the past few decades. Whether it is employed to generate data that we do not have, or to help us comprehend the data that we do already have, computer simulations have transformed our ability to understand the physical world. A legitimate concern in computer simulations, however, is how to build a model, and how truthful the results are. The most reliable strategy regarding simulations in chemistry is not to rely on any hypothesis or conjecture, and formulate a model from the most fundamental laws of nature, *i.e.*, from the very beginning, or as they call it in Latin: *ab initio*.

1.2 Ab initio methods

The most fundamental principles of nature are based on quantum mechanics, and thus, this would be a reasonable starting point for formulating a simulation model. Quantum mechanics postulates that all the knowledge about an electronic system, whether it be a single atom or a large and complex biopolymer, is stored in its wavefunction. This wavefunction can be in principle obtained in the non-relativistic, time-independent, stationary-nucleus scheme by solving the Schrödinger equation

$$\hat{H}\Psi(\mathbf{r}_1, \mathbf{r}_2, \ldots, \mathbf{r}_N) = E\Psi(\mathbf{r}_1, \mathbf{r}_2, \ldots, \mathbf{r}_N), \tag{1.1}$$

where $\hat{H}$, $\Psi(\mathbf{r}_1, \mathbf{r}_2, \ldots, \mathbf{r}_N)$ and E are, respectively, the Hamiltonian operator, the many-body wavefunction, and the total energy of the system, and $\mathbf{r}_i$ denote electronic degrees of freedom.

In fact, a large part of chemistry and physics would be revealed, if only the many-body wavefunction of electronic systems could be exactly determined [1]. However, despite the fact that the equations required for an exact solution have been well known since 1920s, analytical solutions have remained unattainable for all but the simplest systems such as hydrogen-like ions.

This difficulty arises not so much from the complexity of the physical laws. After all, all the matter is composed of positively and negatively charged particles, *i.e.,* electrons and protons, interacting via the Coulomb potential. Instead, the difficulty is due to the pairwise and instantaneous interaction of N electrons and M nuclei within an electronic system, and hence, within the Hamiltonian operator:

$$\hat{H} = -\frac{1}{2}\sum_{i=1}^{N}\nabla_i^2 - \sum_{i=1}^{N}\sum_{j=1}^{M}\frac{Z_j}{|\mathbf{r}_i - \mathbf{R}_j|} + \sum_{i<j}^{N}\frac{1}{|\mathbf{r}_i - \mathbf{r}_j|}. \tag{1.2}$$

The first term in Eq. (1.2) is the kinetic energy of electrons, and the last two are, respectively, the Coulomb interactions arising from the pairwise and instantaneous electron-nucleus attraction and electron-electron repulsion. The electron-nucleus attraction term, also known as the external potential, v_{ext}, is the only system-dependent component in Eq. (1.2), and distinguishes atoms, molecules, solids, etc. Atomic units have been employed above in which $\hbar = e = m_e = 4\pi\epsilon_0 = 1$. Z_j and $\mathbf{R}_j$ in Eq. (1.2) are, respectively, the charge and position of the nuclei.

The pairwise interaction in Eq. (1.2) renders the $3N$-dimensional many-body wavefunction too complicated to obtain, and this complication grows dramatically with increasing number of electrons and nuclei. This necessitates a fundamental change in tackling the solution of Schrödinger equation.

Formulating efficient schemes for approximating this complex many-body wavefunction has been a key objective of scientists since the dawn of quantum mechanics [2]. Most notably, the Hartree−Fock method makes a drastic simplification by assuming that electrons move independently of each other and feel an *effective* Coulomb repulsion arising from the *average* positions of all the other electrons. In a way, the Hartree−Fock method is decoupling the $3N$ degrees of freedom in the many-body wavefunction, thereby enabling each to be treated independently. Furthermore, to

satisfy the Pauli exclusion principle, the Hartree−Fock method involves a so-called exchange potential, which prevents electron from occupying identical quantum states.

The total many-body wavefunction is approximated in the Hartree−Fock scheme by a single determinant composed of single-particle wavefunctions, otherwise known as spin-orbitals:

$$\Psi \approx \frac{1}{\sqrt{N!}} \begin{vmatrix} \psi_1(\mathbf{x}_1) & \psi_2(\mathbf{x}_1) & \cdots & \psi_{\mathrm{N}}(\mathbf{x}_1) \\ \psi_1(\mathbf{x}_2) & \psi_2(\mathbf{x}_2) & \cdots & \psi_{\mathrm{N}}(\mathbf{x}_2) \\ \vdots & \vdots & \vdots & \vdots \\ \psi_1(\mathbf{x}_{\mathrm{N}}) & \psi_2(\mathbf{x}_{\mathrm{N}}) & \cdots & \psi_{\mathrm{N}}(\mathbf{x}_{\mathrm{N}}) \end{vmatrix} \tag{1.3}$$

where $\psi_i(\mathbf{x})$ are single-particle functions, containing both a spatial, $\phi_i(\mathbf{r})$, and a spin, $\chi(\sigma)$, counterpart such that

$$\psi_i(\mathbf{x}_i) = \phi_i(\mathbf{r}_i)\chi(\sigma_i). \tag{1.4}$$

The spatial part of single-particle wavefunctions is obtained from a Schrödinger-like equations of the form

$$\left(-\frac{1}{2}\nabla^2 - \sum_{j=1}^{M}\frac{Z_j}{|\mathbf{r}_i - \mathbf{R}_j|}\right)\phi_i(\mathbf{r}) + \sum_{j=1}^{N}\int d\mathbf{r}'\frac{|\phi_j(\mathbf{r}')|^2}{|\mathbf{r}-\mathbf{r}'|}\phi_i(\mathbf{r}) - \sum_{j=1}^{N}\int d\mathbf{r}'\frac{\phi_j^*(\mathbf{r}')\phi_j(\mathbf{r})}{|\mathbf{r}-\mathbf{r}'|}\phi_i(\mathbf{r}') = \epsilon_i\phi_i(\mathbf{r}) \tag{1.5}$$

known as the Hartree−Fock equations. The second term on the left-hand side is the Hartree potential, $v_{\mathrm{H}}(\mathbf{r})$, which represents the Coulombic potential arising from the electronic charge distribution; and the third term is the exchange potential. It is called "exchange" because according to the principles of quantum mechanics, the total wavefunction of indistinguishable particles, like electrons, should change sign when two particles are exchanged:

$$\Psi(x_1, \ldots, x_i, \ldots, x_j, \ldots, x_N) = -\Psi(x_1, \ldots, x_j, \ldots, x_i, \ldots, x_N) \tag{1.6}$$

Wavefunctions in the Hartree−Fock method *exactly* preserve this property as a consequence of their determinantal form (a determinant changes sign upon exchange of two rows or two columns).

The total Hartree−Fock energy is obtained as:

$$E_{\mathrm{Tot}}^{\mathrm{HF}} = \sum_{i=1}^{N} \int \left(-\frac{1}{2}\nabla^2 - \sum_{j=1}^{M} \frac{Z_j}{|\mathbf{r}_i - \mathbf{R}_j|} \right) \phi_i^*(\mathbf{r})\phi_i(\mathbf{r}) d\mathbf{r} + \frac{1}{2} \sum_{i,j=1}^{N} \int d\mathbf{r} \int d\mathbf{r}' \frac{|\phi_i(\mathbf{r})|^2 |\phi_j(\mathbf{r}')|^2}{|\mathbf{r} - \mathbf{r}'|} - \frac{1}{2} \sum_{i,j=1}^{N} \int d\mathbf{r} \int d\mathbf{r}' \frac{\phi_i(\mathbf{r})\phi_i^*(\mathbf{r}')\phi_j^*(\mathbf{r})\phi_j(\mathbf{r}')}{|\mathbf{r} - \mathbf{r}'|}, \quad (1.7)$$

where the terms on the right-hand side are, respectively, the kinetic energy of electrons, the external energy, the Hartree energy and the exchange energy.

Despite being a milestone in the development of quantum-chemistry methods, the Hartree−Fock predictions fall far short of chemical accuracy ($\sim 1\,\mathrm{kcal/mol}$). It even often fails to provide a qualitative description, the famous example being the case of fluorine molecule F_2, which according to the Hartree−Fock method should not even exist, because it is unstable with respect to atomic dissociation. Therefore, a number of more accurate theories, having their roots in the Hartree−Fock method, have been made available. Configuration interaction, coupled cluster, and Møller–Plesset perturbation theory are among the most popular post-Hartree−Fock methods. However, the added accuracy in these methods have come with a steep price of extra computational demand, and thus, their applications are limited to small electronic systems. That being the case, it did not take long before it was realized that a bare application of *ab initio* methods to real-size chemical problems is an impossible mission. For electronic systems in which the cost of these methods is restrictive, a more effective computational approach is required. This has been achieved by the density-functional theory (DFT) [3], which is a well-tempered balance between computational demand and numerical accuracy at present, and the most widely used approach for electronic structure investigations in physics, chemistry and biology.

1.3 Density-functional theory

In quantum mechanics, the standard approach is to insert the potential energy function of an electronic system into the Schrödinger equation to solve for the wavefunctions. Once the wavefunctions are known, all observable quantities correspond to the expec-

tation value of their corresponding operators, $\hat{\mathcal{O}}$, through the relation:

$$\langle \mathcal{O} \rangle = \langle \Psi | \hat{\mathcal{O}} | \Psi \rangle. \tag{1.8}$$

Density-functional theory reverses this approach for the ground state, in the sense that the electron density is promoted to be the main variable in place of the wavefunction, and all other properties are found as functionals of the electron density. This is a remarkable reduction in the computational complexity, since now, instead of pursuing $3N$-dimensional wavefunctions, $\Psi(\mathbf{r}_1, \mathbf{r}_2, \ldots, \mathbf{r}_N)$, we are dealing with a 3-dimensional density $\rho(\mathbf{r}) \equiv \rho(x, y, z)$ that has a smoother behavior.

The Hohenberg−Kohn [4] and Kohn−Sham [5] papers established the theoretical foundations of density-functional theory, which later earned Walter Kohn, along with John Pople, the 1998 Nobel Prize in Chemistry.

Hohenberg−Kohn theorems state that for the ground state of an electronic system, the Hamiltonian, and hence all the properties that can be derived from it, are all unique functionals of the ground-state electron density. In particular, the total energy is expressed as

$$E = E[\rho(\mathbf{r})], \tag{1.9}$$

and attains its minimum value for the ground-state density. In other words, the ground-state electron density contains simply all the information needed to describe a system. However, the Hohenberg−Kohn theorems only prove the existence of such relation, and do not offer a practical recipe to obtain the exact functional form of $E[\rho(\mathbf{r})]$. Indeed, the exact functional form of $E[\rho(\mathbf{r})]$ has remained unrevealed until the present day, and some suspect that it is perhaps too complicated to be ever obtainable.

A year after the seminal work of Hohenberg and Kohn, Kohn and Sham settled for less and proposed a practical strategy for approximating this functional. The strategy proposed by Kohn and Sham is to map the real interacting electronic system into a fictitious and non-interacting one, in which electrons feel an *effective* one-electron potential, but produce the *same* ground-state density $\rho_0(\mathbf{r})$. Since the real and fictitious systems share the same ground state density, all the properties that are solely and directly determined by the density must be the same for them. The Kohn−Sham effective potential is further partitioned into three components:

$$v_{\mathrm{KS}}(\mathbf{r}) = v_{\mathrm{ext}}(\mathbf{r}) + v_{\mathrm{H}}(\mathbf{r}) + v_{\mathrm{XC}}(\mathbf{r}), \tag{1.10}$$

where $v_{\text{ext}}(\mathbf{r})$ and $v_{\text{H}}(\mathbf{r})$ are, respectively, the external and Hartree potentials, and bear the same meaning as in the Hartree−Fock method; and $v_{\text{XC}}(\mathbf{r})$ is the so-called exchange-correlation potential. It is added to compensate for the interaction of now non-interacting electrons, and is the only unknown component in Eq. (1.10) which has to be approximated.

It should be stressed that the effective potential does not anymore contain a pair-wise interaction term. As a result, Kohn−Sham theory transforms the problem of finding N-dimensional wavefunctions into the problem of finding N 1-dimensional wavefunctions (orbitals) from a set of Schrödinger-like equations of the form

$$\left(-\frac{1}{2}\nabla^2 + v_{\text{KS}}(\mathbf{r})\right)\phi_i(\mathbf{r}) = \epsilon_i\phi_i(\mathbf{r}). \tag{1.11}$$

The single-particle orbitals, $\phi_i(\mathbf{r})$, are further constrained to build the same ground-state density as that of the true interacting system:

$$\rho_0(\mathbf{r}) = \sum_{i=1}^{occ.} |\phi_i(\mathbf{r})|^2, \tag{1.12}$$

where the summation in Eq. (1.12) is over all occupied orbitals. Equations (1.11) and (1.12) are known as the Kohn-Sham equations.

Similar to the expression for potential, the total energy functional is partitioned in the Kohn−Sham DFT as:

$$E_{\text{KS}}[\rho] = T_s[\rho] + E_{\text{ext}}[\rho] + E_{\text{H}}[\rho] + E_{\text{XC}}[\rho], \tag{1.13}$$

where T_s is the kinetic energy of the fictitious non-interacting electrons, E_{ext} and E_{H} are, respectively, the external and Hartree energies arising from the Coulombic interaction of the electron density with the external $v_{\text{ext}}(\mathbf{r})$, and Hartree $v_{\text{H}}(\mathbf{r})$ potentials; and lastly, E_{XC} is the exchange-correlation energy functional, which is related to the exchange-correlation potential, $v_{\text{XC}}(\mathbf{r})$, in Eq. (1.10), but still unknown and needs to be treated approximately.

In essence, the Kohn−Sham method splits the total energy into several terms and wraps all the complications of the many-body interactions into one term, *i.e.*, exchange-correlation, in the hope that approximating a fraction of the total energy is more prudent than approximating the whole. Likewise, the exchange-correlation energy is itself

split into two parts, the exchange and correlation functionals:

$$E_{\mathrm{XC}}[\rho] = E_{\mathrm{X}}[\rho] + E_{\mathrm{C}}[\rho], \tag{1.14}$$

and approximations for each part is sought separately. The exchange part in Eq. (1.14) could be treated in the same *exact* form as in the Hartree−Fock method (see Eq. 1.7 and the discussion afterward),

$$E_{\mathrm{X}}^{\mathrm{exact}}[\rho] = -\sum_{i,j=1}^{N} \int d\mathbf{r} \int d\mathbf{r}' \frac{\phi_i(\mathbf{r})\phi_i^*(\mathbf{r}')\phi_j^*(\mathbf{r})\phi_j(\mathbf{r}')}{|\mathbf{r}-\mathbf{r}'|}. \tag{1.15}$$

It should be emphasized that $\phi_i(\mathbf{r})$ in Eq. (1.15) are the Kohn−Sham orbitals originating from the Kohn−Sham equations, while $\phi_i(\mathbf{r})$ in Eq. (1.7) are the Hartree−Fock orbitals, arising from the Hartree−Fock equations. Therefore, despite their identical functional forms, $E_{\mathrm{X}}^{\mathrm{exact}}$ and $E_{\mathrm{X}}^{\mathrm{HF}}$ use with different orbitals, and thus, will return different energy values.

The correlation part in Eq. (1.14) does not enjoy a similar exact treatment, and it was soon realized that the pair of exact exchange, and approximate correlations does not live up to expectations. Besides, the exact-exchange functional is not an explicit functional of ρ, and depends on the density only implicitly through the Kohn−Sham orbitals by Eq. (1.12). Therefore, the exact exchange is discarded in favor of approximate ones that are explicit functional of density and fit better with the available approximate correlation functionals.

Approximate exchange-correlation energy functionals, $E_{\mathrm{XC}}[\rho]$, can also be expressed in an integral form and in terms of the exchange-correlation density functions, $e_{\mathrm{XC}}(\rho, \ldots)$

$$E_{\mathrm{XC}}[\rho] = \int e_{\mathrm{XC}}(\rho, \ldots) d\mathbf{r}, \tag{1.16}$$

where e_{XC} is a function of the electron density, ρ, but may also contain other ingredients such as the gradient of the density, $\nabla\rho$, the Laplacian of the density, $\nabla^2\rho$, or even the exact-exchange energy density, $e_{\mathrm{X}}^{\mathrm{exact}}$.

In local-density approximation (LDA), for example, $e_{\mathrm{XC}}^{\mathrm{LDA}}$ is solely a function of the density $\rho(\mathbf{r})$ at each point in space, and does not contain other ingredients. LDA is, by construction, the exact functional for a homogeneous electron gas (*i.e.*, when $\rho(\mathbf{r})$ is constant), and still a decent approximation for electronic systems in which density

is slowly varying in space, as in solid-state materials; however, it is not sufficient for atoms and molecules. LDA usually overestimates binding energies, and underestimates bond lengths [6].

Generalized-gradient approximations (GGA) are another class of approximate functionals that can be considered as an extension to LDA, in the sense that $e_{\mathrm{XC}}^{\mathrm{GGA}}$ depends not only on the density at each point in space, but also on how rapidly the density is varying at that point through the gradient of the density, $\nabla\rho$:

$$E_{\mathrm{XC}}^{\mathrm{GGA}}[\rho] = \int e_{\mathrm{XC}}^{\mathrm{GGA}}(\rho, \nabla\rho) d\mathbf{r} = \int e_{\mathrm{XC}}^{\mathrm{LDA}}(\rho) F_{\mathrm{XC}}(\rho, \nabla\rho) d\mathbf{r}. \tag{1.17}$$

In the rightmost equality of Eq. (1.17), the so-called enhancement factor $F_{\mathrm{XC}}(\rho, \nabla\rho)$ is introduced to emphasize the deviation of GGAs from the LDA behavior. To fulfill certain dimensionality requirements, the dependence of the GGA enhancement factors on the gradient of the density is expressed through a dimensionless parameter s of the form

$$s = \frac{|\nabla\rho|}{\rho^{4/3}}. \tag{1.18}$$

The analytic form of $F_{\mathrm{XC}}(s)$ varies in different GGAs, but the asymptotic behavior of $F_{\mathrm{X}}(s)$ in the $s \to 0$ limit is known [7] to be:

$$F_{\mathrm{X}}(s) \xrightarrow[s \longrightarrow 0]{} 1 + \frac{10}{81} s^2. \tag{1.19}$$

The dependence on the gradient of the density makes GGAs more appropriate for electronic systems in which the electron density is far from being uniform. GGAs significantly improve upon LDA for binding energies and atomization energies, but often slightly overestimate bond lengths [8]. Despite this encouraging improvement, GGA approximations systematically fail to reproduce certain observed properties of materials, the most notorious one being the band gaps. GGA functionals severely underestimate semiconductor band gaps and sometimes even erroneously predict them to be metallic. To remedy this shortcoming, more sophisticated density functional approximations (DFA) are called for.

As discussed earlier, exact exchange does not pair well with approximate correlation functionals. In 1993, however, Becke [9] showed that a significant progress will be made, if a *mixture* of exact and approximate exchange is paired with an approximate

correlation functional, in the so-termed *hybrid* functionals:

$$E_{\mathrm{XC}}^{\mathrm{hybrid}} = aE_{\mathrm{X}}^{\mathrm{exact}} + (1-a)E_{\mathrm{X}}^{\mathrm{DFA}} + E_{\mathrm{C}}^{\mathrm{DFA}}, \tag{1.20}$$

where a ($0 \leqslant a \leqslant 1$) is the mixing fraction, may be a constant or a function of $\mathbf{r}$, and is usually obtained by empirically fitting to experimental data. Hybrid functionals have offered a remarkable improvement in accuracy of optical properties over LDA and GGAs. This, however, has been achieved at the expense of a greater computational effort.

Development of approximate exchange and correlation potential or energy functionals that produce more reliable results with less computational demand, and for broader class of electronic systems with less empirical input, has been an active and challenging domain of research in the DFT community. There are currently a variety of DFAs, based on different ideas, in the literature [10]. Some functionals include parameters that are to be obtained by fitting to a set of empirical data; these functionals typically yield accurate results only for systems that are close to their fit set. Others are constructed nonempirically and based on physical concepts and known constraints, and are more well-founded for investigation of unknown compounds and materials. Regardless of how it is constructed, each functional comes with its own strengths and deficiencies, and it is of paramount importance for practitioners of DFT to choose proper ones for any particular situation.

During the course of this work, we employed, for the most part, two energy density-functional approximations: the Perdew−Burke−Ernzerhof (PBE) generalized-gradient approximation [12], along with its minor but critical modification for solids, PBEsol [13]; and also the range-separated Heyd−Scuseria−Ernzerhof (HSE) hybrid density functional [14]. They are each designed to fulfill a particular objective which will be addressed in the following two sections.

1.3.1 PBE and PBEsol functionals

Despite the fact that the exact functional form of E_{xc} is not known, some of its properties and behaviors are indeed known [15]. For example, any approximate exchange density-functional should reduce to the known exact expression of $E_{\mathrm{x}}^{\mathrm{LDA}}$ for a homogeneous electron gas:

$$E_{\mathrm{x}}[\rho] = E_{\mathrm{x}}^{\mathrm{LDA}}[\rho] \qquad \text{if} \qquad \rho(\mathbf{r}) = \text{const.} \tag{1.21}$$

Moreover, Levy and Perdew [16] have suggested that the exchange enhancement factor should be bounded from below:

$$F_{\mathrm{x}} \leqslant 1.804. \tag{1.22}$$

In 1996, Perdew, Burke and Ernzerhof employed these constraints and proposed a non-empirical exchange and correlation functional. In particular, the PBE exchange enhancement factor takes the form of

$$F_{\mathrm{x}}^{\mathrm{PBE}}(s) = 1 + \frac{\mu s^2}{1 + \mu s^2/k}, \tag{1.23}$$

where $k = 0.804$ is set to the maximum value allowed by Eq. (1.22), and $\mu = 0.21951$, is determined from the condition that the second-order gradient coefficient for exchange cancels the corresponding counterpart for correlation. This value, which is almost twice as large as the exact value of $\frac{10}{81}$ in Eq. (1.19), is set to ensure that the PBE exchange-correlation reduces to LDA in the slowly varying regions. Perdew and coworkers have shown that accurate atomization energy predictions are achieved using PBE only at the expense of this violation.

Owing to its non-empirical derivation and relatively simple form, the PBE functional has been the computational workhorse in the solid-state community for almost two decades. However, despite its accurate atomization energy predictions and superior performance over LDA and other GGAs, PBE usually overestimate bond lengths and lattice parameters by 1%. This error is essentially spread out to many physical properties whose values are sensitive to geometries. In 2008, Perdew and coworkers [13] revised PBE with the aim of remedying this situation for solids; the revision, called PBEsol, retains the same functional form of PBE in Eq. (1.23), but restores the original value of $\mu = \frac{10}{81}$ in Eq. (1.19). This new parameterization has been demonstrated to yield more accurate equilibrium geometries, and is expected to become increasingly more accurate at high pressures, where solids are truly slowly varying in density [13]. Atomization energies, however, are predicted with less accuracy with PBEsol than PBE. Therefore, PBEsol outperforms PBE in predicting geometrical parameters but fall behind it in predicting atomization energies. It appears that no GGA can perform well for both of these properties at the same time.

1.3.2 HSE functional

The exact exchange component of hybrid functionals (see Eq. 1.15) has a large spatial extent arising form its $\frac{1}{r_{12}}$ dependence. This causes hybrid functionals to suffer from severe convergence problems in extended electronic systems, where density does not decay fast enough. In order to accelerate the decay of exact exchange interaction in solids, Heyd, Scuseria and Ernzerhof introduced the idea of range-separated hybrid functional in 2003 [14], in which the $\frac{1}{r_{12}}$ operator is partitioned into a short-range (SR) and a long-range (LR) components:

$$\frac{1}{r_{12}} = \underbrace{\frac{1 - f(r_{12})}{r_{12}}}_{\text{SR}} + \underbrace{\frac{f(r_{12})}{r_{12}}}_{\text{LR}}. \tag{1.24}$$

A popular choice for $f(r_{12})$ is the Gauss error function:

$$f(r_{12}) = \text{erf}(\omega r_{12}) = \frac{2}{\sqrt{\pi}} \int_0^{\omega r_{12}} e^{-t^2} dt, \tag{1.25}$$

with ω being a positive parameter. When $\omega \to 0$, we have $f \to 0$, and thus, the long-range component of $\frac{1}{r_{12}}$ in Eq. (1.24) is switched off, and the Coulomb operator is described only by its short-range component. Conversely, when $\omega \to \infty$, we have $f \to 1$, thereby, Eq. (1.24) will be dominated by its long-range component. At other intermediate values of ω, we have $0 \leqslant f \leqslant 1$, which controls how $\frac{1}{r_{12}}$ is split between its short- and long-range components.

Utilizing the range-separated Coulomb operator, we can further split both DFA and exact exchange energies into their short- and long-range components:

$$E_{\text{X}}^{\text{DFA}} = E_{\text{X}}^{\text{DFA,SR}} + E_{\text{X}}^{\text{DFA,LR}}, \tag{1.26}$$

$$E_{\text{X}}^{\text{exact}} = E_{\text{X}}^{\text{exact,SR}} + E_{\text{X}}^{\text{exact,LR}}. \tag{1.27}$$

The hybrid exchange-correlation functional will then be:

$$\begin{aligned} E_{\text{XC}}^{\text{hybrid}} &= a E_{\text{X}}^{\text{exact}} + (1-a) E_{\text{X}}^{\text{DFA}} + E_{\text{C}}^{\text{DFA}} \\ &= a(E_{\text{X}}^{\text{exact,SR}} + E_{\text{X}}^{\text{exact,LR}}) + (1-a)(E_{\text{X}}^{\text{DFA,SR}} + E_{\text{X}}^{\text{DFA,LR}}) + E_{\text{C}}^{\text{DFA}} \end{aligned} \tag{1.28}$$

HSE then proposes to replace the expensive long-range portion of exact exchange,

$E_{\mathrm{X}}^{\mathrm{exact,LR}}$, with the inexpensive long-range portion of a DFA, $E_{\mathrm{X}}^{\mathrm{DFA,LR}}$.

Employing PBE as the DFA in Eq. (1.28) yields the range-separated HSE hybrid density functional, in the form of:

$$E_{\mathrm{XC}}^{\mathrm{HSE}} = aE_{\mathrm{X}}^{\mathrm{exact,SR}} + (1-a)E_{\mathrm{X}}^{\mathrm{PBE,SR}} + E_{\mathrm{X}}^{\mathrm{PBE,LR}} + E_{\mathrm{C}}^{\mathrm{PBE}}, \tag{1.29}$$

for which the optimum value of ω is set by empirical fitting to 0.106 bohr^{-1}, and $a = \frac{1}{4}$ is the mixing fraction of exact and approximate exchange energies, determined by perturbation theory [17].

HSE has substantially lowered the computational demand for calculations in extended systems, and thus has extended the success of hybrid functionals in quantum chemistry into solid-state physics, thereby reproducing experimental optical properties more accurately and at an affordable computational effort.

1.4 Periodic systems

Thus far, the many-body problem of interacting electrons within an electronic system has been addressed in terms of density-functional theory. This, however, is not the only obstacle to surmount. In solids, unlike single atoms and isolated molecules, we are faced with an enormous number of ions (of the order of Avogadro's number) closely packed together in a tiny chunk of matter, with nearly the same amount of electrons moving around and among them. The ions and electrons are so close to each other in solids that the effect of one on another cannot be neglected.

On the face of it, this depicts a too complicated picture to fit into any computational modeling; we seem to need to integrate over an infinite space. This complexity, however, is relieved by observing that most solids have significant degrees of periodicity in their structure; so much so that the whole structure can be constructed by replicating a single atomistic-scale building block, known as the primitive unit cell. The primitive unit cell is identified by a set of three linearly-independent vectors $\mathbf{a}_i$, which will shape the whole lattice once translated in three dimensions by

$$\mathbf{T} = \sum_{i=1}^{3} n_i \mathbf{a}_i, \tag{1.30}$$

with n_i being any set of three integers.

An important consequence of this observation is that all the macroscopic properties of an infinitely large solid can be studied by only focusing on their finite-size unit cell, and instead of taking into account of an infinite number of electrons, it is only required to consider the number of electrons within a single unit cell (or perhaps half of that number, if energy states are doubly occupied).

1.4.1 Bloch's theorem

We may consider the non-interacting electrons of the Kohn-Sham scheme under the influence of an effective Kohn-Sham potential $v_{\mathrm{KS}}(\mathbf{r})$, which essentially possesses the same periodicity as the underlying lattice,

$$v_{\mathrm{KS}}(\mathbf{r}+\mathbf{T}) = v_{\mathrm{KS}}(\mathbf{r}). \tag{1.31}$$

Bloch's theorem states that the Kohn-Sham orbitals under such a periodic potential can be written as:

$$\phi_k(\mathbf{r}) = e^{\mathbf{i}\mathbf{k}\cdot\mathbf{r}} u_k(\mathbf{r}), \tag{1.32}$$

where $u_k(\mathbf{r})$ is a periodic function with, once again, the same periodicity as the underlying lattice,

$$u_k(\mathbf{r}+\mathbf{T}) = u_k(\mathbf{r}), \tag{1.33}$$

and $\mathbf{k}$ is the Bloch wave vectors, to be discussed below. Being periodic, $u_k(\mathbf{r})$ can always be expressed as a Fourier series in the form of

$$u_k(\mathbf{r}) = \sum_G c_{k,G} e^{\mathbf{i}\mathbf{G}\cdot\mathbf{r}}, \tag{1.34}$$

where $c_{k,G}$ are the Fourier coefficients, and $\mathbf{G} = \Sigma_{i=1}^{3} m_i \mathbf{b}_i$ defines the reciprocal lattice vectors, with m_i being any set of three integers, and $\mathbf{b}_i$ a set of three linearly-independent vectors, identifying the reciprocal primitive unit cell, also known as the first Brillouin zone. Furthermore, the primitive unit cell vectors $\mathbf{a}_i$, are set by the Fourier transformation to be related to their reciprocal counterparts $\mathbf{b}_i$ by

$$\mathbf{a}_i \cdot \mathbf{b}_j = 2\pi\delta_{ij}, \qquad i,j = 1,2,3, \tag{1.35}$$

which further causes the lattice vectors $\mathbf{T}$ and the reciprocal lattice vectors $\mathbf{G}$ to be

related by $\mathbf{G}\cdot\mathbf{T}=2\pi l$, with l being an integer.

Combining Eqs. (1.32) and (1.34), we have

$$\phi_k(\mathbf{r})=\sum_G c_{k,G}e^{\mathrm{i}(\mathbf{G}+\mathbf{k})\cdot\mathbf{r}}. \tag{1.36}$$

This shows that Kohn-Sham orbitals in an extended electronic system can be expressed as a linear combination of s. They are termed plane waves because the planes of constant phase are all parallel to each other and perpendicular to the propagation direction.

One of the essential elements of all first-principles methods is representing complicated functions in terms of a set of predefined and conveniently chosen functions known as basis sets. In the case of isolated atoms and molecules, wavefunctions tend to decay at distances far from nuclei. This necessitates the employment of spatially localized basis sets, such as Gaussian- or Slater-type orbitals. They resemble atomic orbitals in the vicinity of nuclei and decay fast far from them. However, Eq. (1.36) denotes that wavefunctions in periodic systems do not decay. This requires utilization of a spatially extended basis set. In fact, the Bloch's theorem implies the natural basis sets needed: plane wave basis sets. Plane wave basis sets have simple mathematical form, and unlike the localized ones, cover all space equally without biasing any particular region.

Eq. (1.32) implies that the orbitals in adjacent unit cells are written as

$$\phi_k(\mathbf{r}+\mathbf{T})=e^{\mathrm{i}\mathbf{k}\cdot(\mathbf{r}+\mathbf{T})}u_k(\mathbf{r}+\mathbf{T})=e^{\mathrm{i}\mathbf{k}\cdot\mathbf{T}}e^{\mathrm{i}\mathbf{k}\cdot\mathbf{r}}u_k(\mathbf{r})=e^{\mathrm{i}\mathbf{k}\cdot\mathbf{T}}\phi_k(\mathbf{r}), \tag{1.37}$$

which further reveals for the corresponding charge density that

$$\left|\phi_k(\mathbf{r}+\mathbf{T})\right|^2=\left|e^{\mathrm{i}\mathbf{k}\cdot\mathbf{T}}\phi_k(\mathbf{r})\right|^2=\left|\phi_k(\mathbf{r})\right|^2. \tag{1.38}$$

These indicate that in a periodic potential, only the phase of the orbitals are different in different unit cells, and the charge densities remain periodic, as expected.

The orbitals in Eq. (1.32) are also labeled by the Bloch wave vectors $\mathbf{k}$, whose values are determined by the Born-von Karman periodic boundary conditions. The Born-von Karman periodic boundary condition states that when there is an infinite number of atoms in a linear chain, the atoms in the middle are unaware of what is happening to the atoms at either end. Therefore, we can always close a chain on itself and treat an

infinite linear chain of atoms as an infinite ring of atoms. That is to say

$$\phi_k(\mathbf{r} + N_i\mathbf{a}_i) = \phi_k(\mathbf{r}), \qquad i = 1, 2, 3, \tag{1.39}$$

with N_i ($\approx 10^{23}$) being the number of lattice points in each direction. Enforcing Bloch's theorem on both sides of Eq. (1.39), we have

$$e^{\mathrm{i}\mathbf{k}\cdot(\mathbf{r}+N_i\mathbf{a}_i)}u_k(\mathbf{r} + N_i\mathbf{a}_i) = e^{\mathrm{i}\mathbf{k}\cdot\mathbf{r}}u_k(\mathbf{r}), \qquad i = 1, 2, 3. \tag{1.40}$$

Employing the periodic property of $u_k(\mathbf{r})$, Eq. (1.40) can only be true if

$$e^{\mathrm{i}\mathbf{k}\cdot N_i\mathbf{a}_i} = 1, \qquad i = 1, 2, 3. \tag{1.41}$$

This restricts the allowed Bloch wave vectors to a discrete but densely packed form,

$$\mathbf{k} = \sum_{i=1}^{3} \frac{m_i}{N_i}\mathbf{b}_i, \qquad m_i = \text{integer}. \tag{1.42}$$

The Bloch wave vector $\mathbf{k}$ is not only restricted to the form of Eq. (1.42), but also can always be confined within the first Brillouin zone. This is because any $\mathbf{k}'$ not in this zone can be rewritten in term of one $\mathbf{k}$ inside the zone and one reciprocal lattice vector $\mathbf{G}$ as:

$$\mathbf{k}' = \mathbf{G} + \mathbf{k} \Longrightarrow e^{\mathrm{i}\mathbf{k}'\cdot\mathbf{T}} = e^{\mathrm{i}\mathbf{k}\cdot\mathbf{T}} \cdot \underbrace{e^{\mathrm{i}\mathbf{G}\cdot\mathbf{T}}}_{=1} = e^{\mathrm{i}\mathbf{k}\cdot\mathbf{T}}; \tag{1.43}$$

therefore, if Eq. (1.37) holds for $\mathbf{k}'$, it will also hold $\mathbf{k}$, such that all $\mathbf{k}' = \mathbf{G} + \mathbf{k}$ are associated with the same orbital ϕ_k.

At this point, it appears that the Bloch's theorem has mapped the original problem of solving orbitals over an infinite space onto new problems. First of all, since Fourier transformations decompose periodic functions into a sum of infinite terms, the orbitals in Eq. (1.32) are expanded over an infinite number of reciprocal lattice vectors $\mathbf{G}$. In addition, Bloch wave numbers $\mathbf{k}$ has populated the Brillouin zone with infinite density. Bloch's theorem has seemingly traded one infinity for two other infinities. These problems, however, are easily dealt with by first, introduction of a plane wave cutoff energy, and second, an efficient scheme of sampling the Brillouin zone. These will be addressed in the following sections.

1.4.2 Cutoff energy

The kinetic energy of noninteracting electrons in the Kohn-Sham method is written as the sum of the terms:

$$\int \phi^*(\mathbf{r}) \left(-\frac{\nabla^2}{2}\right) \phi(\mathbf{r}) d\mathbf{r}. \tag{1.44}$$

Substituting the Kohn-Sham orbitals of Eq. (1.36) into the above term we have,

$$\int \sum_{G'} c^*_{k,G'} e^{-\mathrm{i}(\mathbf{G}'+\mathbf{k})\cdot\mathbf{r}} \left(-\frac{\nabla^2}{2}\right) \sum_{G} c_{k,G} e^{\mathrm{i}(\mathbf{G}+\mathbf{k})\cdot\mathbf{r}} d\mathbf{r} =$$
$$\sum_{G,G'} c^*_{k,G'} c_{k,G} \left(\frac{\mathbf{G}+\mathbf{k}}{2}\right)^2 \underbrace{\int d\mathbf{r} e^{-\mathrm{i}(\mathbf{G}'-\mathbf{G})\cdot\mathbf{r}}}_{=\delta_{\mathbf{G}\mathbf{G}'}} = \sum_{G} \left(\frac{\mathbf{G}+\mathbf{k}}{2}\right)^2 |c_{k,G}|^2 \tag{1.45}$$

This shows that the kinetic energy term of the Kohn-Sham energy is proportional to square of $\mathbf{G}+\mathbf{k}$. On the other hand, $\mathbf{G}+\mathbf{k}$ is the frequency of the oscillating Bloch plane waves, with higher $\mathbf{G}+\mathbf{k}$ indicating a more rapid oscillation, and thus, a less contribution to the Fourier expansion of the ground state. This establishes a justification for truncating the plane wave expansions above a certain point. The point at which the plane waves basis sets are truncated is called the plane-wave cutoff kinetic-energy,

$$\left(\frac{\mathbf{G}+\mathbf{k}}{2}\right)^2 \leqslant E_{\text{cutoff}}. \tag{1.46}$$

The value of cutoff energy depends on the atomic structure within the unit cell, and it is crucial to test the convergence of the results with respect to it. The accuracy of calculations in periodic systems can always be systematically improved by increasing this single parameter. This is a remarkable advantage over other localized basis sets, with which computed properties are often greatly affected by small changes in the basis sets, and a systematic pattern for increasing convergence is not available.

1.4.3 K-point sampling

Bloch's theorem has shifted the focus from the infinite real space to the finite $\mathbf{k}$ space within the first Brillouin zone. On the other hand, Eq. (1.42) indicates that in the limit of $N_i \to \infty$, the first Brillouin zone space is densely filled with $\mathbf{k}$ points. This problem can be surmounted by observing that Kohn-Sham orbitals ϕ_k do not significantly vary

over small changes in $\mathbf{k}$, such that an integration within the first Brillouin zone can be replaced by a summation over a finite but sufficient number of $\mathbf{k}$ points:

$$\int F(\mathbf{k})d\mathbf{k} \approx \sum_j \omega_j F(\mathbf{k}_j). \tag{1.47}$$

A number of methods have been developed for efficiently sampling the $\mathbf{k}$-space. In this work, we employed the Monkhorst-Pack scheme [18]. The Monkhorst-Pack scheme samples the first Brillouin zone with an unbiased and uniform mesh, in which $\mathbf{k}$ points are homogeneously distributed parallel to the reciprocal primitive unit cell in the form of

$$\mathbf{k} = u_1\mathbf{b}_1 + u_2\mathbf{b}_2 + u_3\mathbf{b}_3, \tag{1.48}$$

where $\mathbf{b}_i$ are the reciprocal primitive vectors, and

$$u_i = \frac{2m - M_i - 1}{2M_i}, \qquad m = 1, 2, 3, \ldots, M; \text{ and} \qquad i = 1, 2, 3, \tag{1.49}$$

with M_i being a user-defined integer determining the number of $\mathbf{k}$ points in $\mathbf{b}_i$ direction. A $\mathbf{k}$ point mesh of $M \times M \times M$, for instance, will generate M^3 points within the first Brillouin zone. Structural symmetries, however, may be exploited to reduce this number.

Unlike the value of cutoff energy, the number of $\mathbf{k}$-points sampling the first Brillouin zone is not a variational parameter, and thus, the total energy of an electronic system does not necessarily exhibit a monotonous decrease as the number of the $\mathbf{k}$-points is increased. Nevertheless, it is always crucial to ensure that computed properties are converged with respect that to the $\mathbf{k}$-point mesh.

1.5 Pseudopotentials

A further simplification regarding calculations in extended systems can be achieved by the use of pseudopotentials [19]. This approximation is motivated by the observation that core electrons are not chemically active and can be frozen within the inner atomic shells, while valence electrons are the ones responsible for most chemical activities and are to be treated with care.

As eigenstates of a Hermitian operator, orbitals of core and valence electrons are required to be mutually orthogonal. Core orbitals are highly localized in the vicinity

of nuclei, while valence orbitals are extended far from the nuclei; however, in order to maintain their orthogonality to the core states, valence orbitals oscillate rapidly and have multiple nodes in the core regions.

Figure 1.1 illustrates the radial atomic orbitals of silicon, calculated using the PBEsol exchange-correlation functional. We can see that the core orbitals are all localized within 2 bohr of the nucleus with the expectation values of $\mathbf{r}$ being around 0.2−0.5 bohr. On the other hand, valence orbitals extend beyond 5 bohr, and oscillate around the origin.

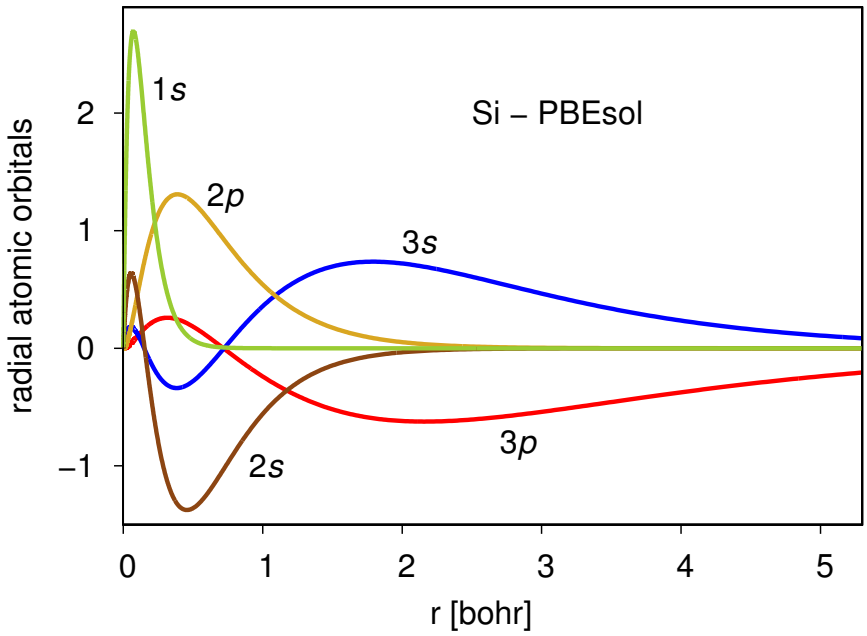

Figure 1.1: Radial atomic orbitals of silicon, calculated using PBEsol functional.

This observation highlights the major drawback of plane wave basis sets: they are not efficient for describing the oscillations of valence orbitals in the unexciting core region. In other words, we need a large number of plane wave basis sets, and thus, computational resources for not much practical usage. In addition, the electron-nucleus potential varies as $\frac{1}{r}$, and diverges to infinity as $r \to 0$, which again, is difficult to be described in terms of plane waves. These difficulties can be avoided by the use of pseudopotentials.

The pseudopotential approximation removes all core electrons as well as the full $\frac{1}{r}$ Coulomb potential arising from the bare nuclear charges, and replace them with a fictitious smooth nondiverging pseudopotential, such that it only reproduces the behavior

of chemically-active valence electrons in the chemically-important valence region. To this end, the rapidly oscillating valence orbitals are replaced with pseudo-orbitals (PO) that are identical to the real ones in the outer region, but is non-oscillating and nodeless in the core region (Figure 1.2). These modifications give rise to softer potentials and orbitals, and consequently a substantially smaller number of plane wave basis sets for adequately describing them.

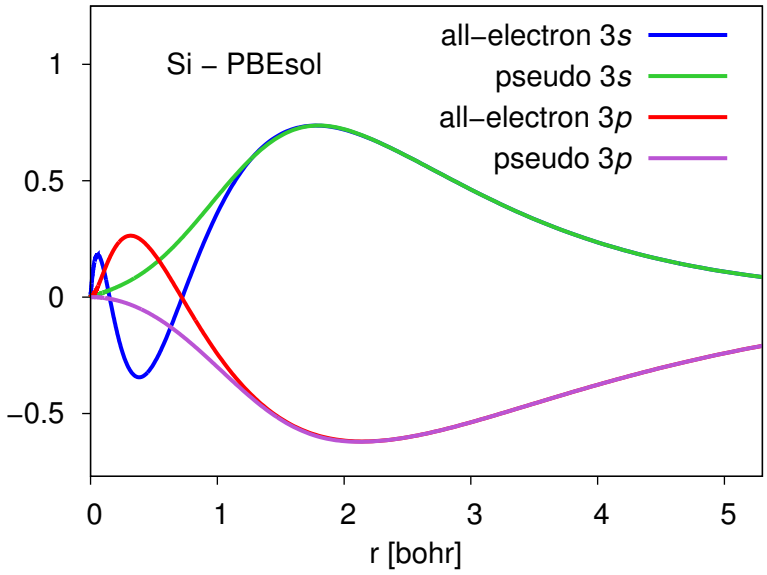

Figure 1.2: Radial atomic all-electron and pseudo orbitals of silicon, calculated using the PBEsol functional.

In order to construct the pseudo-orbitals for an atom, we should first decide which electrons are to be treated as core or valence. Then, for each valence electron with an angular momentum l, a cutoff radius $r_{c,l}$ should be set for separating the core and valence regions. It is then crucial to produce good quality all-electron atomic orbitals for each valence electron using a density-functional method. The radial part of each pseudo-orbital is then constructed so that it is identical to its all-electron counterpart beyond the cutoff radios:

$$R^l_{\text{PO}}(\mathbf{r}) = R^l_{\text{all-electron}}(\mathbf{r}), \qquad r \geqslant r_{c,l}. \tag{1.50}$$

This ensures that the pseudo-orbitals retain the same properties as that of the real ones in the chemically-important zone. For $r \leqslant r_c$, however, the construction of pseudo-orbitals is not unique, but all the available recipes attempt to smooth them out in the core region. In particular, the Troullier-Martins norm-conserving pseudopotential [21]

assumes that

$$R^l_{\mathrm{PO}}(\mathbf{r}) = r^l e^{p(r)}, \qquad r \leqslant r_{c,l}, \tag{1.51}$$

where $p(r)$ is a polynomial of order six in r^2:

$$p(r) = c_0 + c_2 r^2 + c_4 r^4 + c_6 r^6 + c_8 r^8 + c_{10} r^{10} + c_{12} r^{12}. \tag{1.52}$$

The odd powers of r are not included in the polynomial to obtain a smoother behavior of the pseudo-orbitals. In order to determine the seven coefficients of the polynomial, Troullier and Martins demand that the core charge enclosed within $r_{c,l}$ must be the same for the pseudo-orbital and its all-electron counterpart

$$\int_0^{\mathbf{r}_{c,l}} \left|R^l_{\mathrm{PO}}(\mathbf{r})\right|^2 r^2 d\mathbf{r} = \int_0^{\mathbf{r}_{c,l}} \left|R^l_{\text{all-electron}}(\mathbf{r})\right|^2 r^2 d\mathbf{r}. \tag{1.53}$$

This guarantees that the total charge within the core region, and thus, the electrostatic potential of the real- and pseudo-orbitals are the same. Moreover, according to Troullier and Martins, the pseudo-orbitals and their first four derivatives must be continuous at the cutoff radios $r_{c,l}$, and the screened pseudopotential must have zero curvature at the origin. These conditions are set to ensure the smoothness of pseudo-orbitals.

Once pseudo-orbitals are constructed, the screened (scr) atomic pseudopotential is obtained by inversion of the radial Schrödinger equation:

$$v^{l,\mathrm{scr}}_{\mathrm{PP}}(\mathbf{r}) = \epsilon_l - \frac{l(l+1)}{2r^2} + \frac{1}{2rR^l_{\mathrm{PO}}(\mathbf{r})}\frac{d^2}{dr^2}[rR^l_{\mathrm{PO}}(\mathbf{r})]. \tag{1.54}$$

The total atomic pseudopotential will be composed of several components, one for each angular momentum involved; the total molecular or crystalline pseudopotential will also be obtained by a linear superposition of their constituent atomic pseudopotentials. Since the pseudo-orbitals are, by construction, continuous up to the fourth derivatives, the pseudopotentials emerging from Eq. (1.54) will also be continuous; and since pseudo-orbitals are nodeless and behave as r^l near the origin, the pseudopotentials will not have any singularity, and thus, is non-diverging.

The screened pseudopotential of Eq. (1.54) is the total single-particle potential whose eigenstates are the desired pseudo-orbitals. An unscreened pseudopotential, which will play the role of the external potential in the Kohn-Sham scheme, can be obtained by subtracting the Hartree and exchange-correlation potentials from the screen

pseudopotential:

$$v_{\mathrm{PP}}^{l,\mathrm{ion}}(\mathbf{r}) = v_{\mathrm{PP}}^{l,\mathrm{scr}}(\mathbf{r}) - v_{\mathrm{H}}(\mathbf{r}) - v_{\mathrm{xc}}(\mathbf{r}), \tag{1.55}$$

where the Hartree and exchange-correlation potentials of Eq. (1.55) are evaluated from the occupied valence pseudo-orbitals.

It should also be noted that the exchange-correlation functional utilized in Eq. (1.55) must be the same employed for the construction of all-electron atomic orbitals, and the same as in the targeted calculations employing the unscreened pseudopotential. Inconsistencies between them will lead to unpredictable outcomes.

1.6 Evolutionary crystal structure prediction

Structure is the most paramount piece of information about a condensed-matter system, which has been traditionally garnered from X-ray or neutron diffraction experiments. Given this information, computational chemists have been able to compute most of the properties of materials using state-of-the-art simulation techniques.

Predicting the crystal structure of a solid at a given pressure and temperature, based on pure human reasoning and without any prior knowledge of experiments, has long been believed to be an impossible mission. It corresponds to finding the global minimum of a $3N + 3$ dimensional potential landscape, where N, the number of atoms within the unit cell, may not even be known. It is indeed such a formidable task that two decades ago, the answer to the question "Are crystal structures predictable?" [20] was:

> "No": by just writing down this concise statement, in what would be the first one-word paper in the chemical literature, one could safely summarize the present state of affairs, earn an honorarium from the American Chemical Society, and do a reasonably good service to his or her own reputation.

Since then, a number of methods have been developed to address this difficulty. In particular, an evolutionary algorithm for crystal structure prediction was pioneered by Oganov *et al.* in 2006 [22], and implemented and made public in 2010 in the USPEX code [23]. This has proved to be a powerful approach in determining the crystal structure of materials, and has led to a number of significant discoveries [24, 25, 26, 27].

The USPEX code combines first-principles enthalpy calculations with an evolutionary algorithm to find the most stable and a number of metastable crystal structures,

by only knowing their chemical compositions. The evolutionary algorithm for crystal structure prediction imitates Darwinian evolution and employs its terminology. It starts with an unbiased sampling of the potential energy surface by randomly generating a number of structures to populate the first generation. It then determines the quality of each member of the population by optimizing their geometries using the accompanying first-principles code. Poor members of the first generation, *i.e.*, the structures with the highest enthalpies, will be discarded, and the fittest ones will be selected as parents from which members of the second generation are born. This process is repeated in multiple generations until reaching a certain number of subsequent generations where the fittest member is not changing anymore.

To ensure that good genes are passed on from one generation to the subsequent ones, USPEX employs a mixture of special operators, known as lattice mutation, atomic permutation, softmutation and heredity. Through lattice mutation, fractional coordinates of atoms within parent unit cells remain unchanged, but their unit cell vectors are randomly distorted. This enables an efficient exploration in the neighborhood of good individuals on the potential landscape. Through atomic permutation, unit cell vectors remain unchanged, but chemical identities of atoms are exchanged in randomly selected pairs. This is especially useful for electronic systems in which chemically similar atoms are present. Heredity operator combines random slices of two parent unit cells to form a single offspring. Heredity expands diversity in the population while still preserving the already found good individuals. Softmutation involves mutation of unit cells, not along a random vector, but along the softest phonon eigenmodes. Soft phonon modes are indicative of instabilities in structures, and by mutating the unit cells along them, one can avoid instabilities. These special operators enable one to zoom into more promising regions of the potential landscape until a global minimum is found.

The strength of the evolutionary algorithm lies in the fact that subsequent generations have, by construction, increasingly better quality than previous generations. In that sense, it is a self-learning and self-improving method that locates, step by step, the best structures. Employing evolutionary algorithm for structure prediction, one can compute most of the properties of a material, even before it is synthesized.

1.7 Scope of this study

This study is focused on quantum-chemistry simulations, in the framework of density-functional theory, in order to understand, explain, and predict experimental results. This is partly carried out in collaboration with Prof. Yang Song group in the Department of Chemistry at the University of Western Ontario. Prof. Song and his colleagues have obtained experimental infrared and Raman spectra of solid diborane at high pressures, and based on changes in the spectral profile, have suggested that diborane undergoes a number of phase transitions. However, the crystal structures of the new phases have not been identified due to experimental challenges in both sample confinement and *in situ* structural characterization under extreme pressures. We have simulated the pressure dependence in the vibrational spectra of a number of plausible structures of diborane, and by comparison with the available experimental data, have interpreted the pressure-induced polymorphic transitions in diborane.

The second part of this thesis is focused on band gap engineering of wide-gap semiconducting materials in the hope of improving their optical performance. In particular, we have studied how the band structures and band gap energies can be modified in layered heterostructures of zinc oxide and zinc sulfide.

In Chapter 2, we investigate and assign the pressure-induced structural transformations in crystalline diborane observed spectroscopically by Song and co-workers (*J. Phys. Chem. B* **2009**, 113, 13509; *J. Chem. Phys.* **2009**, 131, 174506) between 3.5 and 24 GPa at room temperature. The assignment is made by calculating the Raman and infrared vibrational spectra of 10 candidate structures at various pressures and comparing the results to experiment. We find that solid diborane undergoes a polymorphic transition at about 6 GPa from β-diborane ($P2_1/n$) to a $P2_1/c$ diborane and possibly a second transition near 14 GPa to another $P2_1/c$ diborane structure. We conclude that no cyclic oligomers or chains of the composition $(BH_3)_n$ ($n > 2$) are formed from diborane up to at least 24 GPa under the experimental conditions employed by the Song group, even when such structures are thermodynamically favored. This suggests that pressure-induced chemical transformations of molecular crystals of diborane are kinetically hindered.

In Chapter 3, we report new pressure-induced polymorphic transformations of crystalline diborane observed between 36 and 88 GPa by *in situ* Raman spectroscopy and interpreted using electronic structure calculations. Two previously unknown phase transitions are identified near 42 and 57 GPa, as evidenced by significant changes

in the Raman profiles. The corresponding new phases, labeled IV and V, consist of B_2H_6 molecules and have triclinic unit cells ($P\bar{1}$), as deduced through evolutionary structure search and comparison of experimental and simulated Raman spectra. Density-functional calculations suggest that, at pressures above 110 GPa, phase V will form new molecular structures consisting of one-dimensional $(BH_3)_n$ chains and will become metallic near 138 GPa.

In Chapter 4, using screened hybrid density-functional methods, we show that the band gaps of ZnO and ZnS can be dramatically reduced by creating layered ZnO/ZnS bulk heterostructures in which m contiguous monolayers of ZnO alternate with n contiguous monolayers of ZnS. In particular, the band gap decreases by roughly 40% upon substitution of every tenth monolayer of ZnS with a monolayer of ZnO (and vice versa) and becomes as low as 1.5 eV for heterostructures with $m = 3$ to $m = 9$ contiguous monolayers of ZnO alternating with $n = 10 - m$ monolayers of ZnS.

Bibliography

[1] P. A. M. Dirac. "Quantum mechanics of many-electron systems". *Proc. Roy. Soc. A* **1929**, *123*, 714.

[2] A. Szabo, N. S. Ostlund, *Modern Quantum Chemistry: Introduction to Advanced Electronic Structure Theory*, Macmillan Publishing Co., Inc., New York, **1982**.

[3] R. G. Parr, W. Yang, *Density-Functional Theory of Atoms and Molecules*, Oxford University Press, New York, **1989**.

[4] P. Hohenberg, W. Kohn. "Inhomogeneous electron gas". *Phys. Rev.* **1964**, *136*, B864.

[5] W. Kohn, L. J. Sham. "Self-consistent equations including exchange and correlation effects". *Phys. Rev.* **1965**, *140*, A1133.

[6] R. O. Jones, O. Gunnarsson. "The density functional formalism, its applications and prospects". *Rev. Mod. Phys.* **1989**, *61*, 689.

[7] P. R. Antoniewicz, L. Kleinman. "Kohn-Sham exchange potential exact to first order in $\rho(\mathbf{K})/\rho_0$". *Phys. Rev. B* **1985**, *31*, 6779.

[8] M. Ernzerhof, G. E. Scuseria. "Assessment of the Perdew–Burke–Ernzerhof exchange-correlation functional". *J. Chem. Phys.* **1999**, *110*, 5029.

[9] A. D. Becke. "Density-functional thermochemistry. III. The role of exact exchange". *J. Chem. Phys.* **1993**, *98*, 5648.

[10] G. E. Scuseria, V. N. Staroverov, "Progress in the development of exchange-correlation functionals", in [11].

[11] C. E. Dykstra, G. Frenking, K. S. Kim, G. E. Scuseria (Eds.), Elsevier, Amsterdam, **2005**.

[12] J. P. Perdew, K. Burke, M. Ernzerhof. "Generalized gradient approximation made simple". *Phys. Rev. Lett.* **1996**, *77*, 3865.

[13] J. P. Perdew, A. Ruzsinszky, G. I. Csonka, O. A. Vydrov, G. E. Scuseria, L. A. Constantin, X. Zhou, K. Burke. "Restoring the density-gradient expansion for exchange in solids and surfaces". *Phys. Rev. Lett.* **2008**, *100*, 136406.

[14] J. Heyd, G. E. Scuseria, M. Ernzerhof. "Hybrid functionals based on a screened Coulomb potential". *J. Chem. Phys.* **2003**, *118*, 8207.

[15] M. Levy, J. P. Perdew. "Density functionals for exchange and correlation energies: Exact conditions and comparison of approximations". *Int. J. Quantum Chem. Symp.* **1994**, *49*, 539.

[16] M. Levy, J. P. Perdew. "Tight bound and convexity constraint on the exchange-correlation-energy functional in the low-density limit, and other formal tests of generalized-gradient approximations". *Phys. Rev. B* **1993**, *48*, 11638.

[17] J. P. Perdew, M. Ernzerhof, K. Burke. "Rationale for mixing exact exchange with density functional approximations". *J. Chem. Phys.* **1996**, *105*, 9982.

[18] H. J. Monkhorst, J. D. Pack. "Special points for Brillouin-zone integrations". *Phys. Rev. B* **1976**, *13*, 5188.

[19] E. W. Pickett. "Pseudopotential methods in condensed matter applications". *Comput. Phys. Rep.* **1989**, *9*, 115.

[20] A. Gavezzotti. "Are crystal structures predictable?". *Acc. Chem. Res.* **1994**, *27*, 309.

[21] N. Troullier, J. L. Martins. "Efficient pseudopotentials for plane-wave calculations. *Phys. Rev. B* **1991**, *43*, 1993.

[22] A. R. Oganov, C. W. Glass. "Crystal structure prediction using ab initio evolutionary techniques: Principles and applications". *J. Chem. Phys.* **2006**, *124*, 244704.

[23] A. R. Oganov, *Modern Methods of Crystal Structure Prediction*, Wiley-VCH, Berlin, **2010**.

[24] Y. Ma, M. Eremets, A. R. Oganov, Y. Xie, I. Trojan, S. Medvedev, A. O. Lyakhov, M. Valle, V. Prakapenka. "Transparent dense sodium". *Nature* **2009**, *458*, 182.

[25] A. R. Oganov, J. Chen, C. Gatti, Y. Ma, Y. Ma, C. W. Glass, Z. Liu, T. Yu, O. O. Kurakevych, V. L. Solozhenko. "Ionic high-pressure form of elemental boron". *Nature* **2009**, *457*, 863.

[26] Q. Zhu, D. Y. Jung, A. R. Oganov, C. W. Glass, C. Gatti, A. O. Lyakhov. "Stability of xenon oxides at high pressures". *Nature Chem.* **2013**, *5*, 61.

[27] Y.-L. Li, S.-N. Wang, A. R. Oganov, H. Gou, J. S. Smith, T. A. Strobel. "Investigation of exotic stable calcium carbides using theory and experiment". *Nature Commun.* **2015**, *6*, 6974.

Chapter 2

Pressure-induced polymorphic transitions in diborane up to 24 GPa

2.0 Introduction

Boron has a unique and exceptional chemistry. It is located between the metals and insulators in the second period of the Periodic Table, with fewer valence electrons than valence orbitals. Three electrons in the valence shell favor metallicity, and indeed, most compounds of this element are found to be either metallic or ionic. However, there are others found to be insulating and non-polar. The existence of such compounds could not be initially explained by conventional schemes of bonding. Diborane (B_2H_6), for instance, has two borons and six hydrogens, Figure 2.1, resulting in a total of twelve valence electrons; and yet, it appears to create eight bonds, for which it is four electrons short. It is also two electrons short to be bonded as in ethane (C_2H_6), and different from dialuminum hexachloride (Al_2Cl_6), in which the bridging bonds are created by donation of a lone pair of electrons from the chlorine atoms to the empty $3p$ orbitals of aluminum atoms.

Such compounds are termed "electron-deficient", and their structures are described by the existence of the so-called three-center two-electron bonds. William N. Lipscomb received the 1976 Nobel Prize in Chemistry for his work on structures of boron hydrides [1]. The bonding scheme in diborane is described by first assigning eight of the twelve electrons to the conventional σ bonds between the terminal hydrogens and

Reprinted in part with permission from **A. Torabi**, Y. Song and V. N. Staroverov, "Pressure-induced polymorphic transitions in crystalline diborane deduced by comparison of simulated and experimental vibrational spectra", *J. Phys. Chem. C* **2013**, *117*, 2210.

borons. The remaining four valence electrons are then used to create three-center–two-electron bonds between the bridging hydrogens and each boron. In this way, the boron atoms make the most out of a poor condition, and for this, the bridging electrons have to labor more than usual. The outcome is consequently a weaker and longer bond than the terminal ones.

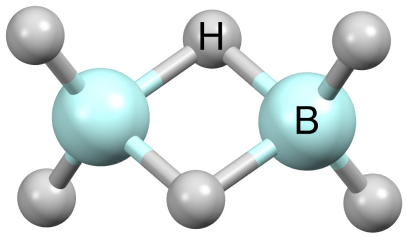

Figure 2.1: Structure of diborane molecule.

It should also be noted that monoborane BH_3, is not a stable compound, as the empty $2p$ orbital of boron makes it a good target for nucleophiles. In the absence of an external nucleophile, however, it dimerizes to diborane. A pair of electrons which used to bond two centers in monoborane, is now spread over three centers in diborane. This makes diborane the simplest stable molecular boron hydride.

At ambient conditions, diborane is a gas (melting point = 108 K, boiling point = 181 K at 1 atmosphere), but it can be liquefied and solidified by cooling or compression. Solid phases of diborane, especially at high-pressure conditions, have been identified as possible high-temperature superconductors with a predicted critical temperature of around 100 K [2], and also hydrogen-storage media with a storage density exceeding that of liquid H_2 [3]. Twenty two percent of diborane weight is hydrogen, which makes it comparable to methane (25%) in terms of hydrogen capacity. Experimental and theoretical investigations of high-pressure structures and transformations of boron hydrides are therefore of significant technological interest.

At present, experimental information about crystalline boron hydrides is very limited due to the difficulty of locating weakly scattering hydrogen and boron atoms by X-ray diffraction techniques. At low temperatures ($T < 100$ K) and ambient pressure, only four forms of B_2H_6 have been reported in the literature [4, 5] and only one of them, β-diborane, has been identified and characterized [6]. The β-phase crystallizes in the $P2_1/n$ space group (monoclinic crystal system), with two formula units per cell [6] as shown in Figure 2.2.

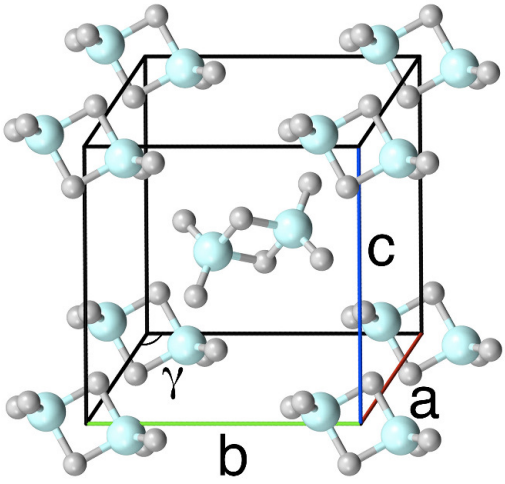

Figure 2.2: Structure of β-diborane at ambient pressure ($a = 4.416$ Å, $b = 5.963$ Å, $c = 6.069$ Å, $\gamma = 104.2$). The lattice parameters were optimized using the PBEsol functional.

Even less is known about high-pressure phases of solid boron hydride. In 2009, the Song group [8, 7] studied pressure-induced structural transformations of diborane at room temperature using *in situ* Raman and synchrotron infrared (IR) spectroscopy. On the basis of changes in spectral profiles of B_2H_6 between 1 atmosphere and 24 GPa, it was suggested that diborane undergoes three phase transitions at about 4, 6, and 14 GPa. The first of these is from the liquid to the solid state, and the other two are polymorphic transitions. The structures of the crystalline phases involved in the polymorphic transitions, however, have not been identified.

In 2011, Yao and Hoffmann [9] carried out an extensive theoretical investigation of possible pressure-induced transformations of boron hydride between 1 atmosphere and 100 GPa using the PBE functional. These workers considered several plausible polymorphs including structures consisting of dimers, cyclic trimers, tetramers, and hexamers of the general formula $(BH_3)_n$, as well as crystals of one-dimensional infinite chains of BH_3. By comparing the calculated enthalpies of these structures at various pressures, Yao and Hoffmann predicted two phase transitions at 0 K: the first at ∼4 GPa, from β-diborane to a molecular crystal of cyclic trimers crystallizing in the $P\bar{1}$ space group; the second at ∼36 GPa, from the molecular crystal of trimers to a $P2_1/c$ crystal of one-dimensional chains, $(BH_3)_n$ [9]. The predictions of Yao and Hoffmann are consistent with the local-density approximation calculations by Barbee *et al.* [3] which also suggested that molecular forms of boron hydride become unstable at high pressure. One should keep in mind that these predictions were made theoreti-

cally by considering only the relative thermodynamic stability (enthalpies) of various phases, leaving aside the issue of kinetic persistence, and that the post-2009 computational studies of crystalline diborane [2, 9] did not fully exploit the experimental data of Song and co-workers [8, 7].

In this study, we interpret the structural changes in compressed diborane observed spectroscopically by the Song group [8, 7]. We do this by calculating the frequencies and intensities of Raman and IR transitions for the 10 candidate structures listed in Table 2.1, and comparing the results to the observed spectra. We selected these structures because, to the best of our knowledge, they are the only ones for which full structural parameters have been published in the literature [6, 2, 9].

Table 2.1: Candidate structures of crystalline boron hydride used for spectroscopic assignment in this study.

structure	molecular unit	source
$P2_1/n$	dimer	Ref. [6]
$P2_1/c$ (**A**)	dimer	Ref. [9]
$P2_1/c$ (**B**)	dimer	Ref. [2]
$Cmc2_1$	trimer	Ref. [9]
$P\bar{1}$	trimer	Ref. [9]
$P2_1/c$	chain	Ref. [9]
$Pna2_1$	chain	Ref. [2]
$P2_1/m$	chain	Ref. [2]
$Pbcn$	chain	Ref. [2]
$Cmcm$	chain	Ref. [2]

The main difference between the computational methodology adopted in this work and those of the previous studies [2, 3, 9] is that here we go beyond the LDA and PBE approximation and use the Perdew–Burke–Ernzerhof exchange-correlation functional for solids (PBEsol), a minor but critical modification of the PBE functional. We chose the PBEsol functional because it makes the most accurate prediction for the lattice parameters of the best-studied phase (β-diborane) at low temperature and ambient pressure experiment, and is supposed to become increasingly accurate at high pressures. The agreement between theory and experiment turns out to be sufficiently clear-cut to propose specific structure assignments.

2.1 Computational methodology

All calculations reported in this work were performed using Quantum Espresso (version 4.3), [10] a plane-wave/pseudopotential electronic structure code. The lattice parameters and atomic positions for each candidate structure were optimized at a fixed pressure at $T = 0$ K by minimizing the enthalpy. To simulate IR spectra, we optimized the candidate structures at the PBEsol level and then calculated IR frequencies and intensities using the PBEsol functional. To simulate Raman spectra, we reoptimized all structures at the LDA level and calculated Raman frequencies and intensities using the LDA. Different functionals had to be used for simulating IR and Raman spectra because Raman spectral intensities are implemented in Quantum Espresso only for the LDA functional. In all cases, we used vibrational frequencies without applying any scale factors.

The pseudopotentials were taken from the Quantum Espresso pseudopotential library. In the PBEsol calculations, the PBE ultrasoft Vanderbilt pseudopotentials [11] with a cutoff energy of 90 Ry for the plane-wave expansion were utilized. In the LDA calculations, the norm-conserving LDA pseudopotentials with a cutoff energy of 130 Ry were employed. The Brillouin zone was sampled using the Monkhorst–Pack scheme. The following **k**-point meshes were used: $6 \times 4 \times 4$ for β-diborane; $6 \times 6 \times 4$ for the $P2_1/c$ (**A**) dimer and $P\bar{1}$ trimer; $6 \times 4 \times 6$ for the $P2_1/c$ (**B**) dimer and the $Pna2_1$, $Pbcn$, and $Cmcm$ chains; $4 \times 6 \times 4$ for the $Cmc2_1$ trimer; $4 \times 6 \times 6$ for the $P2_1/c$ chain; $6 \times 6 \times 6$ for the $P2_1/m$ chain. Convergence with respect to the cutoff energy and the **k**-point mesh was verified for all structures. The convergence criterion for Kohn–Sham self-consistency cycles was set to 10^{-10} Ry.

In all structural optimizations, the Broyden–Fletcher–Goldfarb–Shanno quasi-Newton algorithm was used for both ionic and cell dynamics. The optimization was stopped when the components of all Hellmann–Feynman forces dropped below 10^{-4} Ry/Å, and the pressure on the cell was less than 0.05 GPa of the target. Lattice parameters and atomic positions optimized at each pressure were used as initial guesses for the optimization at the next higher pressure.

The nonresonant Raman intensities were computed using the method described in Ref. [12]. IR intensities were calculated by density-functional perturbation theory [13]. The XCrySDen package [14] was used for visualizing the results.

2.2 Results and discussion

Figure 2.3 shows how the computed enthalpies of the candidate structures studied in this work vary with pressure. We see that β-diborane is not the most stable structure under compression. The trimer-based structures are more stable than β-diborane above ~0.5 GPa; the linear-chain $P2_1/c$ structure becomes the most favored above ~35 GPa. These observations are generally in agreement with the PBE calculations by Yao and Hoffmann [9] and by Abe and Ashcroft [2]. One noteworthy difference is that the PBEsol method predicts the two trimer structures ($Cmc2_1$ and $P\bar{1}$) to be almost as stable as β-diborane at ambient pressure (see the inset in Figure 2.3), whereas PBE calculations predict [9] the trimers to have a slightly higher enthalpy than β-diborane until about 4 GPa (the difference is ~0.04 eV/BH_3 at ambient pressure). Although such thermodynamic stability data are useful, they are not sufficient for making spectroscopic assignments. To cite a well-known example, diamond does not spontaneously turn into graphite at ambient temperature and pressure, even though the latter is favored thermodynamically.

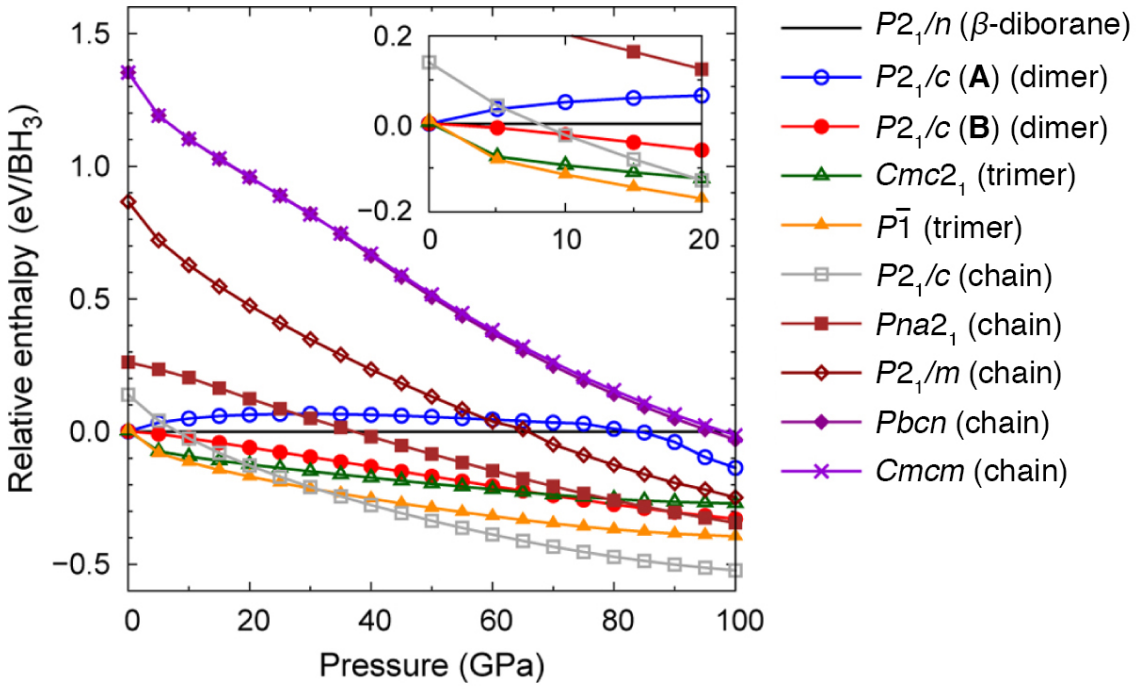

Figure 2.3: Enthalpies of the 10 candidate structures as functions of pressure, relative to the enthalpy of $P2_1/n$ (β-diborane). All enthalpies are calculated using the PBEsol functional.

In order to facilitate comparison with experiment, the Raman and IR spectra of the 10 candidate structures were calculated at the specific pressures for which the experimental data of Refs. [8] and [7] are available. It should be kept in mind that, at room temperature, diborane remains in the liquid state until ∼3.5 GPa, [8, 7] so the experimental spectra recorded below this pressure cannot be directly compared to our calculations.

2.2.1 Raman spectra

All experimental Raman spectra shown in this work are composite; that is, each was formed by combining three separate spectral regions from the original experimental work of Ref. [7]: 100−1300, 1400−2400, and 2500−3000 cm^{-1}. The spectral region between 1300 and 1400 cm^{-1} was excluded because of intense Raman scattering by the diamond of the anvil cell. In the resulting composite spectra, arbitrary peak intensities within each window were scaled to approximately match the distribution of peak intensities in the simulated spectra. Frequencies below 700 cm^{-1} correspond to lattice modes; frequencies above 700 cm^{-1} are due to internal molecular vibrations.

Murli and Song [7] found that the lowest-pressure solid phase of diborane (phase I) exists at room temperature between 3.5 and about 6 GPa. To identify this phase, we computed the Raman spectra of all candidate structures at 4.2 GPa and compared them to the experimental Raman spectrum recorded at the same pressure. The best agreement was found for β-diborane ($P2_1/n$), as shown in Figure 2.4.

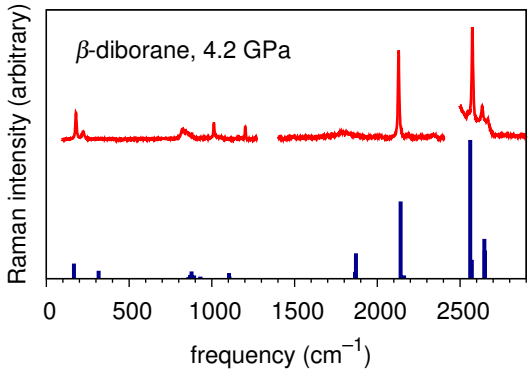

Figure 2.4: Experimental (red) and simulated (blue) Raman spectra of β-diborane at 4.2 GPa.

The most intense peaks in Figure 2.4 correspond to the terminal B−H symmetric stretching mode. In the calculated spectrum, it occurs at 2562 cm^{-1} compared with

2574 cm^{-1} in the observed spectrum. The second most intense peak corresponds to the symmetric BHBH ring stretching; it occurs at a lower frequency of 2141 cm^{-1}, compared to the experimental value of 2128 cm^{-1}. The calculated depolarization ratio of these two modes is close to zero, as anticipated for totally symmetric modes. The antisymmetric terminal BH stretching is calculated to occur at 2647 cm^{-1}, in good agreement with the experimental value of 2633 cm^{-1}. The ring antisymmetric stretching mode is predicted to occur at 1871 cm^{-1} and was observed at 1813 cm^{-1}. Two lattice modes observed [7] at 179 and 222 cm^{-1} are reproduced in our simulation at 167 and 246 cm^{-1}, respectively.

We note that the simulated Raman spectra of $P2_1/c$ (**A**) and $P2_1/c$ (**B**) diboranes are similar to the experimental spectrum at 4.2 GPa, but we rule out these structures because they have no lattice modes below 200 cm^{-1} (Figure 2.5). The simulated spectra of the other seven candidate structures clearly do not match the experiment. The trimer and linear-chain structures consist of different molecular units, so their internal vibrational modes are very different from those of diborane molecules (Figure 2.5). All this allows us to conclude that phase I of Ref. [7] is β-diborane.

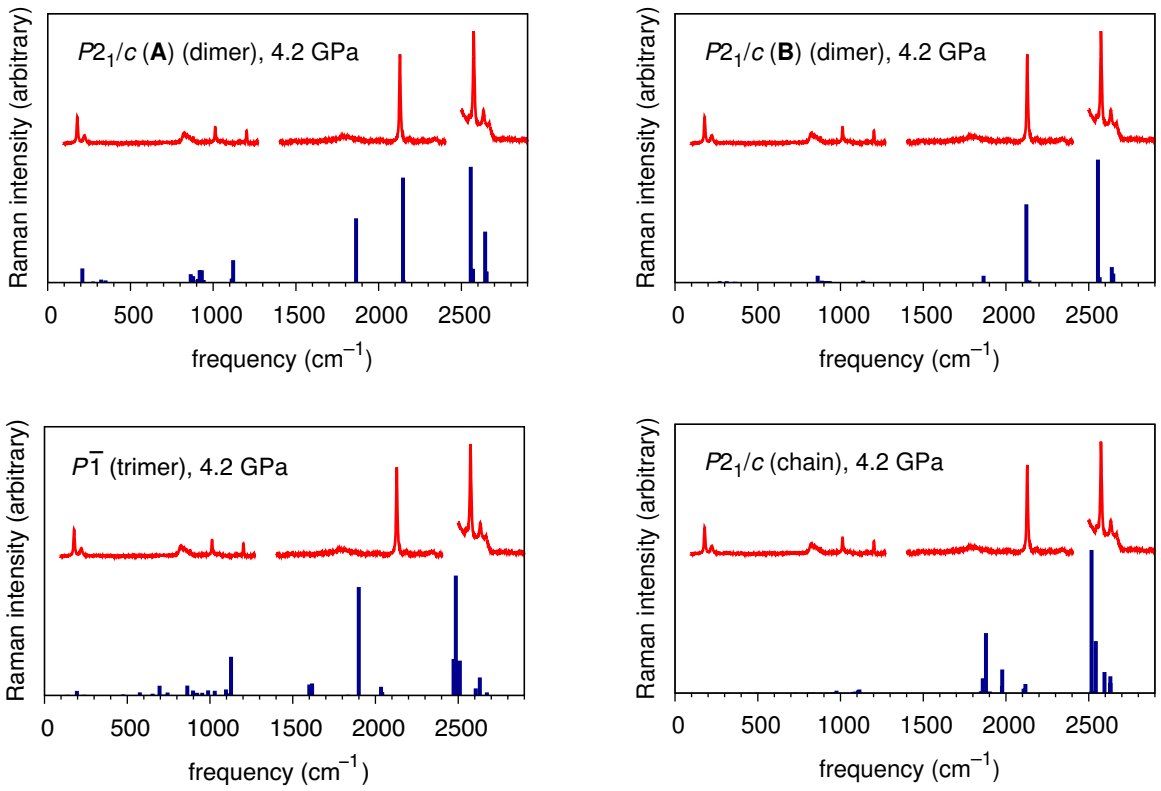

Figure 2.5: Experimental (red) and simulated (blue) Raman spectra of $P2_1/c$ (**A**) and $P2_1/c$ (**B**) dimers, $P\bar{1}$ trimer, and $P2_1/c$ chain at 4.2 GPa.

Upon compression of the sample to 6.4 GPa, Murli and Song [7] observed the emergence of several new lattice and internal modes and interpreted them as evidence of a polymorphic transition from β-diborane to another phase referred to as phase II. As we argue below, these spectral changes are best reproduced by the calculated Raman spectrum of $P2_1/c$ (**A**) diborane. Just like β-diborane, the $P2_1/c$ (**A**) structure contains two B_2H_6 molecules per unit cell but has a different stacking of diborane molecules, depicted in Figure 2.6.

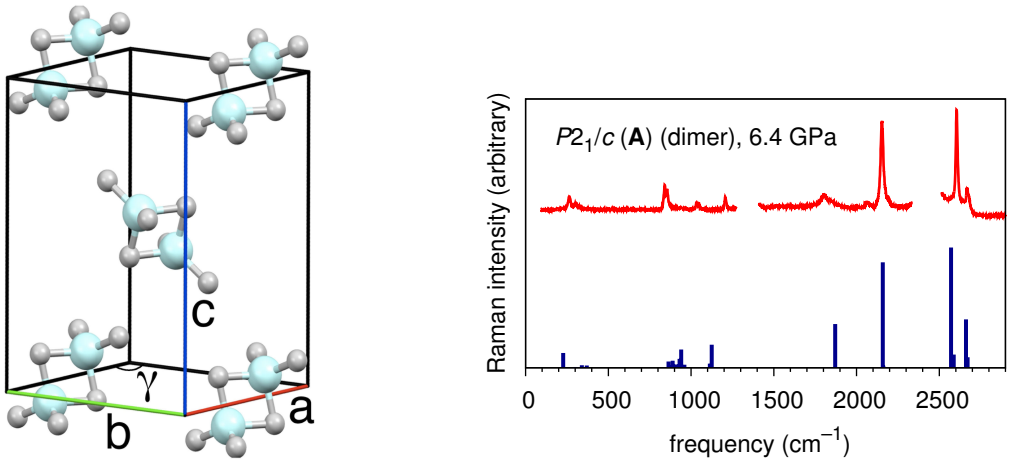

Figure 2.6: Left: structure of $P2_1/c$ (**A**) diborane at ambient pressure ($a = 4.519$, $b = 4.725$, $c = 8.874\,\text{Å}, \gamma = 120.0$). The lattice parameters were optimized using the PBEsol functional. Right: experimental (red) and simulated (blue) Raman spectra of $P2_1/c$ (**A**) diborane at 6.4 GPa.

Figure 2.6 also shows the calculated Raman spectrum of $P2_1/c$ (**A**) diborane at 6.4 GPa along with the experimental spectrum of the sample taken at the same pressure [7]. The experimental spectrum has two low-intensity lattice modes at 326 and 367 cm^{-1} which were not present at 4.2 GPa. These modes are found in the simulated spectrum of $P2_1/c$ (**A**) diborane at 340 and 370 cm^{-1}. The lattice mode observed at 265 cm^{-1} is no longer found in the simulated spectrum of β-diborane at 6.4 GPa but corresponds nicely to the peak at 227 cm^{-1} in the calculated spectrum of $P2_1/c$ (**A**) diborane. The calculated spectrum also contains a BH_2 twisting mode at 864 cm^{-1}, a BH_2 wagging mode at 931 cm^{-1}, and two low-intensity modes at 886 and 912 cm^{-1}. These correspond to the experimentally observed modes at 855, 907, 936, and 962 cm^{-1} [7]. No other candidate structure has a Raman spectrum that matches experiment better than this.

The above evidence strongly suggests that phase II is $P2_1/c$ (**A**) diborane. The transition from β-diborane to this phase occurs around 6 GPa. Note that Yao and Hoff-

mann [9] have previously identified $P2_1/c$ (**A**) diborane with the phase observed in 1925 by Mark and Pohland [4]. We therefore propose that phase II observed by Murli and Song [7] is the phase of Mark and Pohland. This is despite the fact that, according to the PBE calculations of Yao and Hoffmann [9] and to our PBEsol calculations (Figure 2.3), $P2_1/c$ (**A**) diborane is slightly less stable than β-diborane, $P2_1/c$ (**B**) diborane, and the trimer structures at pressures between 1 and 80 GPa.

At pressures above 14 GPa, another phase transition was proposed in Ref. [7] to account for several subtle changes in the Raman spectrum. However, the experimental spectrum of diborane recorded at 14.1 GPa (after the proposed phase transition has occurred) is still well matched by the simulated spectrum of $P2_1/c$ (**A**) diborane (Figure 2.7).

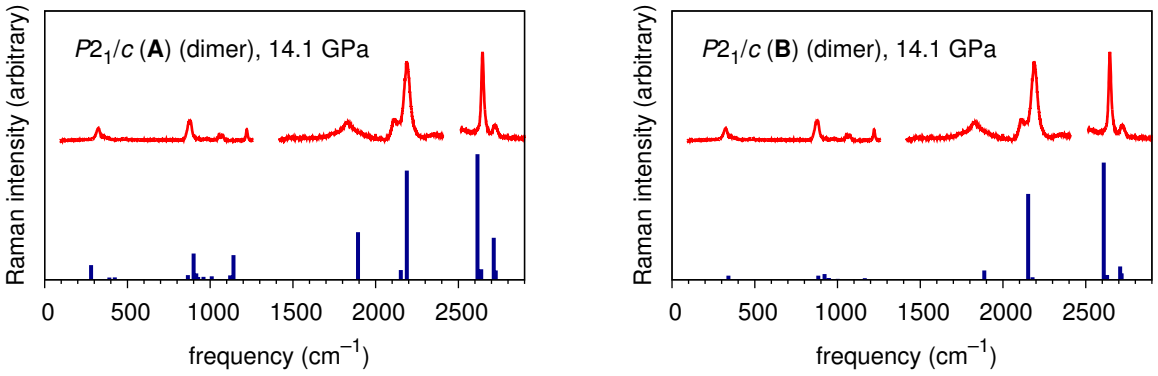

Figure 2.7: Experimental (red) and simulated (blue) Raman spectra of $P2_1/c$ (**A**) and $P2_1/c$ (**B**) diboranes at 14.1 GPa.

Note that all three dimer structures considered in this work (β-diborane and the two $P2_1/c$ diboranes) have very similar internal vibration modes, so their spectra differ mainly by the positions of lattice modes. The greatest discrepancy between the calculated and observed spectra of $P2_1/c$ (**A**) diborane at 14.1 GPa is in the position of the first lattice mode, which in our calculation occurs at 281 cm^{-1}, while the experimental one is at 323 cm^{-1}. This lattice mode is more closely matched in the simulated spectrum of $P2_1/c$ (**B**) diborane, where it occurs at 341 cm^{-1}. At 20.0 GPa, the first observed lattice mode shifts to 361 cm^{-1}, whereas the first lattice modes in the simulated Raman spectra of structures **A** and **B** are found at 298 and 359 (or possibly 337) cm^{-1}, respectively. Thus, if a phase transition above 14 GPa does take place, it is from $P2_1/c$ (**A**) diborane (phase II) to $P2_1/c$ (**B**) diborane (phase III). The structure of the latter is shown in Figure 2.8.

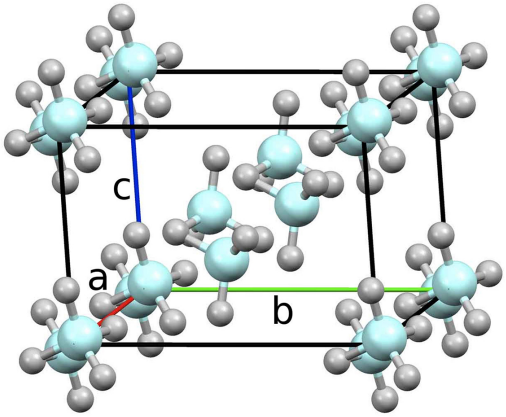

Figure 2.8: Structure of $P2_1/c$ (**B**) diborane at ambient pressure ($a = 4.577$, $b = 6.954$, $c = 4.998\,\text{Å}, \gamma = 95.8°$). The lattice parameters were optimized using the PBEsol functional.

To investigate the remaining possibility that the phase existing above 14 GPa consists of $(BH_3)_n$ units with $n > 2$, we calculated the Raman spectra of all candidate structures at 20.0 GPa and compared them to the experimental spectrum of the sample recorded at the same pressure. At 20.0 GPa, the simulated Raman spectrum of $P2_1/c$ (**A**) diborane remains the best match with experiment, although the $P2_1/c$ (**B**) structure cannot be ruled out (Fig. 2.9). At the same time, the spectra of the trimer and linear chain structures are not even close to experiment (Fig. 2.10). We conclude that the subtle changes in the observed Raman spectra of diborane above 14 GPa are most likely consequences of the compression of $P2_1/c$ (**A**), but allow for the possibility that $P2_1/c$ (**A**) diborane transforms near 14 GPa into $P2_1/c$ (**B**) diborane.

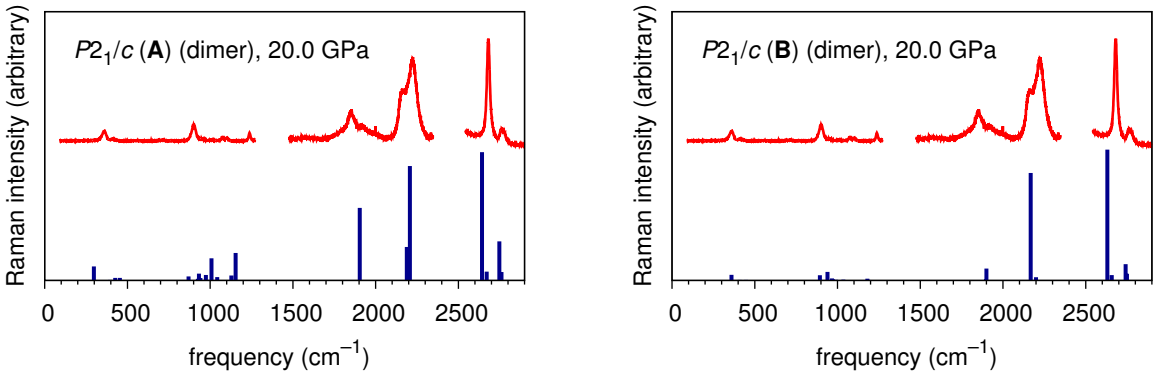

Figure 2.9: Experimental (red) and simulated (blue) Raman spectra of $P2_1/c$(**A**) and $P2_1/c$(**B**) dimers at 20.0 GPa.

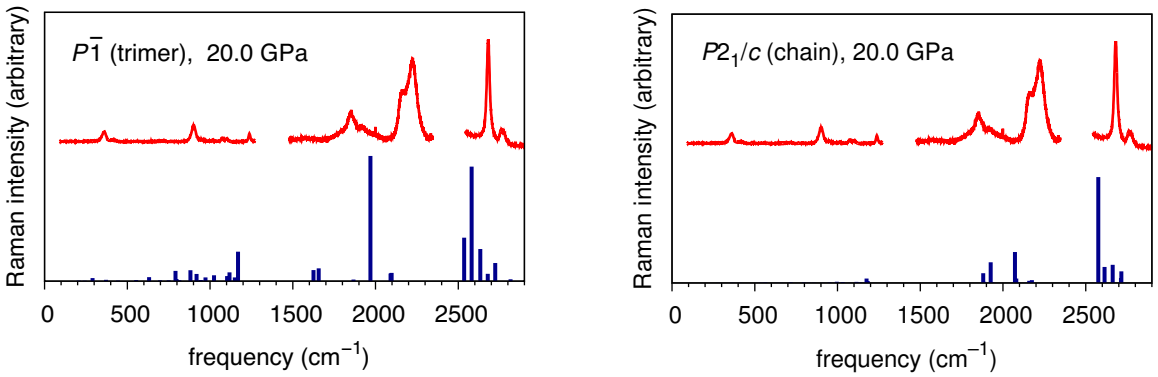

Figure 2.10: Experimental (red) and simulated (blue) Raman spectra of $P\bar{1}$ trimer and $P2_1/c$ chain at 20.0 GPa.

2.2.2 Infrared spectra

To provide additional evidence supporting our structural assignments, we also simulated infrared absorption spectra of compressed diborane and compared them to the published infrared spectra from the Song group [8]. Note that Ref. [8] did not report infrared absorption data for frequencies below 800 cm^{-1}. Also, the broad band appearing above 3700 cm^{-1} in all experimental infrared spectra of Ref. [8] is associated with overtones or combination modes [8], so it is absent from the simulated spectra which show only fundamental transitions.

The experimental infrared spectrum recorded at 5.4 GPa is well matched by the simulated spectrum of β-diborane, as shown in Figure 2.11.

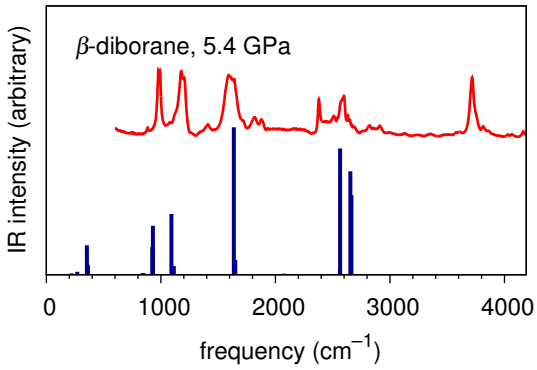

Figure 2.11: Experimental (red) and simulated (blue) infrared spectra of β-diborane at 5.4 GPa.

The most intense peak in the simulated spectrum occurs at 1637 cm^{-1}, accompanied by a low-intensity mode at 1650 cm^{-1}. This pair matches the split band observed near

1600 cm^{-1} in the experimental spectrum. Two internal modes occur in the simulated spectrum at 930 and 1092 cm^{-1}, respectively, compared to 980 and 1176 cm^{-1} in the experimental spectrum. The simulated terminal BH symmetric stretching and antisymmetric BH stretching modes at 2565 and 2655 cm^{-1} likely correspond to the experimental peaks at 2598 and 2630 cm^{-1}, respectively. The high-intensity band at 2379 cm^{-1} is due to overtones/combination modes [8], so it is not present in the simulated spectrum. The simulated infrared spectra of trimer and chain structures agree poorly with the experimental spectrum at 5.4 GPa. Thus, our simulated infrared data are consistent with the conclusion that at 5.4 GPa diborane exists in the form of the β-phase (phase I).

Upon compression above 6 GPa, the best match between the calculated and experimental infrared spectra is found for $P2_1/c$ (**A**) diborane (phase II), as was the case with the Raman spectra. The experimental and simulated spectra of $P2_1/c$ (**A**) diborane at 6.9 GPa are compared in Figure 2.12. The simulated spectrum reproduces most of the features noted in Ref. [8] including the evolution of a shoulder band near 1100 cm^{-1} and a more pronounced separation of the two peaks near 1630 cm^{-1}.

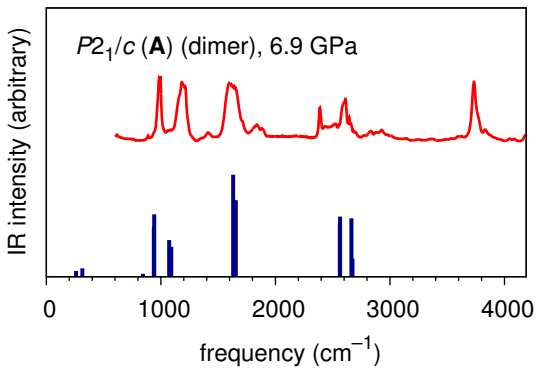

Figure 2.12: Experimental (red) and simulated (blue) infrared spectra of $P2_1/c$ (**A**) diborane at 6.9 GPa.

As in the Raman spectroscopic studies, the subtle differences between the experimental spectra taken at 6.9 GPa and above 14 GPa were interpreted by Song et al. [8] as evidence of a polymorphic transition from phase II to phase III. These difference include the emergence of a new mode near 2760 cm^{-1}, development of an asymmetric profile of a mode near 1000 cm^{-1}, and an enhanced splitting of a mode near 1200 cm^{-1}. These changes are consistent with the simulated infrared spectrum of $P2_1/c$ (**A**) diborane at 16.7 GPa and, to a lesser degree, with the spectrum of $P2_1/c$ (**B**) diborane (see Figure 10). The latter possibility cannot be ruled out because of the similarity

between the infrared spectra of these two structures.

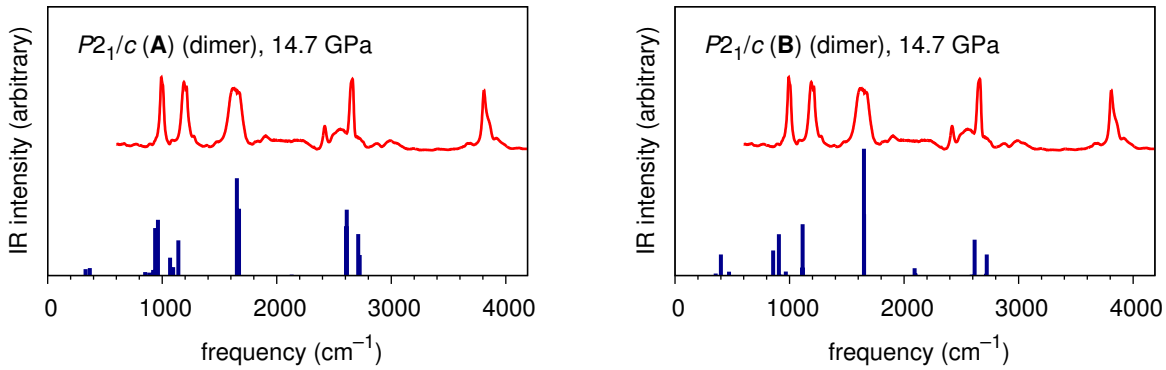

Figure 2.13: Experimental (red) and simulated (blue) infrared spectra of $P2_1/c$ (**A**) and $P2_1/c$ (**B**) diboranes at 16.7 GPa.

Infrared spectra of crystalline triboranes and chain structures differ starkly from the experimental spectra recorded above 14 GPa. This again means that the high-pressure phases observed by the Song group are not oligomer or polymer structures. Thus, the spectral changes observed above 14 GPa are most likely consequences of compression of $P2_1/c$ (**A**) diborane. No other polymorphic transitions between 14 and 24 GPa were observed or proposed in Ref. [8].

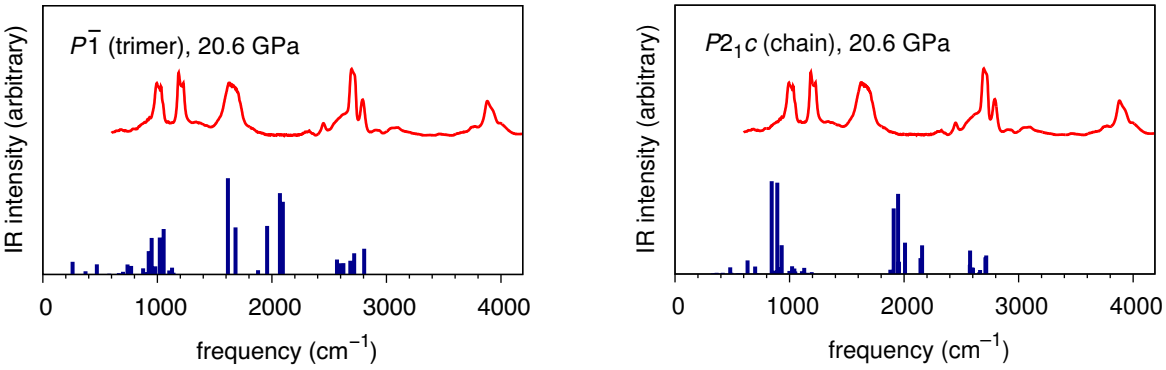

Figure 2.14: Experimental (red) and simulated (blue) infrared spectra of $P\bar{1}$ trimer and $P2_1/c$ chain at 20.6 GPa.

2.3 Conclusion

We have simulated the pressure dependence of Raman and infrared spectra of 10 plausible crystalline structures of boron hydride for which experimental data [7, 8] are

available. Comparison of the simulated spectra to the experiment shows (Figure 2.15) that boron hydride exists as β-diborane (phase I) until about 6 GPa when it transforms into $P2_1/c$ (**A**) diborane (phase II). The subtle spectral changes above 14 GPa, which were previously interpreted as an indication of another phase transition [7, 8], are attributed here to the compression of $P2_1/c$ (**A**) diborane. However, we do not rule out the possibility that near 14 GPa $P2_1/c$ (**A**) diborane is converted into $P2_1/c$ (**B**) diborane (phase III). This ambiguity is due to the fact that the simulated spectra of $P2_1/c$ (**A**) and $P2_1/c$ (**B**) diboranes are similar. What is certain is that none of the structures built up of $(BH_3)_n$ units with $n > 2$ has a vibrational spectrum that is consistent with the experimental observations. Although the formation of cyclic oligomers and polymer chains is favored thermodynamically, it appears to be hindered kinetically. Our findings strongly agree with the conclusion of Refs. [7] and [8] that the geometry of the BHBH diborane ring is not altered significantly by compression and that B_2H_6 molecules remain chemically stable up to at least 24 GPa.

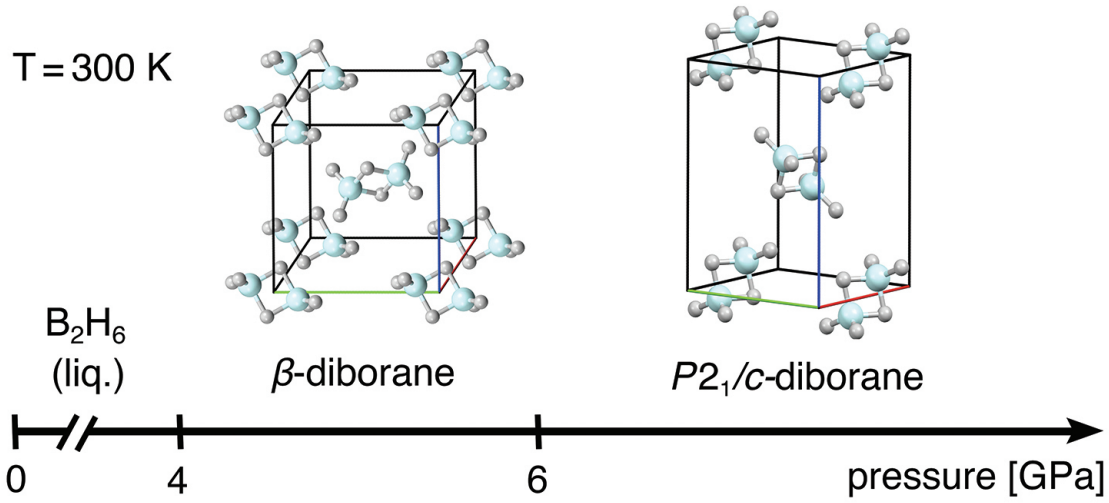

Figure 2.15: Pressure-induced polymorphic transitions in crystalline diborane.

Bibliography

[1] W. N. Lipscomb, *Boron Hydrides*, W. A. Benjamin: New York, **1963**.

[2] K. Abe, N. W. Ashcroft. "Crystalline diborane at high pressures". *Phys. Rev. B* **2011**, *84*, 104118.

[3] T. W. Barbee, A. K. McMahan, J. E. Klepeis, M. V. Schilfgaarde. "High-pressure boron hydride phases". *Phys. Rev. B* **1997**, *56*, 5148.

[4] H. Mark, E. Pohland. "IV. Über die gitterstruktur des äthans und des diborans". *Z. Kristallogr* **1925**, *62*, 103.

[5] L. H. Bolz, F. A. Mauer, H. S. Peiser. "Exploratory study, by low-temperature x-ray diffraction techniques, of diborane and the products of a microwave discharge in diborane". *J. Chem. Phys.* **1959**, *31*, 1005.

[6] H. W. Smith, W. N. Lipscomb. "Single-crystal x-ray diffraction study of β-diborane". *J. Chem. Phys.* **1965**, *43*, 1060.

[7] C. Murli, Y. Song. "Pressure-induced transformations in diborane: a Raman spectroscopic study". *J. Phys. Chem. B* **2009**, *113*, 13509.

[8] Y. Song, C. Murli, Z. Liu. "*In situ* high-pressure study of diborane by infrared spectroscopy". *J. Chem. Phys.* **2009**, *131*, 174506.

[9] Y. Yao, R. Hoffmann. "BH_3 under pressure: leaving the molecular diborane motif". *J. Am. Phys. Soc.* **2011**, *133*, 21002.

[10] P. Giannozzi, S. Baroni, N. Bonini, M. Calandra, R. Car, C. Cavazzoni, D. Ceresoli, G. L. Chiarotti, M. Cococcioni, I. Dabo, A. D. Corso, S. de Gironcoli, S. Fabris, G. Fratesi, R. Gebauer, U. Gerstmann, C. Gougoussis, A. Kokalj, M. Lazzer, L. Martin-Samos, N. Marzari, F. Mauri, R. Mazzarello, S. Paolini, A. Pasquarello, L. Paulatto, C. Sbraccia, S. Scandolo, G. Sclauzero, A. P. Seitsonen, A. Smogunov, P. Umari, R. M. Wentzcovitch. "QUANTUM ESPRESSO:

a modular and open-source software project for quantum simulations of materials". *J. Phys.: Condens. Matter* **2009**, *21*, 395502.

[11] D. Vanderbilt. "Soft self-consistent pseudopotentials in a generalized eigenvalue formalism". *Phys. Rev. B* **1990**, *41*, 7892.

[12] M. Lazzeri, F. Mauri. "First-principles calculation of vibrational Raman spectra in large systems: signature of small rings in crystalline SiO_2". *Phys. Rev. Lett.* **2003**, *90*, 036401.

[13] S. Baroni, S. de Gironcoli, A. D. Corso, P. Giannozzi. "Phonons and related crystal properties from density-functional perturbation theory". *Rev. Mod. Phys.* **2001**, *73*, 515.

[14] A. Kokalj. "Computer graphics and graphical user interfaces as tools in simulations of matter at the atomic scale". *Comput. Mater. Sci.* **2003**, *28*, 155.

Chapter 3

Polymorphic transitions of diborane at sub- and near-megabar pressures

3.0 Introduction

Chemical hydrides under extreme pressures have become the subject of explosive interest in recent years. Rich in elemental hydrogen, these materials offer attractive possibilities for high-density energy storage [11]. Being "chemically pre-compressed" [12], they also provide a practical route to achieving pressure-induced hydrogen metallization, a long-standing challenge of high-pressure physics. In this context, experimental and theoretical studies of compressed silane (SiH_4) and other hydrides have already yielded notable discoveries[13, 14, 15, 16, 17, 18, 19].

Diborane (B_2H_6), a peculiar electron-deficient molecule with bridging hydrogen atoms, is a chemical hydride that attracts much attention in high-pressure research [3, 4, 6, 7, 8, 20]. At ambient pressure and below 60 K, solid diborane crystallizes as an orthorhombic structure ($a = 7.89\,\text{Å}$, $b = 4.54\,\text{Å}$, $c = 8.69\,\text{Å}$, $Z = 4$) referred to as the α-phase, while annealing to above 90 K results in the formation of the β-phase (space group $P2_1/n$, $a = 4.40\,\text{Å}$, $b = 5.72\,\text{Å}$, $c = 6.50\,\text{Å}$, $\gamma = 105.1°$) [5, 22]. Song and co-workers [7, 6] were the first to report intriguing pressure-induced phase transitions in diborane. Specifically, they found that diborane progresses through three crystal structure phases (labeled I, II, and III) in the pressure region between 3.5 GPa (the liquid−solid boundary at room temperature) and 24 GPa. Using density-functional calculations, Torabi *et al.* [20] identified phase I with the β-diborane structure and

found that phases II (formed at 6 GPa) and possibly phase III (formed at 14 GPa) both have monoclinic $P2_1/c$ structures differing by molecular orientations. Abe and Ashcroft [3] used density-functional theory to show that diborane is thermodynamically unstable with respect to decomposition into B and H between 40 and 350 GPa, but also predicted that the metastable B_2H_6 structures should become metallic around 160 GPa. Yao and Hoffmann [8] demonstrated the thermodynamic possibility of oligo- and polymerization of B_2H_6 units above 4 GPa. Torabi *et al.* [20] arrived at the same conclusions, but showed that phases II and III were still molecular crystals of B_2H_6. More recently, Hu *et al.* [21] suggested that B_2H_6 should decompose into BH and H_2 at 153 GPa and that the most stable structure of BH should become metallic at 168 GPa.

Despite these theoretical predictions, no direct evidence of non-dimer-based phases of boron hydride has been obtained to date due to experimental challenges in both sample confinement and *in situ* structural characterization under extreme pressures. In particular, it is very difficult to unambiguously locate atoms of light elements such as boron and hydrogen by X-ray diffraction. As a result, the structure of compressed diborane have remained controversial. Here we report the first experimental evidence of new polymorphs of diborane using an alternative yet highly sensitive spectroscopic probe in a wide pressure regime approaching one megabar, which is unprecedented for this class of compounds. Our interpretation of the experimental data using electronic structure calculations suggests that B_2H_6 molecular units persist beyond 100 GPa, but transform into one-dimensional $(BH_3)_n$ chains near 110 GPa, and that the latter polymorph becomes metallic at even higher pressures. These findings shed light on the previously unknown high-pressure structures of diborane and take us one step closer to solving the problem of hydrogen metallization.

3.1 Results

In situ Raman spectroscopy was used to monitor the structural changes as a function of pressure. The Raman spectra of diborane recorded upon compression at selected pressures between 36 and 88 GPa are presented in Figure 3.1.

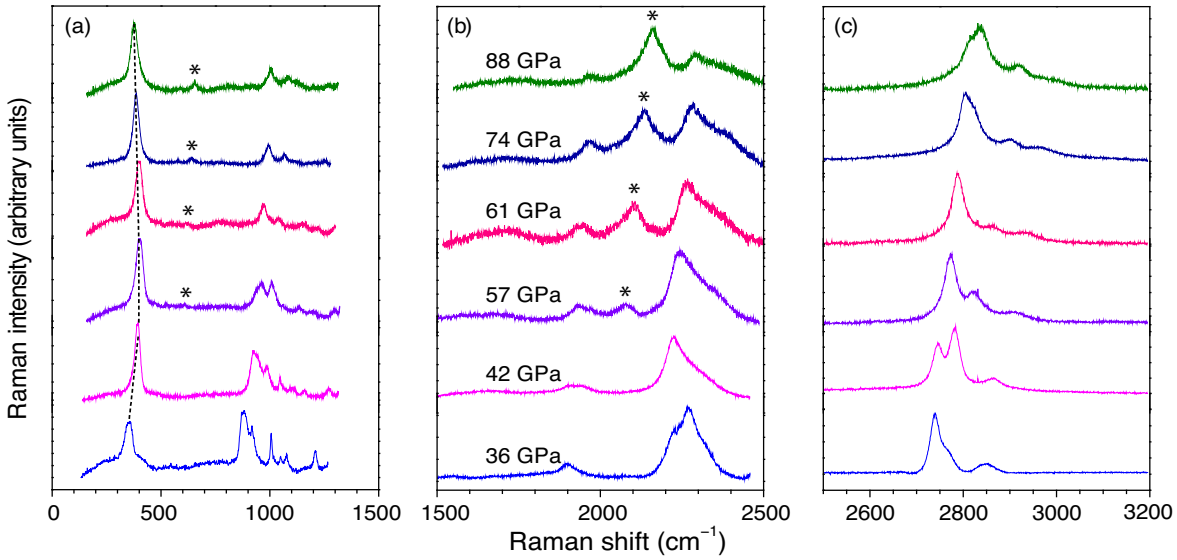

Figure 3.1: Experimental Raman spectra of compressed diborane, recorded in three frequency regions at selected pressures between 36 and 88 GPa. The dashed lines in panel (a) trace the soft behavior of the lattice mode. The asterisks label the new bands emerging near 57 GPa.

At the starting pressure of 36 GPa, we deal with the known phase III, $P2_1/c$, as evidenced by the fact that the experimental Raman profile of the sample at 36 GPa is best reproduced by the simulated Raman spectrum of phase III for the same pressure (Figure 3.2). The simulated Raman spectrum, in blue, is broadened using the Lorentzian scheme to better simulate the experimental spectrum.

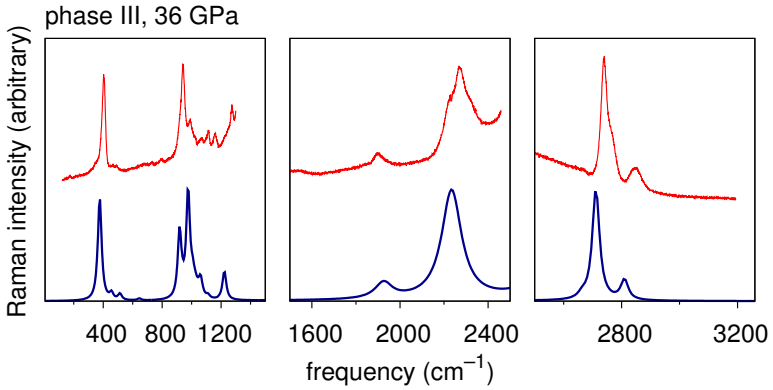

Figure 3.2: Experimental (red) and simulated (blue) Raman spectra of phase III at 36 GPa.

Upon compression of phase III to 42 GPa, most Raman modes below 2000 cm^{-1} blue-shift and broaden; other significant changes include a red shift and a profile

change of the symmetric ring-stretching mode near 2250 cm^{-1}, and the splitting of the terminal symmetric BH stretching mode (t-BH) near 2750 cm^{-1} (Figure 3.1). These observations suggest a polymorphic transition at 42 GPa to a new phase, which we label phase IV.

Upon compression of phase IV to 57 GPa, another set of prominent changes was observed. The first of these is the appearance of two new Raman modes near 600 and 2100 cm^{-1}, which are marked with asterisks in Figure 3.1. With increasing pressure, the latter mode evolves into a very intense band. More interestingly, the doublet of the terminal BH symmetric stretching mode near 2750 cm^{-1} undergoes an intensity reversal between the two components at 57 GPa. Finally, the lowest-frequency lattice mode exhibits a soft turning behavior near 57 GPa, which is usually indicative of a phase transition. These observations suggest that another phase is formed near 57 GPa, which we label phase V. Given the similarity in Raman profiles recorded between 57 and 88 GPa, we conclude that no other phase transition occurs in that pressure range.

Further experimental evidence of the formation of phases IV and V is provided by the pressure-dependence plots for Raman shifts, shown in Figure 3.3.

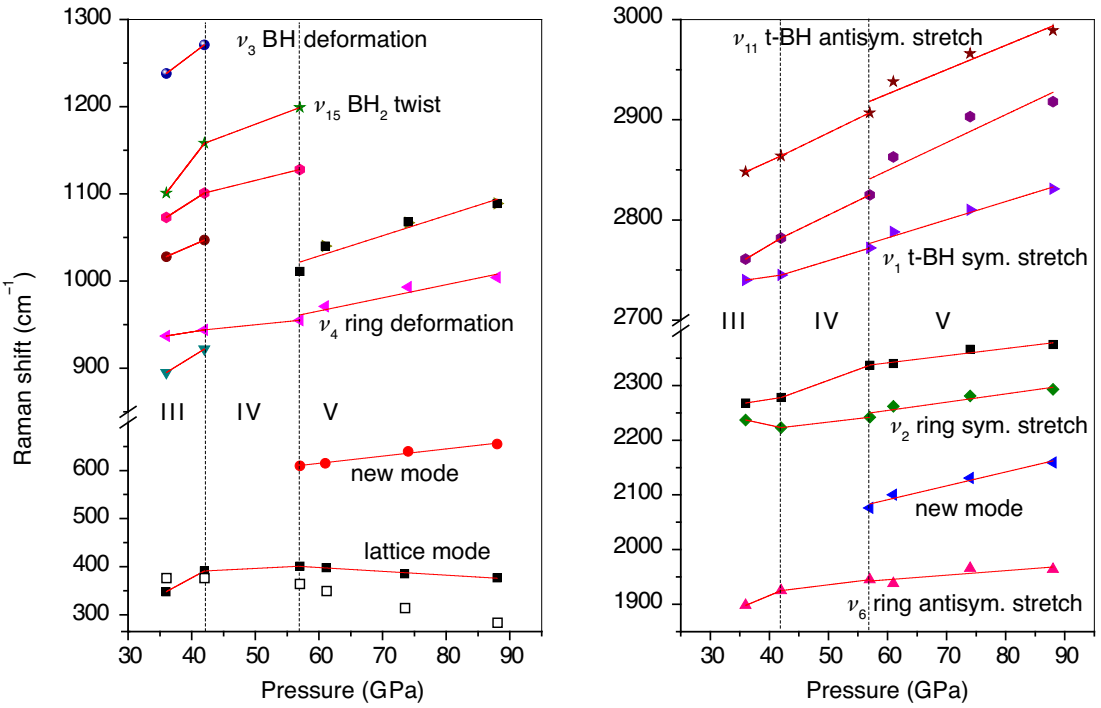

Figure 3.3: Experimental Raman shifts of compressed diborane as functions of pressure. The calculated frequencies of the lattice mode are shown in the left panel as open squares. t-BH stands for terminal B−H bond.

These plots reveal two phase boundaries in the 36−88 GPa range: one at 42 GPa and another at 57 GPa, denoted by the vertical dashed lines. Note that in the previous experimental studies [7] of compressed diborane using infrared spectroscopy at pressures up to 50 GPa, a phase transition near 42 GPa was not observed. This is not inconsistent with the present findings because infrared absorption bands at pressures above 30 GPa were so broad that infrared data alone could neither indicate nor rule out a phase transition.

To assign possible crystal structures to phases IV and V, we proceeded as follows. First, we ran the evolutionary structure search algorithm of Oganov and co-workers [2, 23, 24] to generate candidate crystal structures of the empirical formula BH_3 for pressures of 30, 60, and 90 GPa. The only information used on input was that there are either 4 B and 12 H atoms or 6 B and 18 H atoms in a unit cell; no constraints were imposed on the type or number of bonds between the atoms. These runs produced a total of 5502 candidate structures. Out of these, we selected by inspection a short list of 134 candidates by keeping the structures that had either a low enthalpy or a high symmetry. To maintain diversity, we included comparable numbers of structures with two, three, or four B atoms per molecular unit (36, 18, and 21 structures, respectively), as well as 59 polymers of BH_3 units. Then we optimized the lattice parameters and atomic coordinates of each of these 134 structures at the corresponding experimental pressure (36, 42, 57, 61, 74 and 88 GPa), and calculated their Raman spectra at each pressure point.

By comparing the observed Raman spectra of phases IV and V to the simulated spectra of these 134 candidate structures, we found two best matches which correspond to the structures shown in Figure 3.4.

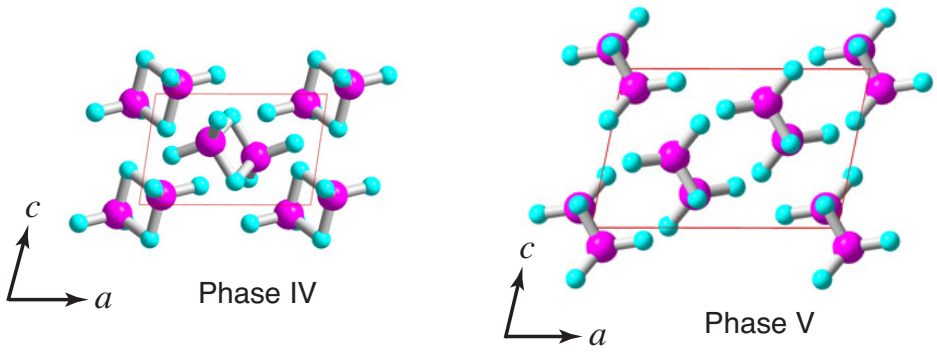

Figure 3.4: Structures assigned to phases IV and V.

The structure assigned to phase IV has a triclinic unit cell ($P\bar{1}$) with two B_2H_6 units

per cell ($Z = 2$), almost perpendicular to each other. The cell parameters of phase IV at 42 GPa calculated using PBEsol functional are $a = 4.740\,\text{Å}$, $b = 4.425\,\text{Å}$, $c = 3.217\,\text{Å}$, $\alpha = 73.37°$, $\beta = 97.41°$, and $\gamma = 87.56°$. The structure assigned to phase V also has a triclinic cell ($P\bar{1}$) but with $Z = 3$; here the B_2H_6 molecules form a layered structure with B or H atoms roughly aligned in the [101] direction. The cell parameters of phase V at 88 GPa calculated using PBEsol functional are $a = 6.216\,\text{Å}$, $b = 3.060\,\text{Å}$, $c = 4.350\,\text{Å}$, $\alpha = 69.90°$, $\beta = 78.75°$, and $\gamma = 89.81°$.

The experimental and simulated Raman spectra of phases IV at 42 GPa, and phase V at 57, 61, 74 and 88 GPa are shown in Figure 3.5.

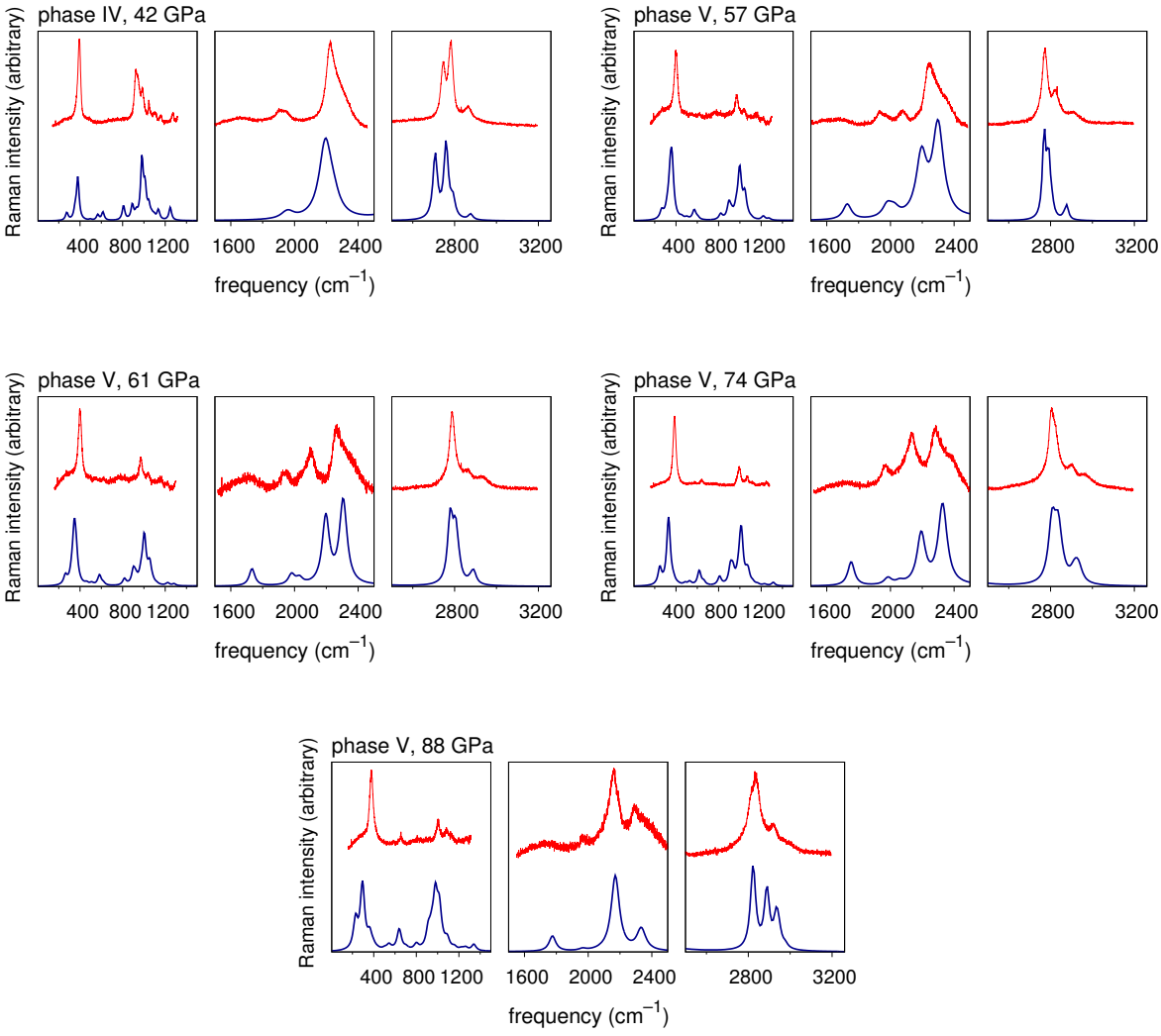

Figure 3.5: Experimental (red) and simulated (blue) Raman spectra of phases IV at 42 GPa and phase V at 57, 61, 74 and 88 GPa.

The simulated Raman spectra exhibit most of the essential features of the experimental

profiles of Figure 3.1, including a number of important details. In particular, the soft behavior of the lowest-frequency lattice mode is qualitatively reproduced by our calculations (Figure 3.3). The new modes near 600 and 2200 cm^{-1} at pressures of 57 GPa and higher (those labeled with asterisks in Figure 3.1) are unambiguously present in the simulated spectra. Also reproduced are the complex features corresponding to the ring vibrations in the spectral region of 800−1300 cm^{-1} as well as the reversal of relative intensities of the terminal BH symmetric stretching modes near 2800 cm^{-1}, which occurs between 42 and 57 GPa (Figure 3.1). The experimental and simulated relative intensities of the dominant peaks near 2200 and 2400 cm^{-1} are consistent at both 42 and 88 GPa. Although only one prominent lattice mode is observed near 400 cm^{-1} at 88 GPa, the simulated spectra suggest that the broad base of this intense mode contains other lattice vibrations (Figure 3.5). All these facts strongly support the proposed structural assignments to phases IV and V. No other of the 134 crystal structures matched the experimental Raman spectra of phases IV and V nearly as well as the structures shown in Figure 3.4. Because the structure of phase V matches the experimental Raman spectra of compressed diborane not only at 57 GPa but also at every higher pressure, we conclude that no other phase transitions occur between 57 and 88 GPa, and that diborane remains in molecular form up to at least 88 GPa.

More evidence supporting our identification of phases III−V is provided by enthalpy calculations using the PBEsol functional (Figure 3.6).

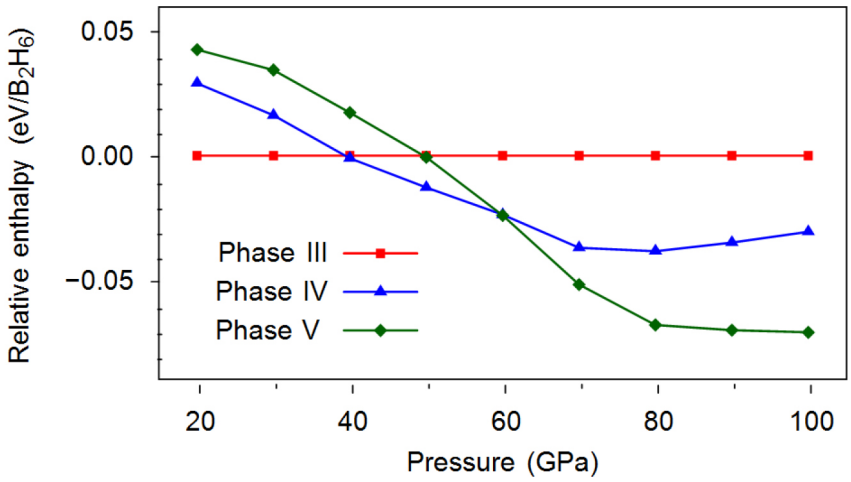

Figure 3.6: Calculated enthalpies of phases IV and V relative to phase III. All enthalpies are calculated using the PBEsol functional.

Although PBEsol was specifically developed to produce more accurate structural parameters than PBE at the expense of less accurate energies (at least at ambient pressure), we observed here and earlier in Ref. [20] that the relative PBEsol enthalpies of various high-pressure polymorphs of diborane are nearly the same as those predicted with the PBE functional. According to PBEsol, phase III is the most stable among the three up to about 40 GPa, phase IV is the most stable from ∼40 to ∼60 GPa, and phase V is the most stable from ∼60 up to at least 100 GPa. The crossover points near 40 and 60 GPa are in good agreement with the experimentally deduced phase boundaries at 42 and 57 GPa (Figure 3.6).

Interestingly, none of the phases III−V is thermodynamically the most stable structure among the 5502 candidate structures studied in this work at any pressure between 20 and 100 GPa. The candidate structure with the lowest enthalpy proved to be a $Pca2_1$ phase of BH and H_2 (Figure 3.7), whose boron-containing units resemble the *Ibam* phase reported by Hu *et al.* [21].

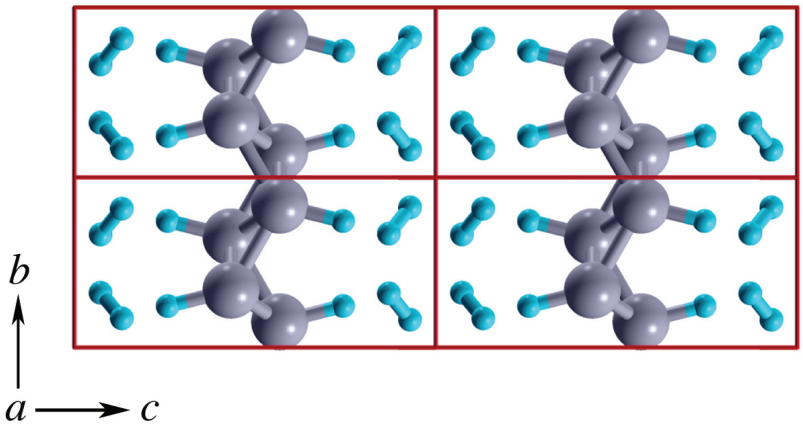

Figure 3.7: The lowest-enthalpy structure ($Pca2_1$).

It is likely that dispersion interactions between diborane molecules also play a role in determining the relative stability of various polymorphs. However, because dispersion corrections usually rely on empirical short-range damping functions developed for systems where interatomic distances are not too short, we deemed it unsafe to apply those corrections to highly compressed structures.

PBEsol phonon calculations for phase IV at 42 GPa and phase V at 57, 61, 74, and 88 GPa revealed no imaginary frequencies at any of these pressures. The absence of imaginary frequencies indicates that the proposed structures of phases IV and V are dynamically stable and genuine minima (Figure 3.8).

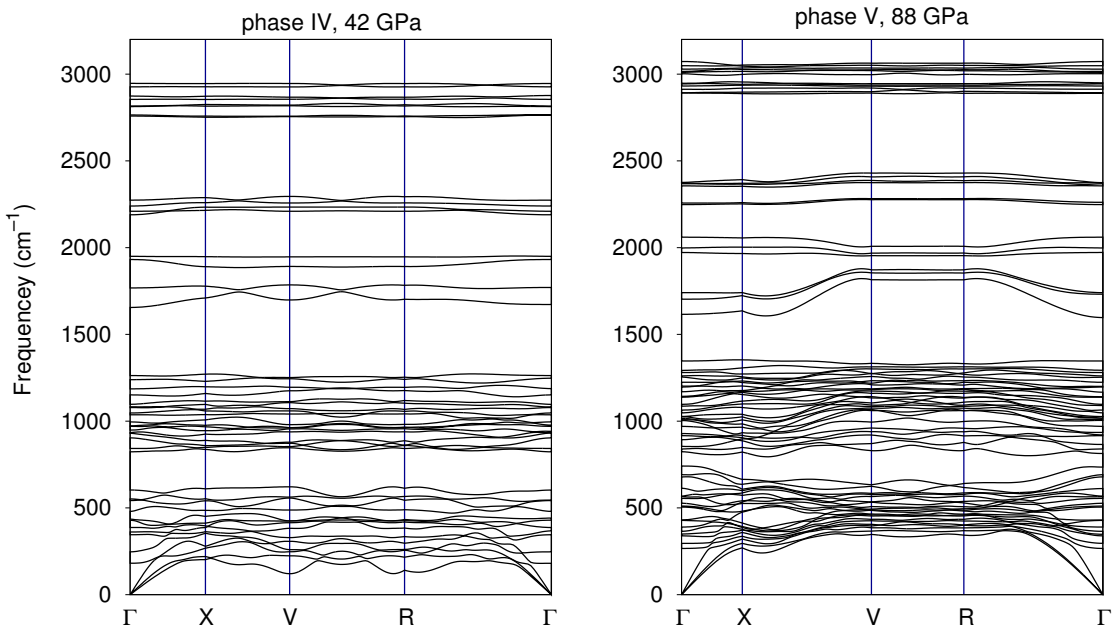

Figure 3.8: Phonon dispersions, calculated using the PBEsol functional, for phase IV at 42 GPa, and phase V at 88 GPa.

As an extra assurance of our structural assignments, we calculated and plotted the average volume per B_2H_6 unit for the proposed structures of phases III−V at various pressures. The resulting plots (Figure 3.9) exhibit two volume contractions with ratios of 1.84% and 1.43% at 42 and 57 GPa, respectively, which are consistent with pressure-induced polymorphic transitions.

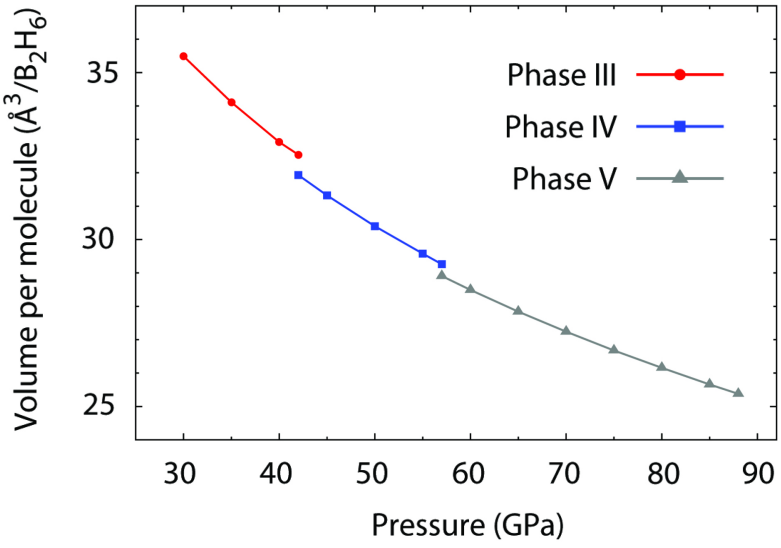

Figure 3.9: Calculated volume per B_2H_6 unit as a function of pressure. The volumes are calculated for the PBEsol structures optimized at a fixed pressure.

3.2 Discussion

Our experiments and calculations strongly suggest that diborane remains in the molecular crystal form over an extended pressure range from 3.5 GPa to at least 88 GPa. At the same time, the soft behavior of the lattice mode in phase V hints at the possibility of upcoming structural changes at even higher pressures. Of particular interest in this regard are the two long-standing questions: 1) whether diborane eventually leaves the molecular B_2H_6 motif and forms polymeric boron hydride [8]; 2) whether sufficiently compressed diborane becomes metallic [3].

To address the first of these questions, we explored the behavior of phase V at pressures above 88 GPa using the PBEsol method. We found that, between 88 GPa and 110 GPa, the crystal structure of phase V changes continuously, but still can be described as consisting of B_2H_6 molecules. Near 110 GPa, however, it finally leaves the molecular diborane motif and is best described as consisting of one-dimensional zigzag chains of boron atoms. This transformation is evidenced by the disappearance of B−B bond length alternation and by the absence of identifiable molecular units in plots of the electron localization function [25] (Figure 3.10).

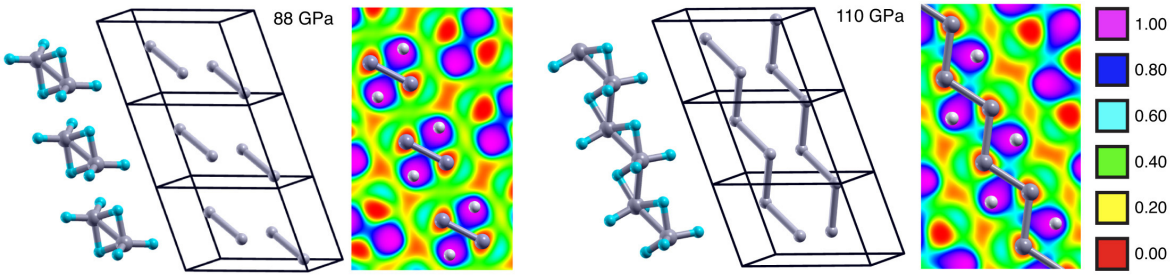

Figure 3.10: Units cells of phase V at 88 GPa (left) and 110 GPa (right) and the corresponding ELF plots are shown for the plane containing the right B-atom chain. The ELF is calculated using the HSE06 functional for the PBEsol-optimized structures. B−B bonds inside the unit cells are shown as sticks; H atoms inside the unit cells are removed for clarity.

In particular, the B−B distances in zigzag chains along the b axis alternate between 1.605 Å and 2.084 Å at 88 GPa, whereas all B−B bond lengths in the chains are 1.716 Å at 110 GPa. Also shown in Fig. 6 are the corresponding plots of the electron localization function (ELF) for the plane containing a B atom chain. The areas with low ELF values represent the B atoms; the areas with high values represent the H atoms. Note that, at 88 GPa, there are two bridging H atoms in the plane for every

two B atoms, but at 138 GPa one of those bridging H atoms moves out of the plane, but each B atom at 110 GPa is still coordinated by four H atoms (Figure 3.10).

To investigate the possibility of pressure-induced metallization of compressed diborane, we calculated the band gaps, the total and projected density of states of phase V in the 36−150 GPa pressure range using the Heyd–Scuseria–Ernzerhof (HSE06) screened hybrid density functional, known for realistic band gap predictions. These calculations show that at 88 GPa, phase V is a semiconductor with a band gap of 1.6 eV. The band gap gradually decreases with increasing pressure and finally closes near 138 GPa (Figure 3.11), resulting in a nonzero total density of states at the Fermi level (Figure 3.12).

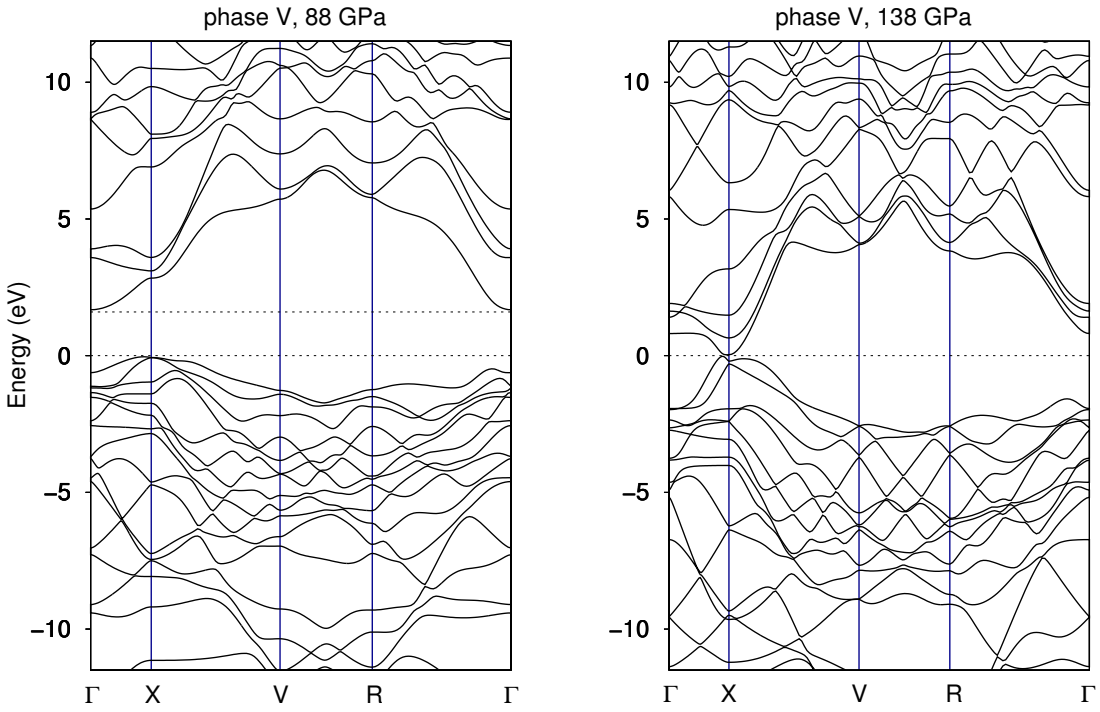

Figure 3.11: Band structure of phase V, calculated at 88 and 138 GPa. The unit cell parameters are optimized at each pressure using the PBEsol functional, the electronic energy bands are calculated using the HSE06 functional. Horizontal dashed lines represent the top of the valence band and the bottom of the conduction band

Analysis of the projected density of states plot (Figure 3.12) reveals that the main contribution to the metallization is from the boron's $2p$ orbitals. Although extremely experimentally challenging, *in situ* conductivity measurements would be needed to characterize the electronic properties of diborane at high pressures in the future.

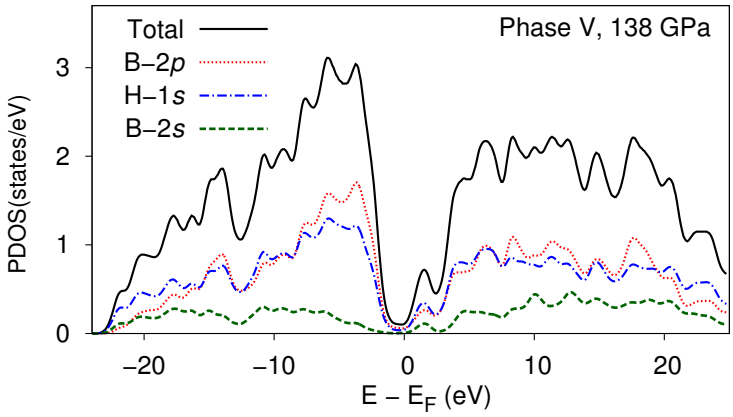

Figure 3.12: Total and projected density of states, calculated using HSE06 functional, for phase V optimized at 138 GPa using PBEsol functional.

3.3 Conclusion

In summary, we have reported and interpreted two previously unknown polymorphic transformations of compressed diborane occurring between 36 and 88 GPa. At the lower end of this pressure range, diborane exists in the form of phase III which transforms into phase IV near 42 GPa and then into phase V near 57 GPa. All these phases retain the diborane motif and are thermodynamically metastable. Future synchrotron and neutron-based *in situ* diffraction experiments should be able to verify these structure assignments and predictions. We also predict that phase V will remain in molecular form up to near-megabar pressures, above which it should transform into a structure with covalently bonded chains of boron atoms and eventually become metallic around 138 GPa. While such pressures have not yet been reached experimentally, they are feasible, which means that the first reports of pressure-induced polymerization and metallization of diborane are a matter of time.

3.4 Computational methodology

All candidate crystal structures of diborane were generated using the evolutionary structure search algorithm as implemented in the USPEX code [2, 23, 24]. The enthalpies of the structures at 0 K were used as a fitness criterion: the 40% least stable structures were discarded and the remaining was allowed to produce the next generation through heredity (60%), softmutation (20%) and lattice mutation (20%). Two

distinct lowest-enthalpy structures of each generation were allowed to survive into the subsequent one, and the runs were terminated after 50 generations. The enthalpy calculations were performed with the Quantum ESPRESSO program (version 5.0.1) [9]. Because Raman spectral intensities are implemented in Quantum ESPRESSO only for the local density approximation (LDA), we re-optimized all structures at the LDA level and calculated Raman frequencies and intensities using the LDA. The resulting vibrational frequencies were used without applying any scale factors. The pseudopotentials were taken from the Quantum ESPRESSO pseudopotential library. In the PBEsol calculations, PBE ultrasoft Vanderbilt pseudopotentials with a cutoff energy of 90 Ry were used. In the LDA calculations, the norm-conserving LDA pseudopotentials with a cutoff energy of 130 Ry were employed. The Brillouin zone was sampled using the homogeneous Monkhorst–Pack **k**-point meshes [1] with reciprocal space resolution of 0.08π Å^{-1}. The convergence criterion for Kohn–Sham self-consistency cycles was set to 10^{-8} Ry. All structure optimizations were performed using the Broyden−Fletcher−Goldfarb−Shanno quasi-Newton method [26]. The optimization was stopped when the components of all Hellmann–Feynman forces dropped below 10^{-4} Ry/Å and the stress on the cell was within 0.05 GPa of the target. The phonon frequency was obtained by diagonalization of the dynamical matrix calculated by the density-functional perturbation theory. The non-resonant Raman intensities were computed using the method described in Ref. [10].

Bibliography

[1] H. J. Monkhorst, J. D. Pack. "Special points for Brillouin-zone integrations". *Phys. Rev. B* **1976**, *13*, 5188.

[2] A. R. Oganov, C. W. Glass. "Crystal structure prediction using ab initio evolutionary techniques: Principles and applications". *J. Chem. Phys.* **2006**, *124*, 244704.

[3] K. Abe, N. W. Ashcroft. "Crystalline diborane at high pressures". *Phys. Rev. B* **2011**, *84*, 104118.

[4] T. W. Barbee, A. K. McMahan, J. E. Klepeis, M. V. Schilfgaarde. "High-pressure boron hydride phases". *Phys. Rev. B* **1997**, *56*, 5148.

[5] H. W. Smith, W. N. Lipscomb. "Single-crystal x-ray diffraction study of β-diborane". *J. Chem. Phys.* **1965**, *43*, 1060.

[6] C. Murli, Y. Song. "Pressure-induced transformations in diborane: a Raman spectroscopic study". *J. Phys. Chem. B* **2009**, *113*, 13509.

[7] Y. Song, C. Murli, Z. Liu. "*In situ* high-pressure study of diborane by infrared spectroscopy". *J. Chem. Phys.* **2009**, *131*, 174506.

[8] Y. Yao, R. Hoffmann. "BH_3 under pressure: leaving the molecular diborane motif". *J. Am. Phys. Soc.* **2011**, *133*, 21002.

[9] P. Giannozzi, S. Baroni, N. Bonini, M. Calandra, R. Car, C. Cavazzoni, D. Ceresoli, G. L. Chiarotti, M. Cococcioni, I. Dabo, A. D. Corso, S. de Gironcoli, S. Fabris, G. Fratesi, R. Gebauer, U. Gerstmann, C. Gougoussis, A. Kokalj, M. Lazzer, L. Martin-Samos, N. Marzari, F. Mauri, R. Mazzarello, S. Paolini, A. Pasquarello, L. Paulatto, C. Sbraccia, S. Scandolo, G. Sclauzero, A. P. Seitsonen, A. Smogunov, P. Umari, R. M. Wentzcovitch. "QUANTUM ESPRESSO: a modular and open-source software project for quantum simulations of materials". *J. Phys.: Condens. Matter* **2009**, *21*, 395502.

[10] M. Lazzeri, F. Mauri. "First-principles calculation of vibrational Raman spectra in large systems: signature of small rings in crystalline SiO_2". *Phys. Rev. Lett.* **2003**, *90*, 036401.

[11] Y. Song. "New perspectives on potential hydrogen storage materials using high pressure". *Phys. Chem. Chem. Phys.* **2013**, *15*, 14524.

[12] N. W. Ashcroft. "Hydrogen dominant metallic alloys: high temperature superconductors?". *Phys. Rev. Lett.* **2004**, *92*, 187002.

[13] M. I. Eremets, I. A. Trojan, S. A. Medvedev, J. S. Tse, Y. Yao. "Superconductivity in hydrogen dominant materials: Silane". *Science* **2008**, *319*, 1506.

[14] T. A. Strobel, M. Somayazulu, R. J. Hemley. "Novel pressure-induced interactions in silane-hydrogen". *Phys. Rev. Lett.* **2009**, *103*, 065701.

[15] S. Wang, H.-K. Mao, X.-J. Chen, W. Mao. "High pressure chemistry in the H_2-SiH_4 system". *Proc. Natl. Acad. Sci.* **2009**, *106*, 14763.

[16] E. Zurek, R. Hoffmann, N. W. Ashcroft, A. R. Oganov, A. O. Lyakhov. "A little bit of lithium does a lot for hydrogen". *Proc. Natl. Acad. Sci.* **2009**, *106*, 17640.

[17] Y. Yao, D. D. Klug. "Silane plus molecular hydrogen as a possible pathway to metallic hydrogen". *Proc. Natl. Acad. Sci.* **2010**, *107*, 20893.

[18] W.-L. Yim, J. S. Tse, T. Iitaka. "Pressure-induced intermolecular interactions in crystalline silane-hydrogen". *Phys. Rev. Lett.* **2010**, *105*, 215501.

[19] P. Baettig, E. Zurek. "Pressure-stabilized sodium polyhydrides: NaH_n ($n > 1$)". *Phys. Rev. Lett.* **2011**, *106*, 237002.

[20] A. Torabi, Y. Song, V. N. Staroverov. "Pressure-induced polymorphic transitions in crystalline diborane deduced by comparison of simulated and experimental vibrational spectra". *J. Phys. Chem. C* **2013**, *117*, 2210.

[21] C.-H. Hu, A. R. Oganov, Q. Zhu, G.-R. Qian, G. Frapper, A. O. Lyakhov, H.-Y. Zhou. "Pressure-induced stabilization and insulator-superconductor transition of BH". *Phys. Rev. Lett.* **2013**, *110*, 165504.

[22] D. S. Jones, W. N. Lipscomb. "X-ray evidence for bonding electrons in diborane". *J. Chem. Phys.* **1969**, *51*, 3133.

[23] A. R. Oganov, A. O. Lyakhov, M. Valle. "How evolutionary crystal structure prediction works-and why". *Acc. Chem. Res.* **2011**, *44*, 227.

[24] A. O. Lyakhov, A. R. Oganov, H. T. Stokes, Q. Zhu. "New developments in evolutionary structure prediction algorithm USPEX". *Comput. Phys. Commun.* **2013**, *184*, 1172.

[25] A. D. Becke, K. E. Edgecombe. "A simple measure of electron localization in atomic and molecular systems". *J. Chem. Phys.* **1990**, *92*, 5397.

[26] B. G. Pfrommer, M. Côté, S. G. Louie, M. L. Cohen. "Relaxation of crystals with the quasi-Newton method". *J. Comput. Phys.* **1997**, *131*, 233.

Chapter 4

Band gap reduction in ZnO and ZnS by creating layered ZnO/ZnS heterostructures

4.0 Introduction

The intense search for renewable and economically viable sources of energy has spurred much interest in semiconductor-based devices capable of converting solar energy into electricity. Zinc oxide (ZnO) and zinc sulfide (ZnS) are abundant, chemically stable, and nontoxic materials that are particularly appealing for building such devices. In one of their common forms, bulk ZnO and ZnS have wurtzite-type structures with tetrahedrally coordinated zinc atoms. The wide band gaps of wurtzite-type ZnO (3.4 eV) and ZnS (3.91 eV) [2] are well suited for absorption in the ultraviolet region of the electromagnetic spectrum [3, 4, 5], but are too large for harvesting visible light. Photocatalytic hydrogen production, for instance, is expected to be achievable for semiconductors with band gaps in the range 1.8–2.2 eV [6]. In photovoltaic devices, the maximum efficiency is reached for a band gap of 1.1 eV [7].

The fact that inexpensive semiconductors such as ZnS and ZnO have wide band gaps is unfortunate because ultraviolet light accounts for only a small fraction (∼5%) of the solar energy compared to visible light (∼45%) [8]. It would greatly facilitate photovoltaic device engineering if one could reduce the band gaps of either ZnO or ZnS.

Reprinted in part with permission from **A. Torabi** and V. N. Staroverov, "Band gap reduction in ZnO and ZnS by creating layered ZnO/ZnS heterostructures", *J. Phys. Chem. Lett.* **2015**, *6*, 2075. Copyright 2015, The American Chemical Society.

The conventional technique for modulating the band gap of a given semiconductor is by doping the crystal with other elements. However, the efficacy of this approach is limited by the maximum dopability of the material, which in the case of ZnO and ZnS is extremely low [9]. Another technique to reduce the band gap is to combine ZnO and ZnS into bulk or nanosized heterostructures, through a judicious control of atomic composition and structural configuration. As a matter of fact, multi-component materials involve intriguing morphological features which enable them to exhibit distinct properties from those observed in their bulk forms.

Numerous studies have shown that, despite the large lattice parameter mismatch between ZnS and ZnO (∼16%), one can successfully synthesize high-quality ZnO/ZnS heterostructures with a variety of morphologies, such as nanocables [10, 11], nanosaw [12], nanoring [13], nanobelt [14], nanoribbons [15, 16], nanotetrapod [17], nanoflower [18], nanowires [19, 20], core-shell nanotubes [21, 22], nanorod [23], and nanocone [24]. More recently and for the first time, nanoscaled spectroscopy across an interface between ZnS nanobelt/ZnO nanorod was studied in detail by Sham and coworkers [25].

The possibility of band gap engineering with ZnO and ZnS has so far been explored computationally for bulk ZnO/ZnS heterostructures [26], multilayered structures and solid solutions of ZnO or ZnS with group-13 phosphides and nitrides [27, 28], ZnO/ZnS core/shell nanowires [26, 29, 30] and heteronanotubes [31]. In particular, Schrier *et al.* [26] predicted a band gap of 2.31 eV for ZnO/ZnS bulk heterostructures consisting of zinc-blende ZnO and ZnS slabs in the (001) direction with seven monolayers per slab, and a band gap of 2.07 eV for ZnO/ZnS core/shell heterostructured nanowires. Hart *et al.* [27] showed that the band gap of ZnS can be reduced to about 2 eV by forming layered ZnS/GaP structures. Saha *et al.* [30] studied the electronic structure of ZnO/ZnS core/shell nanowires as a function of core radius and shell thickness and found that when the radius of the ZnO nanowire core is kept fixed, the band gap of the heterosystem decreases with increasing ZnS shell thickness.

4.1 Models

Motivated by the importance of the problem and the intriguing findings of Refs. [26, 27, 28, 29, 30, 31] we undertook a systematic investigation of layered wurtzite-type ZnO/ZnS bulk heterostructures in order to find out to what extent their band gap can be reduced through ZnO−ZnS layered alternation.

Unit cells of layered ZnO/ZnS bulk heterostructures were constructed as follows. We started with ten (0001)-monolayers of ZnS (*i.e.*, monolayers normal to the [0001] direction) and replaced them, one by one, with (0001)-monolayers of ZnO. Replacement of a single monolayer of ZnS with ZnO per every 10 monolayers of ZnS gives the 1:9 ZnO/ZnS structure shown in Figure 4.1.

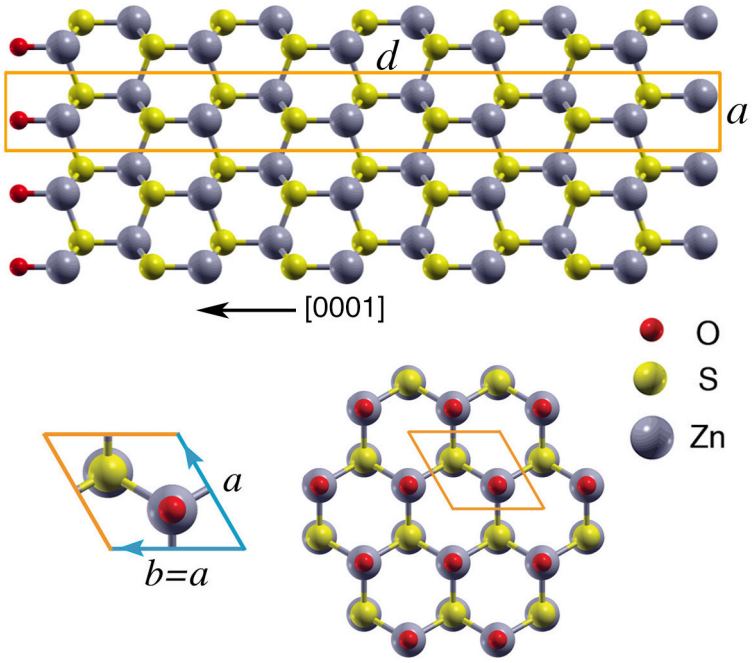

Figure 4.1: Side and top views of a supercell of the layered 1:9 ZnO/ZnS bulk heterostructure. The primitive unit cell is the highlighted parallelepiped. The angle between the a and b axes is $\gamma = 60$.

Replacement of two contiguous monolayers gives a 2:8 ZnO/ZnS heterostructure, and so forth until all 10 monolayers of ZnS are replaced by 10 monolayers of ZnO. Unit cells of the intermediate 5:5 ZnO/ZnS and 9:1 ZnO/ZnS heterostructures are shown in Figure 4.2. All the atoms in these heterostructures remain tetrahedrally coordinated.

Wurtzite-type structures of ZnO and ZnS are characterized by the following parameters: the lattice constants $a = b$ (translations normal to the [0001] direction), c (translation along the [0001] direction), and the internal parameter u related to the c/a ratio [32]. In the case of ZnO/ZnS heterostructures, the meaning of parameters a and b is preserved, but parameter c is replaced by parameter d representing the length of the primitive unit cell (Figure 4.1).

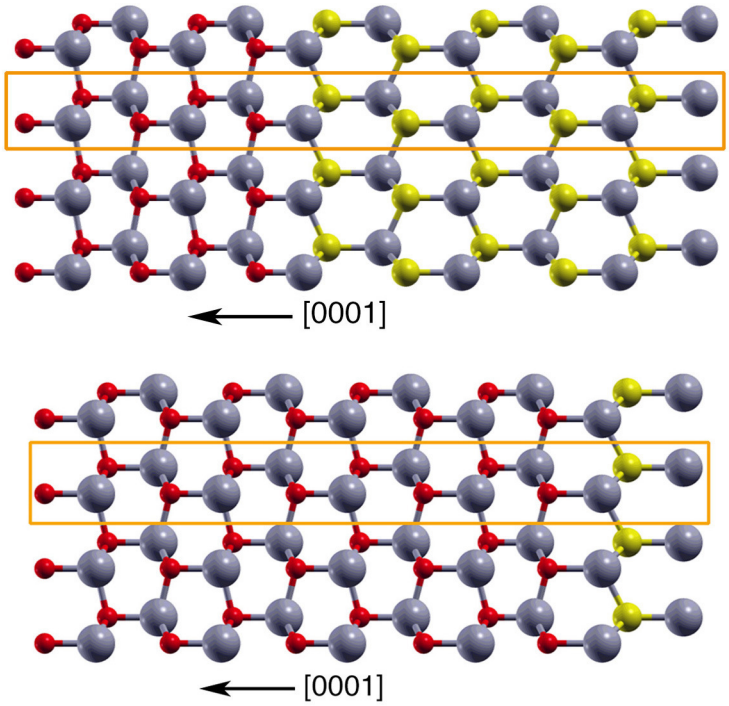

Figure 4.2: Side views of supercells of layered 5:5 ZnO/ZnS (top) and 9:1 ZnO/ZnS (bottom) bulk heterostructure. The conventions are the same as in Figure 4.1.

We note in passing that the ZnO/ZnS heterostructures constructed as above may also serve as models for various interfaces between ZnS nanobelt and ZnO nanorod structures studied by the Sham group [25]. Specifically, the 1:9 ZnO/ZnS heterostructure represents an early stage of the ZnO nanorod growth on a ZnS nanobelt, whereas the 5:5 ZnO/ZnS heterostructure mimics the interface between a ZnS nanobelt and a grown ZnO nanorod.

4.2 Results

The lattice parameters of ZnO, ZnS and ZnO/ZnS heterostructures were optimized using the Quantum Espresso program and the modification of the PBE generalized gradient approximation for solids known as PBEsol, which gives more realistic values of lattice parameters than the PBE functional. No change in the hexagonal pattern occurred during the supercells relaxation; the Zn, O, and S atoms of the heterostructures remained in the same fractional atomic positions (1/3, 1/3) and (2/3, 2/3) relative to the a and b axes as in bulk wurtzite. To compute the band gaps, we employed the Heyd–Scuseria–Ernzerhof screened Coulomb hybrid density functional [1, 33, 34]

in its 2006 parametrization [35] (HSE06) which is known to give superior band-gap predictions [36] compared to generalized gradient approximations such as PBE. The use of the HSE06 functional for band-gap calculations distinguishes this work from previous computational studies of ZnO, ZnS, [37, 38, 39, 40, 41] and ZnO/ZnS nanostructures [26, 29, 30, 31].

In order to demonstrate that the HSE06 functional is more suitable for our purposes than PBE and PBEsol, we first calculated the band gaps of pure bulk ZnO and ZnS using all three functionals at the respective optimized geometries (Table 4.1).

Table 4.1: Optimized structures and corresponding band gaps of wurtzite-type ZnO and ZnS in comparison with experiment.

ZnO					ZnS				
method	a	c	u	E_g(eV)	method	a	c	u	E_g(eV)
PBE	3.318	5.339	0.380	0.67	PBE	3.789	6.358	0.374	1.86
PBEsol	3.272	5.260	0.380	0.63	PBEsol	3.843	6.258	0.374	1.92
HSE06	3.252	5.245	0.382	2.58	HSE06	3.803	6.233	0.376	3.59
exp.	3.249	5.207	0.382	3.4	exp.	3.811	6.234	0.375	3.91

The results of these calculations (Table 4.1 and Figure 4.3) show that PBE as usual overestimates the lattice parameters relative to the experimental values and predicts band gaps that are much too low: 20% and 48% of the experimental values for ZnO and ZnS, respectively. The PBEsol functional gives significantly more accurate values of lattice parameters, but the band gaps are still too low: 19% and 49% of the experimental values for ZnO and ZnS, respectively. By contrast, the HSE06 functional predicts lattice constants that are similar to the PBEsol values but gives much more realistic band gaps: 76% and 92% of the experimental values for ZnO and ZnS, respectively. Because the PBEsol and HSE06 values of lattice parameters are close to each other, we will henceforth assume that it is a good approximation to use PBEsol-optimized lattice parameters of ZnO, ZnS, and ZnO/ZnS heterostructures as substitutes for the HSE06-optimized values.

We also confirm the recent observation [42] that one can obtain an essentially exact band gap of 3.4 eV for ZnO by increasing the value of the exact-exchange mixing parameter a_X in the HSE06 functional from 0.25 to 0.375. However, we decided against using this modification for calculations on ZnO/ZnS heterostructures because we found that for pure bulk ZnS the HSE06 functional with $a_X = 0.375$ produces a band gap that is far too large (4.3 eV).

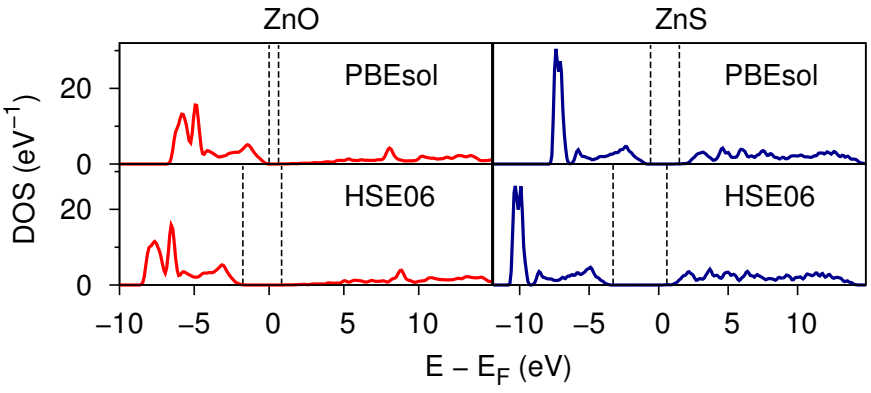

Figure 4.3: Density of states (DOS) calculated using PBEsol and HSE06 functionals for bulk ZnO and ZnS. The Fermi level is at 0 eV. Vertical dashed lines indicate positions of the highest occupied and lowest unoccupied states of each type.

The results of HSE06 band gaps calculations for the PBEsol-optimized geometries of ZnO, ZnS, and ZnO/ZnS heterostructures are summarized in Table 4.2.

Table 4.2: Calculated structural parameters, band gaps and total energies of layered $m : n$ ZnO/ZnS heterostructures. The structures were optimized using the PBEsol functional. The band gaps were computed using the HSE06 functional for the PBEsol geometries. The parameters a and d are defined in Figure 4.1. $\bar{r}$(ZnO) and $\bar{r}$(ZnS) are, respectively, the Zn–O and Zn–S bond lengths averaged over the chain of atoms inside the unit cell.

structure	structural parameters (Å)					
$m : n$	a	d	$\bar{r}$(ZnO)	$\bar{r}$(ZnS)	E_g(eV)	Total energy (eV)
			$m + n = 10$			
0:10	3.843	31.290		2.348	3.59	-1299.689019
1:9	3.832	31.013	2.120	2.359	2.23	-1308.246830
2:8	3.795	30.454	2.102	2.363	1.97	-1316.822891
3:7	3.750	29.795	2.092	2.355	1.58	-1325.405887
4:6	3.692	29.257	2.084	2.345	1.57	-1333.999945
5:5	3.631	28.790	2.074	2.336	1.50	-1342.609644
6:4	3.564	28.362	2.064	2.325	1.53	-1351.220893
7:3	3.496	28.024	2.054	2.314	1.54	-1359.851845
8:2	3.432	27.637	2.043	2.312	1.55	-1368.498064
9:1	3.371	27.231	2.033	2.324	1.55	-1377.165925
10:0	3.272	26.300	1.995		2.58	-1385.842070

The most striking conclusion emerging from these data is that the introduction of a single ZnO monolayer per every 10 monolayers of ZnS (1:9 ZnO/ZnS) decreases

the band gap by 38% from 3.59 eV to 2.23 eV. Similarly, substitution of every tenth monolayer in bulk ZnO with a single ZnS monolayer (9:1 ZnO/ZnS) decreases the band gap by 40% from 2.58 eV to 1.55 eV. Between 3:7 ZnO/ZnS and 9:1 ZnO/ZnS, the band gap does not vary much and stays in the range between 1.50–1.58 eV. The minimum of 1.50 eV is reached in 5:5 ZnO/ZnS. As can be inferred from the calculated total electronic energies (last column in Table 4.2), the 5:5 ZnO/ZnS heterostructure is thermodynamically metastable as it has a higher molar energy than bulk ZnO and ZnS separately:

$$-1342.609644 \text{ (5:5 ZnO/ZnS)} > -1342.765544 = -(\frac{1385.842070 + 1299.689019}{2}). \tag{4.56}$$

Since the lower band gap was found for a ZnO/ZnS heterostructure with equal mole fractions of ZnO and ZnS, it is natural to ask whether the $n:n$ heterostructure with $n = 5$ yields the lowest possible band gap. To answer this question, we optimized the geometries of $n:n$ ZnO/ZnS heterostructures for $n = 1$ to $n = 6$ and computed their band gaps using the same computational methodology as above. We found that the computed band gap as a function of n indeed reaches its minimum at $n = 5$ (Table 4.3).

Table 4.3: Calculated structural parameters and band gaps of layered $n:n$ ZnO/ZnS heterostructures. The conventions are the same as in Table 4.2.

structure	structural parameters (Å)				
$m:n$	a	d	$\bar{r}$(ZnO)	$\bar{r}$(ZnS)	E_g(eV)
		$m = n$			
1:1	3.600	5.872	2.077	2.327	2.31
2:2	3.615	11.645	2.074	2.334	1.97
3:3	3.624	17.367	2.074	2.335	1.77
4:4	3.627	23.066	2.073	2.336	1.66
5:5	3.631	28.790	2.074	2.336	1.50
6:6	3.626	34.152	2.069	2.327	1.65

It is interesting to note that the lattice parameter a for $n:n$ ZnO/ZnS heterostructures first increases with n and then decreases, with a maximum reached at $n = 5$. In the theoretical limit $n \to \infty$, the calculated parameter a for $n:n$ heterostructures should approach 3.558 Å, the average of the a values for bulk ZnO and ZnS.

4.3 Discussion

To understand the origin of band gap reduction in crystals with ZnO/ZnS layer alternation, we computed the band structure (Figure 4.4) and projected densities of states (PDOS) for bulk ZnO, ZnS, and selected ZnO/ZnS heterostructures (Figure 4.5).

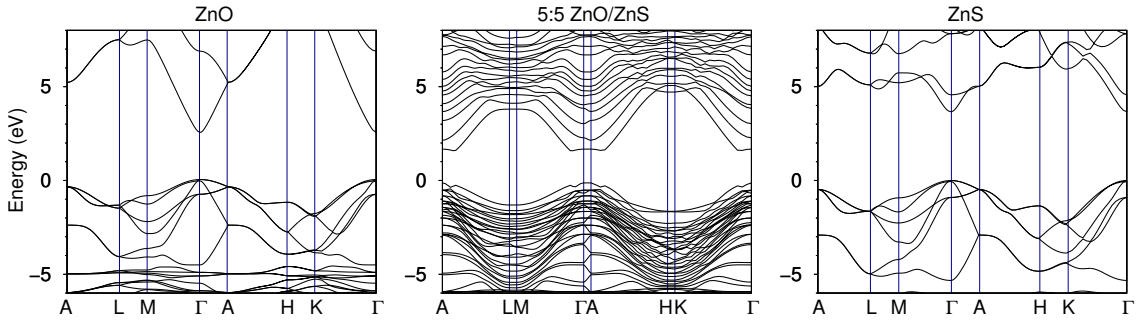

Figure 4.4: Electronic band structure of bulk ZnO, 5:5 ZnO/ZnS, and ZnS computed using the HSE06 functional at the respective PBEsol-optimized geometries. The **k**-path inside the Brillouin zone for a hexagonal reciprocal lattice is defined in Ref. [43]. The lowest band gaps in bulk ZnO and ZnS are direct and in 5:5 ZnO/ZnS is indirect.

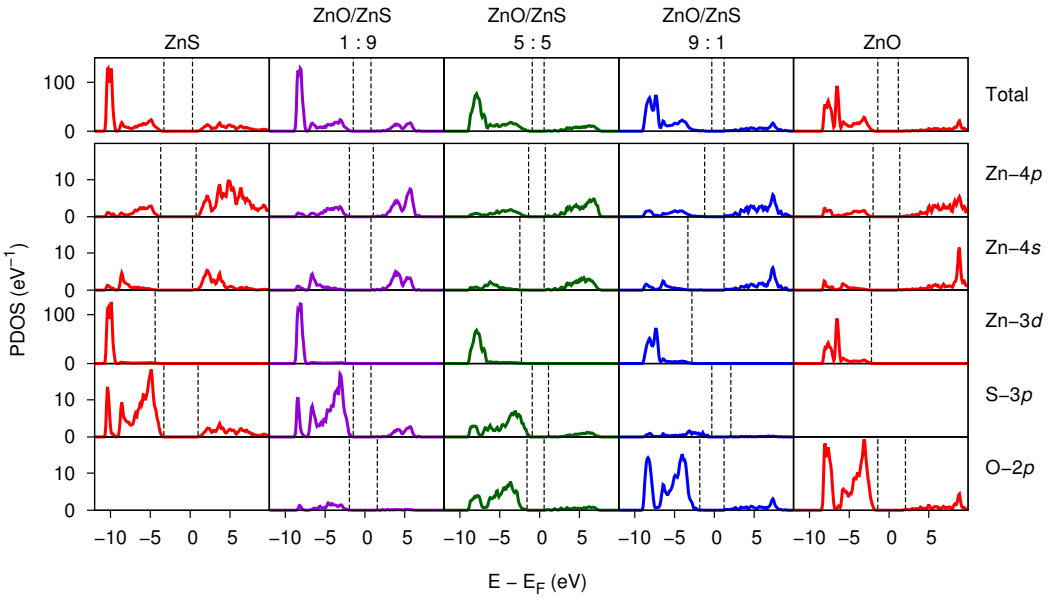

Figure 4.5: Total and projected densities of states calculated using the HSE06 functional at the PBEsol-optimized geometries of wurtzite-type bulk ZnS, wurtzite-type bulk ZnO, and selected ZnO/ZnS heterostructures. The Fermi level is always at 0 eV. Vertical dashed lines indicate positions of the highest occupied and lowest unoccupied states of each type. Note the different scales on the vertical axes for the total and Zn-3*d* densities of states.

These plots suggest the following mechanisms of band gap narrowing. In pure ZnS, the band gap is essentially the gap between the highest occupied (bonding) S-3p level and the lowest unoccupied (antibonding) Zn-4s level. In bulk ZnO, the band gap is the gap between the highest occupied O-2p level and the lowest unoccupied Zn-4s and Zn-4p levels. In the ZnO/ZnS heterostructures, the highest occupied S-3p level in the heterostructures is always higher in energy than the highest occupied O-2p level, and so their band gap is essentially determined by the gap between highest occupied S-3p level and the lowest unoccupied Zn-4s/4p levels. From Figure 4.5, we see that, as the fraction of ZnO in ZnO/ZnS heterostructures increases, the highest occupied S-3p level shifts to higher energies, whereas the lowest unoccupied Zn-4s and Zn-4p levels drift slightly toward lower energies. The net result of these opposite trends is a narrowing of the total band gap, with a minimum band gap value attained for the 5:5 ZnO/ZnS heterostructure.

The observed shifts in the S-3p and Zn-4s/4p levels can be explained in terms of contraction and expansion of the crystal lattice of the 5:5 ZnO/ZnS heterostructure relative to pure bulk ZnS and ZnO. The calculated lattice parameters a for the 5:5 ZnO/ZnS heterostructure and pure bulk ZnO and ZnS are, respectively, 3.631, 3.272, and 3.843 Å (Table 4.2). This means that, in the 5:5 ZnO/ZnS heterostructure, the S atoms are effectively in a contracted ZnS lattice, while the Zn atoms of the ZnO layers are in an expanded ZnO lattice. The contraction of the ZnS lattice causes the orbital energy levels of the S atoms to rise, while the expansion of the ZnO lattice lowers the orbital energy levels of the Zn atoms of the ZnO layers, as seen in Figure 4.5. To validate this explanation, we computed the PDOS for the normal and distorted ZnS and ZnO lattices. The calculations showed that when the ZnS lattice parameter a is decreased from 3.843 Å to 3.631 Å, the highest occupied S-3p level shifts up from -3.30 eV to -2.81 eV, and when the ZnO lattice parameter a is increased from 3.272 Å to 3.631 Å, the lowest unoccupied Zn-4s level shifts down from 1.11 eV to 0.89 eV, and the lowest unoccupied Zn-4p level from 1.06 eV to 0.91 eV.

To determine whether the observed band-gap reduction is also influenced by a possible transfer of charge between the atoms and/or interfaces, we calculated Bader atomic charges [49] on all atoms in the unit cell of the 5:5 ZnO/ZnS heterostructure and compared them to the corresponding atomic charges in pure bulk ZnO ($\pm 1.285e$) and ZnS ($\pm 0.911e$) (Figure 4.6). The individual charges on the Zn and S atoms of the ZnS layers were found to have changed very little relative to pure ZnS (by $0.012e$ on average and $0.031e$ at most), whereas the charges on the Zn and O atoms of the ZnO layers

all decreased in magnitude relative to pure ZnO (by 0.065e on average and 0.101e at most). The net charge of the 5 ZnO contiguous monolayers in the heterostructure is $-0.050e$ per unit cell, whereas the net charge of the 5 contiguous ZnS monolayers is $+0.050e$ per unit cell, indicating that the overall charge transfer between the ZnO and ZnS interfaces is negligible.

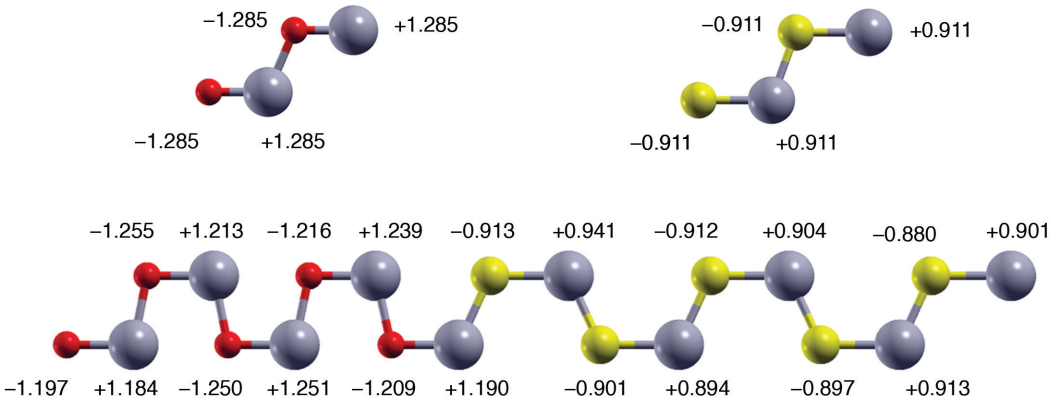

Figure 4.6: Bader atomic charges of pure bulk ZnO (top left), pure bulk ZnS (top right) and 5:5 ZnO/ZnS heterostructure (bottom). The numbers are in units of e.

Therefore, the redistribution of charge occurs mainly between the Zn and O atoms of the heterostructure and enhances the observed band-gap reduction by slightly lowering the Zn–O bond polarity, but this effect is less significant than the lattice distortion.

We have also calculated the valence band maximum (VBM) and conduction band minimum (CBM) orbitals for the 5:5 ZnO/ZnS heterostructure, and found that they are localized in different regions: the VBM on the ZnS layers, the CBM on the ZnO layers, with both VBM and CBM densities increasing toward the ZnO/ZnS interface boundary. This spatial separation of the VBM and CBM orbitals facilitates charge carrier control and therefore is beneficial for photovoltaic applications.

4.4 Conclusion

In conclusion, we have found computationally that one can reduce the relatively large band gap of semiconductors ZnO and ZnS by up to 42% and 58%, respectively, by creating bulk heterostructures in which nanolayers of ZnO alternate nanolayers of ZnS. Band gaps as low as 1.5–1.6 eV are achieved when $m = 3$ to $m = 9$ contiguous monolayers of ZnO alternative with $n = 10 - m$ contiguous monolayers of ZnS (Figure 4.7).

Because the HSE06 functional underestimates band gaps of pure bulk ZnO and ZnS by 24% and 8%, respectively, the calculated minimum band gap of 1.5 eV is likely underestimated as well. Assuming conservatively that the HSE06 functional underestimates band gaps of ZnO/ZnS heterostructures by 20% relative to experiment, we expect the unknown experimental band gap of the 5:5 ZnO/ZnS heterostructure to be no higher than 1.9 eV. Our findings indicate that integration of ZnO and ZnS semiconductors into layered heterostructures is an effective strategy for band-gap engineering and the development of photovoltaic devices that can harness, store and utilize the solar energy.

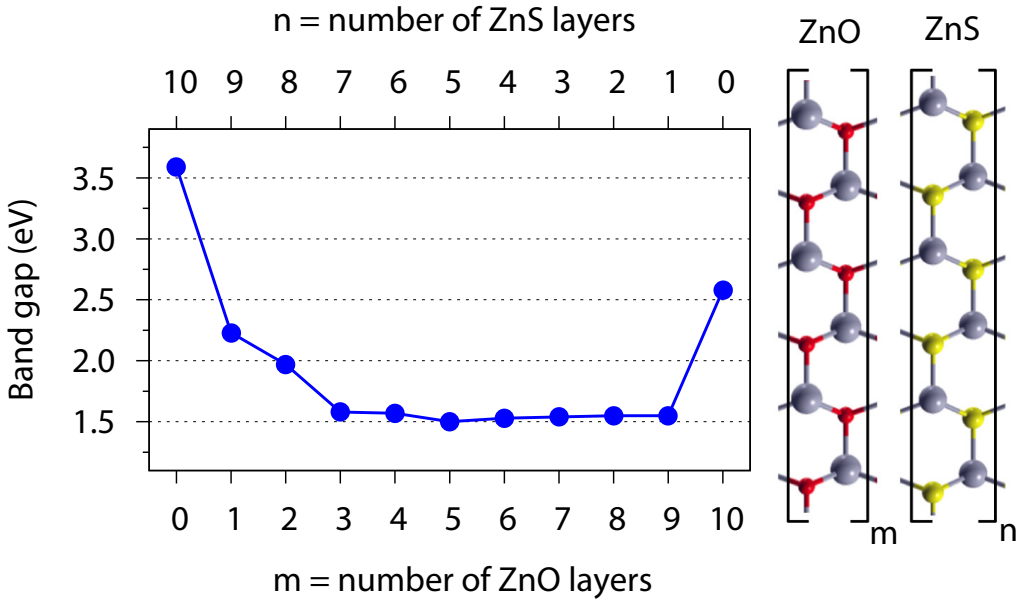

Figure 4.7: Band gap energy of $m : n$ ZnO/ZnS heterostructures.

4.5 Computational methodology

All electronic structure calculations reported in this work were performed with the Quantum Espresso program (version 5.0.1) at $T = 0$ K using plane-wave basis sets with a cutoff energy of 120 Ry and the Troullier–Martins norm-conserving pseudopotentials. PBE and PBEsol calculations were carried using PBE and PBEsol pseudopotentials, respectively, but the HSE06 calculations used PBEsol pseudopotentials. The pseudopotentials were taken from the PSLibrary (version 1.0.0). The $3d$ electrons of Zn atoms were treated as valence electrons. A 8×8×6 Monkhorst–Pack **k**-point grid was adopted for calculations on bulk ZnO and ZnS; a $8 \times 8 \times 1$ grid was used for the

$m + n = 10$ heterostructures. For the $n : n$ heterostructures, we used a $8 \times 8 \times K_z$ grid with $K_z = 6, 3, 2, 2, 1$ for $n = 1, 2, 3, 4, 6$, respectively. With these settings, the total energy was converged to within 1 mRy with respect to the **k**-point grid. The convergence criterion for Kohn–Sham self-consistency cycles was set to 10^{-8} Ry. All atomic coordinates and lattice parameters were optimized without any constraints by employing the Broyden–Fletcher–Goldfarb–Shanno quasi-Newton algorithm. The structures were considered optimized when the components of all Hellmann–Feynman forces dropped below 10^{-4} Ry/Å. Because structure optimization at the HSE06 level is not implemented in the version of QUANTUM ESPRESSO which we used, we found the optimal HSE06 lattice parameters of ZnO and ZnS reported in Table 4.1 by a two-dimensional search on the potential energy surface using a discrete step size of 0.001 Å. The results of our calibration calculations on bulk ZnO and ZnS are in good agreement with previous investigations [44, 45, 46, 47, 48], small discrepancies being due to differences in pseudopotentials, plane wave cutoffs, and other details of the calculations. The XCrySDen package was employed for visualizing the results.

Bibliography

[1] J. Heyd, G. E. Scuseria, M. Ernzerhof. "Hybrid functionals based on a screened Coulomb potential". *J. Chem. Phys.* **2003**, *118*, 8207.

[2] S. Kasap, P. Capper, *"Springer Handbook of Electronic and Photonic Materials"*, Springer, **2006**.

[3] Ü. Özgür, Y. I. Alivov, C. Liu, A. Teke, M. A. Reshchikov, S. Dogan, V. Avrutin, S.-J. Cho, H. Morkoç. "A comprehensive review of ZnO materials and devices". *J. Appl. Phys.* **2005**, *98*, 041301.

[4] X. Fang, Y. Bando, U. K. Gautam, T. Zhai, H. Zeng, X. Xu, M. Liao, D. Golberg. "ZnO and ZnS nanostructures: ultraviolet-light emitters, lasers, and sensors". *Crit. Rev. Sol. State Mater. Sci.* **2009**, *34*, 190.

[5] X. Fang, T. Zhai, U. K. Gautam, L. Li, L. Wu, Y. Bando, D. Golberg. "ZnS nanostructures: from synthesis to applications". *Progr. Mater. Sci.* **2011**, *56*, 175.

[6] J. Nowotny, C. C. Sorrell, L. R. Sheppard, T. Bak. "Solar-hydrogen: environmentally safe fuel for the future". *Int. J. Hydrogen Energy* **2005**, *30*, 521.

[7] W. Shockley, H. J. Queisser. "Detailed balance limit of efficiency of p-n junction solar cells". *J. Appl. Phys.* **1961**, *32*, 510.

[8] M. Romero, J. Blanco, B. Sanchez, A. Vidal, S. Malato, A. I. Cardona, E. Garcia. "Solar photocatalytic degradation of water and air pollutants: challenges and perspectives". *Sol. Energy* **1999**, *66*, 169.

[9] S. B. Zhang, S.-H. Wei, A. Zunger. "Microscopic origin of the phenomenological equilibrium "doping limit rule" in n-type III-V semiconductors". *Phys. Rev. Lett.* **2000**, *84*, 1232.

[10] X. Wang, P. Gao, J. Li, C. J. Summers, Z. L. Wang. "Rectangular Porous ZnO–ZnS Nanocables and ZnS Nanotubes". *Adv. Mater.* **2002**, *14*, 1732.

[11] C. Yan, D. Xue. "Conversion of ZnO nanorod arrays into ZnO/ZnS nanocable and ZnS nanotube arrays via an *in situ* chemistry strategy". *J. Phys. Chem. B* **2006**, *110*, 25850.

[12] G. Shen, D. Chen, C. J. Lee. "Hierarchical saw-like ZnO nanobelt/ZnS nanowire heterostructures induced by polar surfaces". *J. Phys. Chem. B* **2006**, *110*, 15689.

[13] X. Wu, P. Jiang, Y. Ding, W. Cai, S.-S. Xie, Z. L. Wang. "Mismatch strain induced formation of ZnO/ZnS heterostructured rings". *Adv. Mater.* **2007**, *19*, 2319.

[14] J. Yan, X. Fang, L. Zhang, Y. Bando, U. K. Gautam, B. Dierre, T. Sekiguchi, D. Golberg. "Structure and cathodoluminescence of individual ZnS/ZnO biaxial nanobelt heterostructures". *Nano Lett.* **2008**, *8*, 2794.

[15] X. Fan, M.-L. Zhang, I. Shafiq, W.-J. Zhang, C.-S. Lee, S.-T. Lee. "ZnS/ZnO heterojunction nanoribbons". *Adv. Mater.* **2009**, *21*, 2393.

[16] M. W. Murphy, X. T. Zhou, J. Y. P. Ko, J. G. Zhou, F. Heigl, T. K. Sham. "Optical emission of biaxial ZnO–ZnS nanoribbon heterostructures". *J. Chem. Phys.* **2009**, *130*, 084707.

[17] L. Yu, X.-F. Yu, Y. Qiu, Y. Chen, S. Yang. "Nonlinear photoluminescence of ZnO/ZnS nanotetrapods". *Chem. Phys. Lett.* **2008**, *465*, 272.

[18] Y. Ni, S. Yang, J. Hong, L. Zhang, W. Wu, Z. Yang. "Fabrication, characterization and properties of flowerlike ZnS- ZnO heterogeneous microstructures built up by ZnS-particle-strewn ZnO microrods". *J. Phys. Chem. C* **2008**, *112*, 8200.

[19] J. Li, D. Zhao, X. Meng, Z. Zhang, J. Zhang, D. Shen, Y. Lu, X. Fan. "Enhanced ultraviolet emission from ZnS-coated ZnO nanowires fabricated by self-assembling method". *J. Phys. Chem. B* **2006**, *110*, 14685.

[20] K. Wang, J. J. Chen, Z. M. Zeng, J. Tarr, W. L. Zhou, Y. Zhang, Y. F. Yan, C. S. Jiang, J. Pern, A. Mascarenhas. "Synthesis and photovoltaic effect of vertically aligned ZnO/ZnS core/shell nanowire arrays". *Appl. Phys. Lett.* **2010**, *96*, 123105.

[21] S. K. Panda, A. Dev, S. Chaudhuri. "Fabrication and luminescent properties of c-axis oriented ZnO-ZnS core-shell and ZnS nanorod arrays by sulfidation of aligned ZnO nanorod arrays". *J. Phys. Chem. C* **2007**, *111*, 5039.

[22] H. Zhang, D. Yang, X. Ma, D. Que. "A versatile solution route for oxide/sulfide core–shell nanostructures and nonlayered sulfide nanotubes". *Nanotechnology* **2005**, *16*, 2721.

[23] M.-Y. Lu, J. Song, M.-P. Lu, C.-Y. Lee, L.-J. Chen, Z. L. Wang. "ZnO-ZnS heterojunction and ZnS nanowire arrays for electricity generation". *ACS Nano* **2009**, *3*, 357.

[24] X. Zhang, M. Chen, J. Wen, L. Wu, H. Gao, D. Zhang. "Side by side ZnO/ZnS hetero-junction nanocrystal arrays with superior field emission property". *CrystEngComm* **2013**, *15*, 1908.

[25] Z. Wang, J. Wang, T. K. Sham, S. Yang. "Tracking the interface of an individual ZnS/ZnO nano-heterostructure". *J. Phys. Chem. C* **2012**, *116*, 10375.

[26] J. Schrier, D. O. Demchenko, L. Wang, A. P. Alivisatos. "Optical properties of ZnO/ZnS and ZnO/ZnTe heterostructures for photovoltaic applications". *Nano Lett.* **2007**, *7*, 2377.

[27] J. N. Hart, N. L. Allan. "GaP-ZnS solid solutions: semiconductors for efficient visible light absorption and emission". *Adv. Mater.* **2013**, *25*, 2989.

[28] J. N. Hart, M. Cutini, N. L. Allan. "Band gap modification of ZnO and ZnS through solid solution formation for applications in photocatalysis". *Energy Procedia* **2014**, *60*, 32.

[29] S. Saha, P. Sarkar. "Electronic structure of ZnO/ZnS core/shell quantum dots". *Chem. Phys. Lett.* **2013**, *555*, 191.

[30] S. Saha, S. Sarkar, S. Pal, P. Sarkar. "Tuning the energy levels of ZnO/ZnS core/shell nanowires to design an efficient nanowire-based dye-sensitized solar cell". *J. Phys. Chem. C* **2013**, *117*, 15890.

[31] X. Zhang, S. Xie, Y. Fan, Z. Wang, H. Zhang, M. Zhao. "Structural and electronic properties of ZnS/ZnO heteronanotubes". *Physica E* **2011**, *43*, 1522.

[32] H. Morkoç, Ü. Özgür, *"Zinc Oxide: Fundamentals, Materials and Device Technology"*, Wiley- VCH: Weinheim, **2009**.

[33] J. Heyd, G. E. Scuseria. "Efficient hybrid density functional calculations in solids: assessment of the Heyd–Scuseria–Ernzerhof screened Coulomb hybrid functional". *J. Chem. Phys.* **2004**, *121*, 1187.

[34] J. Heyd, J. E. Peralta, G. E. Scuseria, R. L. Martin. "Energy band gaps and lattice parameters evaluated with the Heyd-Scuseria-Ernzerhof screened hybrid functional". *J. Chem. Phys.* **2005**, *123*, 174101.

[35] A. V. Krukau, O. Vydrov, A. F. Izmaylov, G. F. Scuseria. "Influence of the exchange screening parameter on the performance of screened hybrid functionals". *J. Chem. Phys.* **2006**, *125*, 224106.

[36] T. M. Henderson, J. Paier, G. E. Scuseria. "Accurate treatment of solids with the HSE screened hybrid". *Phys. Status Solidi B* **2011**, *248*, 767.

[37] H. Xu, Y. Li, A. L. Rosa, T. Frauenheim, R. Q. Zhang. "First-principles study of the structural stability and electronic properties of ZnS nanowires". *J. Phys. Chem. C* **2008**, *112*, 20291.

[38] F. De Angelis, L. Armelao. "Optical properties of ZnO nanostructures: a hybrid DFT/TDDFT investigation". *Phys. Chem. Chem. Phys.* **2011**, *13*, 467.

[39] J. M. Azpiroz, E. Mosconi, F. D. Angelis. "Modeling ZnS and ZnO nanostructures: structural, electronic, and optical properties". *J Phys. Chem. C* **2011**, *115*, 25219.

[40] J. M. Azpiroz, I. Infante, X. Lopez, J. M. Ugalde, F. D. Angelis. "A first-principles study of II–VI (II= Zn; VI= O, S, Se, Te) semiconductor nanostructures". *J. Mater. Chem.* **2012**, *22*, 21453.

[41] G. Malloci, L. Chiodo, A. Rubio, A. Mattoni. "Structural and optoelectronic properties of unsaturated ZnO and ZnS nanoclusters". *J. Phys. Chem. C* **2012**, *116*, 8741.

[42] Z. Wang, M. Zhao, X. Wang, X. Yan, X. He, X. Liu, S. Yan. "Hybrid density functional study of band alignment in ZnO–GaN and ZnO–(Ga1- xZnx)(N1- xOx)–GaN heterostructures". *Phys. Chem. Chem. Phys.* **2012**, *14*, 15693.

[43] W. Setyawan, S. Curtarolo. "High-throughput electronic band structure calculations: challenges and tools". *Comput. Mater. Sci.* **2010**, *49*, 299.

[44] P. Schröer, P. Krüger, J. Pollmann. "First-principles calculation of the electronic structure of the wurtzite semiconductors ZnO and ZnS". *Phys. Rev. B* **1993**, *47*, 6971.

[45] B. Meyer, D. Marx. "Density-functional study of the structure and stability of ZnO surfaces". *Phys. Rev. B* **2003**, *67*, 035403.

[46] J. Uddin, G. E. Scuseria. "Theoretical study of ZnO phases using a screened hybrid density functional". *Phys. Rev. B* **2006**, *74*, 245115.

[47] J. Wróbel, K. J. Kurzydłowski, K. Hummer, G. Kresse, J. Piechota. "Calculations of ZnO properties using the Heyd-Scuseria-Ernzerhof screened hybrid density functional". *Phys. Rev. B* **2009**, *80*, 155124.

[48] S. Saha, S. Pal, P. Sarkar, A. L. Rosa, T. Frauenheim. "A complete set of self-consistent charge density-functional tight-binding parametrization of zinc chalcogenides (ZnX; X= O, S, Se, and Te)". *J. Comput. Chem.* **2012**, *33*, 1165.

[49] W. Tang, E. Sanville, G. Henkelman. "A grid-based Bader analysis algorithm without lattice bias". *J Phys.: Condens. Matter* **2009**, *21*, 084204.

Chapter 5

Summary and future directions

Extreme packing of atoms under compression can have a profound effect on the physical and chemical properties of materials. For instance, insulators can become metallic under pressure [3, 2, 4], whereas metals can become wide-gap insulators [1]. These observations represent pressure as an intriguing tool for tuning the properties of materials. The interest in high-pressure conditions is also driven by the possibility of discovering novel industrial materials with exceptional properties that are unprecedented at ambient conditions.

While experimental challenges may limit one's ability to investigate the properties of materials at extreme conditions, there will be no practical limit for computationally simulating high pressure. Employing electronic structure simulations, this thesis examined the pressure-induced polymorphic transformations in solid diborane up to an unprecedented pressure for this class of materials. In particular, our findings suggest that B_2H_6 molecules in solid diborane remain chemically stable up to near-megabar pressures, and the geometry of the BHBH ring is not significantly altered by compression. We further predict that at pressures above 110 GPa, diborane will form new molecular structures consisting of one-dimensional $(BH_3)_n$ chains, and will become metallic near 138 GPa. While such pressures have not yet been reached experimentally, they are feasible, meaning that the first reports of pressure-induced polymerization and metallization of diborane are a matter of time. This will provide a practical pathway to one of the long-standing challenges of high-pressure materials science: achieving pressure-induced hydrogen metallization.

Escalating concerns for environmental pollution and energy shortage have also created a pressing demand for the development of semiconductor-based heterogeneous materials. New physical and chemical behaviors emerge when dissimilar semiconductors are

merged into a multi-component heterostructure. Properties also get affected as the geometry and morphology of the shrinking structures vary; and these have the potential to meet the ever-increasing demand for novel materials with improved functionalities. Employing electronic structure simulations, this thesis examined how the band gaps of ZnO and ZnS can be dramatically reduced by creating layered ZnO/ZnS bulk heterostructures in which m contiguous monolayers of ZnO alternate with n contiguous monolayers of ZnS. The predicted band gaps of layered ZnO/ZnS heterostructures span much of the visible spectrum, which makes these materials suitable for photovoltaic device engineering. The models proposed and studied in this work are helpful as they allow understanding of experimental observations on band gap modulations in various heterostructures.

Bibliography

[1] Y. Ma, M. Eremets, A. R. Oganov, Y. Xie, I. Trojan, S. Medvedev, A. O. Lyakhov, M. Valle, V. Prakapenka. "Transparent dense sodium". *Nature* **2009**, *458*, 182.

[2] P. M. Celliers, P. Loubeyre, J. H. Eggert, S. Brygoo, R. S. McWilliams, D. G. Hicks, T. R. Boehly, R. Jeanloz, G. W. Collins. "Insulator-to-conducting transition in dense fluid helium". *Phys. Rev. Lett.* **2010**, *104*, 184503.

[3] C.-Y. Liu, A. J. Bard. "Pressure-induced insulator–conductor transition in a photoconducting organic liquid-crystal film". *Nature* **2002**, *418*, 162.

[4] R. S. McWilliams, D. K. Spaulding, J. H. Eggert, P. M. Celliers, D. G. Hicks, R. F. Smith, G. W. Collins, R. Jeanloz. "Phase transformations and metallization of magnesium oxide at high pressure and temperature". *Science* **2012**, *338*, 1330.

A Copyright permissions

A.1 American Chemical Society permission

Journal of Physical Chemistry C
Journal of Physical Chemistry Letters
Permission type: Republish or display content
Type of use: Reuse in a Thesis/Dissertation

American Chemical Society's Policy on Theses and Dissertations

If your university requires you to obtain permission, you must use the RightsLink permission system. See RightsLink instructions at `http://pubs.acs.org/page/copyright/permissions.html`.

This is regarding request for permission to include your paper(s) or portions of text from your paper(s) in your thesis. Permission is now automatically granted; please pay special attention to the implications paragraph below. The Copyright Subcommittee of the Joint Board/Council Committees on Publications approved the following:

> Copyright permission for published and submitted material from theses and dissertations: ACS extends blanket permission to students to include in their theses and dissertations their own articles, or portions thereof, that have been published in ACS journals or submitted to ACS journals for publication, provided that the ACS copyright credit line is noted on the appropriate page(s).
>
> Publishing implications of electronic publication of theses and dissertation material: Students and their mentors should be aware that posting of theses and dissertation material on the Web prior to submission of material from that thesis or dissertation to an ACS journal may affect publication in that journal. Whether Web posting is considered prior publication may be evaluated on a case-by-case basis by the journal's editor. If an ACS

> journal editor considers Web posting to be "prior publication", the paper will not be accepted for publication in that journal. If you intend to submit your unpublished paper to ACS for publication, check with the appropriate editor prior to posting your manuscript electronically.

Reuse/Republication of the Entire Work in Theses or Collections: Authors may reuse all or part of the Submitted, Accepted or Published Work in a thesis or dissertation that the author writes and is required to submit to satisfy the criteria of degree-granting institutions. Such reuse is permitted subject to the ACS' "Ethical Guidelines to Publication of Chemical Research" (`http://pubs.acs.org/page/policy/ethics/index.html`); the author should secure written confirmation (via letter or email) from the respective ACS journal editor(s) to avoid potential conflicts with journal prior publication[4]/embargo policies. Appropriate citation of the Published Work must be made. If the thesis or dissertation to be published is in electronic format, a direct link to the Published Work must also be included using the ACS Articles on Request author-directed link−see `http://pubs.acs.org/page/policy/articlesonrequest/index.html`.

If your paper has not yet been published by ACS, please print the following credit line on the first page of your article: "Reproduced (or 'Reproduced in part') with permission from [JOURNAL NAME], in press (or 'submitted for publication'). Unpublished work copyright [CURRENT YEAR] American Chemical Society." Include appropriate information.

If your paper has already been published by ACS and you want to include the text or portions of the text in your thesis/dissertation, please print the ACS copyright credit line on the first page of your article: "Reproduced (or 'Reproduced in part') with permission from [FULL REFERENCE CITATION.] Copyright [YEAR] American Chemical Society." Include appropriate information.

Submission to a Dissertation Distributor: If you plan to submit your thesis to UMI or to another dissertation distributor, you should not include the unpublished ACS paper in your thesis if the thesis will be disseminated electronically, until ACS has published your paper. After publication of the paper by ACS, you may release the entire thesis (not the individual ACS article by itself) for electronic dissemination through the distributor; ACS's copyright credit line should be printed on the first page of the ACS paper.

[4]Prior publication policies of ACS journals are posted on the ACS website at `http://pubs.acs.org/page/policy/prior/index.html`.

A.2 Nature Publishing Group permission

Scientific Reports
Permission type: Republish or display content
Type of use: Reuse in a Thesis/Dissertation

Permission requests from authors

The authors of articles published by Nature Publishing Group, or the authors' designated agents, do not usually need to seek permission for re-use of their material as long as the journal is credited with initial publication. For further information about the terms of re-use for authors please see below.

If you are the author of this content (or his/her designated agent) please read the following. Since 2003, ownership of copyright in original research articles remains with the Authors[5], and provided that, when reproducing the Contribution or extracts from it, the Authors acknowledge first and reference publication in the Journal, the Authors retain the following non-exclusive rights:

1. To reproduce the Contribution in whole or in part in any printed volume (book or thesis) of which they are the author(s).

2. They and any academic institution where they work at the time may reproduce the Contribution for the purpose of course teaching.

3. To reuse figures or tables created by them and contained in the Contribution in other works created by them.

4. To post a copy of the Contribution as accepted for publication after peer review (in Word or Tex format) on the Author's own web site, or the Author's institutional repository, or the Author's funding body's archive, six months after publication of the printed or online edition of the Journal, provided that they also link to the Journal article on NPG's web site (e.g. through the DOI).

NPG encourages the self-archiving of the accepted version of your manuscript in your funding agency's or institution's repository, six months after publication. This policy complements the recently announced policies of the US National Institutes of Health, Wellcome Trust and other research funding bodies around the world. NPG recognizes

[5]Commissioned material is still subject to copyright transfer conditions

the efforts of funding bodies to increase access to the research they fund, and we strongly encourage authors to participate in such efforts.

Authors wishing to use the published version of their article for promotional use or on a web site must request in the normal way.

If you require further assistance please read NPG's online author reuse guidelines.

Note: *British Journal of Cancer* maintains copyright polices of its own that are different from the general NPG policies. Please consult this journal to learn more.

Curriculum Vitæ

Amin Torabi

Education:

- **Ph.D.** in Chemistry, University of Western Ontario, Canada (2011−2015)
  - Advisor: Prof. Viktor N. Staroverov
- **M.Sc.** in Physics, University of Windsor, Canada (2009−2010)
  - Advisor: Prof. Ricardo Aroca
- **B.Sc.** in Physics, Sharif University of Technology, Iran (2002−2006)
  - Advisor: Prof. Mohammadreza Hedayati

Work Experience:

- Teacher & Research Assistant, University of Western Ontario (2011−2015)
- Teacher & Research Assistant, University of Windsor (2009−2010)
- Electro-optics Lab Assistant, Hayyan Ltd., Iran (2007−2008)
- English Translator, Proofreader & Editor, HPAN LLC, Iran (2006−2007)

Publications:

3. **A. Torabi**, C. Murli, Y. Song, V. N. Staroverov, "Polymorphic transitions of diborane at sub- and near-megabar pressures", *Sci. Rep.* **2015**, *5*, 13929.

2. **A. Torabi**, V. N. Staroverov, "Band gap reduction in ZnO and ZnS by creating layered ZnO/ZnS heterostructures", *J. Phys. Chem. Lett.* **2015**, *6*, 2075.

1. **A. Torabi**, Y. Song and V. N. Staroverov, "Pressure-induced polymorphic transitions in crystalline diborane deduced by comparison of simulated and experimental vibrational spectra", *J. Phys. Chem. C* **2013**, *117*, 2210.

Presentations:

5. **A. Torabi**, C. Murli, Y. Song, V. N. Staroverov, "New structures and potential metallization of diborane at near-megabar pressure" 98$^{\text{th}}$ Canadian Chemistry Conference, Ottawa. (2015)

4. **A. Torabi**, V. N. Staroverov, "Computational design of narrow-gap ZnO/ZnS layered heterostructures" 26$^{\text{th}}$ Canadian Symposium on Theoretical and Computational Chemistry, Montréal. (2014)

3. **A. Torabi**, Y. Song, V. N. Staroverov, "Persistence of molecular diborane at elevated pressures, evidence from experimental and simulated vibrational spectra" 96$^{\text{th}}$ Canadian Chemistry Conference, Québec City. (2013)

2. **A. Torabi**, Y. Song, V. N. Staroverov, "Pressure-induced phase transitions in crystalline diborane deduced by comparison of simulated and experimental infrared and Raman spectra" 25$^{\text{th}}$ Canadian Symposium on Theoretical and Computational Chemistry, Guelph. (2012)

1. **A. Torabi**, C. Rangan, R. Aroca, "Resonance Raman calculations of organic semiconductors", 4$^{\text{th}}$ NSERC Strategic Network for Bioplasmonic Systems", Toronto. (2010)

Honors and Awards:

- CSC Travel Award, Western University (2015)
- Best Oral Presentation Award in the Theoretical & Computational Division, 98th Canadian Chemistry Conference, Ottawa (2015)
- Finalist in the Three-Minute Thesis competition, Western University (2014)
- First Award in Data Analytics, 2nd Industry Problem Solving Week, Western University (2014)
- Third-place Poster Award in the High Pressure Division, 96th Canadian Chemistry Conference, Montréal (2013)